A DSP-Enhanced AC Susceptometer for Characterisation of High Temperature Superconductors

Sergio Stephane Babet

Submitted in fulfillment of the Master of Science in Engineering

to the Faculty of Engineering, University of KwaZulu-Natal

September 2014

Supervisor: Dr. A.L.L Jarvis

Declarations

As the candidate's Supervisor I agree/do not agree to the submission of this thesis.

Signed: _____ Name: _____ Date: _____

DECLARATION

I, Sergio Stephane Babet declare that

(i) The research reported in this dissertation, except where otherwise indicated, is my original work.

(ii) This dissertation has not been submitted for any degree or examination at any other university.

(iii) This dissertation does not contain other persons' data, pictures, graphs or other information, unless specifically acknowledged as being sourced from other persons.

(iv) This dissertation does not contain other persons' writing, unless specifically acknowledged as being sourced from other researchers. Where other written sources have been quoted, then:
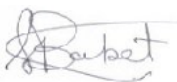
a) their words have been re-written but the general information attributed to them has been referenced;

b) where their exact words have been used, their writing has been placed inside quotation marks, and referenced.

(v) Where I have reproduced a publication of which I am an author, co-author or editor, I have indicated in detail which part of the publication was actually written by myself alone and have fully referenced such publications.

(vi) This dissertation does not contain text, graphics or tables copied and pasted from the Internet, unless specifically acknowledged, and the source being detailed in the dissertation and in the References sections.

Signed:

Acknowledgements

Abstract

DSP-based susceptometer was designed and implemented to study granular HTS $Y_1Ba_2Cu_3O_{7-x}$ (YBCO) superconducting specimens. The AC susceptometer is made up of a primary coil driven by an AC signal and two sensing coils: a balancing coil and a pickup coil which senses the magnetic response of a superconducting specimen. A particular feature of the AC susceptometer was a digital lock-in amplifier which was designed and implemented in DASYLab instead of using a conventional lock-in amplifier. The lock-in amplifier was necessary to separate the real and imaginary parts of AC susceptibility response of the superconducting sample placed into one of the sensing coils. Granular YBCO material is known for having a low critical current density, J_c, due to a weak link effect. Grain boundaries, which are responsible for the weak link effect, comprise of regions of high stress fields. In one experiment to test the apparatus, YBCO specimens were doped with hydrogen with the aim of relieving stresses to improve the intergranular critical current. The AC susceptometer was successfully used to characterise the intergranular critical current of YBCO samples. The relative intergranular critical current was successfully estimated using a critical state model, based on Bean model. The migration of H_2 molecules into the YBCO's lattice was not successful in relieving the stresses at the grain boundaries, and resulted in the deterioration of intergranular critical current.

List of Symbols and their Units

Roman Letters

A

a Crystal lattice parameter (Å)

A Area of cross section (m^2)

A' Area of cross section of wire (m^2)

B

b Crystal lattice parameter (Å)

b_o Burger vector

B Magnetic flux density (T)

B_a Applied magnetic flux density (T)

B_{in} Magnetic flux density inside a material (T)

B_{out} Magnetic flux density outside a material (T)

B_{net} Net magnetic flux density (T)

B_p Penetration magnetic flux density (T)

B^* Full penetration magnetic flux density (T)

B_{pi}^* Magnetic flux density at which the first peak in χ' occurs (T)

B_{pg}^* Magnetic flux density at which the second peak in χ' occurs (T)

C

c Crystal lattice parameter (Å)

c_v Specific heat ($Jkg^{-1}K^{-1}$)

D

D Width of sample (m)

E

e   Electron charge ($1.6 \ x \ 10^{-19} \ C$)

$2e^*$ 2 e (C)

E Electric field (Vm^{-1})

E_F Fermi energy (eV)

F

f Frequency (Hz)

G

G Gibbs free energy (J)

G_n Gibbs free energy in normal state (J)

G_s Gibbs free energy in superconducting state (J)

H

H Magnetic field (A.m^{-1})

H_a Applied magnetic field (A.m^{-1})

H^* Maximum shielded magnetic field in Bean critical state model (A.m^{-1})

H_c Critical magnetic field (A.m^{-1})

H_{c1} Lower Critical magnetic field (A.m^{-1})

H_{c2} Upper Critical magnetic field (A.m^{-1})

$\hbar$ Reduced plank constant (1.1 x 10^{-34} J.s)

h Plank constant (6.62 x 10^{-34} J.s)

I

I Electric current (A)

I_s Electric current flowing through solenoid (A)

I_c Critical electric current (A)

I_{cjo} Dc Josephson current (A)

J

J_c Critical current density (A.m^{-2})

J_{ci} Intergranular critical current density (A.m^{-2})

J_{cg} Intragranular critical current density (A.m^{-2})

J_d Depairing current density (A.m^{-2})

J_h Screening current density (A.m^{-2})

J_i Transport current density (A.m^{-2})

J_s Superconducting Current density (A.m^{-2})

J_t Total current density (A.m^{-2})

J_y Current density along y-axis (A.m^{-2})

K

K   Constant

k GinzburgLandau parameter

K_B Boltzmann constant (1.4 x 10^{-23}JK^{-1})

L

L Length (m)

l Length (m)

L Inductance (Henry)

l_e Mean free path of electron (m)

M

M   Magnetisation (Am^{-1})

m Mass (kg)

m_e Mass of an electron (9.11 x10^{-31}kg)

m^* Mass of Cooper pair (kg)

N

N Number of turns

n_c	Number of charge carriers per unit volume (#.cm^{-3})
n	Number of turns carriers per unit length
n_s	Superconducting electron density (#.cm^{-3})

P

P	Power (W)
P_F	Fermi Momentum (kgms^{-1})
P_{ii}	Hydrostatic Pressure (Pa)

R

r	radius (m)
R	Resistance (Ω)

S

S	Entropy (J K^{-1} m^{-3})
S_n	Normal entropy (J K^{-1} m^{-3})
S_s	Superconducting entropy (J K^{-1} m^{-3})

T

T	Temperature (K)
T_c	Critical temperature (K)
T_{cm}	Curie Temperature (K)
t	Time (s)

V

v	Velocity (ms^{-1})
v_f	Fermi velocity (ms^{-1})
v_s	Electron velocity (ms^{-1})
V	Volume (m^3)
V_{sample}	Volume of superconducting sample (m^3)
V	Potential (calculated by Cottrell (1948) (J)

V_o	Amplitude of fundamental voltage (V)
V_{rms}	Root mean square voltage (V)
V_{ref}	Amplitude of the reference signal (V)
V_s	Amplitude of the fundamental signal (V)
V_1	Fundametal voltage (V)
V	Electric potential difference (V)
V'	In-phase component from lock-in amplifier (V^2)
V''	Out-of-phase component from lock-in amplifier (V^2)

W

ω	Angular frequency (rads^{-1})
W_q	Heat energy dissipated during one cycle of AC field (J)
W_m	Energy stored (J)

X

x	Distance (m)

Z

Z	Impedance (H)

Greek Letters

α	Phase difference (rad)
α'	Pickup coil's calibration coefficient constant ($A\ m^2 V^{-1} s^{-1}$)
α	GL phenomenological constant
α	Empirical constant, of order unity
β	GL phenomenological constant
λ_L	London penetration depth (m)

λ	Penetration depth (m)
δ	Penetration depth (m)
λ	Slip distance (m)
μ	Shear modulus (Pa)
μ_o	Permeability of free space (1.26×10^{-6} NA^{-2})
ε	Lattice dilation
ξ	Coherence length (m)
ξ_o	BCS coherence length (m)
ξ_P	Pippard coherence length (m)
ξ_{GL}	Ginzburg-Landau coherence length (m)
ρ	Resistivity (Ωm^{-1})
ρ_i	Residual resistivity (Ωm^{-1})
ρ_p	Phonon resistivity (Ωm^{-1})
ϱ	Dislocation density (number of dislocation.m^{-2})
σ_s	Surface energy (J)
σ	Stress (Pa)
φ	Phase (rad)
γ	Phase difference across junction (Rad)
Δ	Superconducting energy gap (eV)
Δ_0	Superconducting energy gap at zero Kelvin (eV)
χ	Magnetic susceptibility
χ'	Real magnetic susceptibility component
χ''	Imaginary magnetic susceptibility component
ψ	Wave function (m$^{-3/2}$)
υ	Poisson ratio

Acronyms

AC   Alternating current

BCS   Bardeen, Cooper and Schrieffer

BSSCO   Bismuth strontium calcium copper oxide

Ca   Calcium

DC   Direct current

DSP   Digital Signal Processing

GB   Grain boundary

YBCO   Yttrium barium and copper oxide ($YBa_2Cu_3O_{7-x}$)

PC   Personal computer

SEM   Scanning electron microscopy

XRD   X-ray diffraction

HTS   High temperature superconductors

rms   Root mean square

Contents

List of Figures

List of Tables

Chapter 1 Introduction

The focus of this research was to design and implement an AC susceptometer to study superconductors such as $YBa_2Cu_3O_{7-x}$ (Yttrium Barium Copper Oxide or for short YBCO), with a particular attention given to the grain boundary problem associated with granular YBCO samples. An AC susceptometer is made up of a primary coil, connected to an AC source and two sensing coils to measure the diamagnetic response of high-T_c materials.

Since the discovery of superconductivity, scientists have focussed efforts in improving the critical current density, J_c and the phase transitional temperature,T_c. The conventional experimental techniques used in studying T_c and J_c characteristics of superconductors mostly comprise of fixing instrumental wires to the specimens. Mechanically attached wires undergo thermal contraction at cryogenic temperatures leading to problems such as rupturing of contact wires [1]. Instead of characterising superconductors using conventional contact methods, magnetic measurement has proven to be a very powerful contactless method to study superconducting samples. The diamagnetic response of the specimens is measured in their superconducting phase in either AC or DC magnetic field. This is a very useful technique from which T_c and J_c (both intergranular and intragranular) can be measured. Moreover, other characterising parameters such as penetration depth, real and imaginary power dissipation due to sweeping magnetic field, can be determined [2]. Unlike the contact method, the apparatus used for magnetic measurement can be designed in such a way that it accommodates a big sample [3]. Hence, there is no need in cutting or destroying a specimen subjected to magnetic characterisation. So, a large sample can be preserved in its original state after it is subjected to AC susceptibility measurements. The apparatus used for magnetic measurement are AC susceptometer and DC magnetometer. The DC magnetometer uses a static field whereas in the

case of the AC susceptometer, the sample is subjected to a time-varying magnetic field. They both use sensing coils to sense the magnetic response of the material.

An AC susceptometer measures the magnetic response of material in their superconducting state. The AC susceptibility response is of interest when measured at different temperatures and magnetic fields. The magnetic susceptibility is separated as real and imaginary components by a lock-in amplifier. The scope of the research was to design and implement an AC susceptometer to study high-T_c materials with the specific focus to understand the grain boundary problems in Yttrium Barium Copper Oxide specimens. In this regard, a software-based AC susceptometer was designed and implemented to measure the relative in-phase and the relative out-of-phase AC susceptibilities of the specimens. The exact value of AC susceptibility was not established for this research since the emphasis was about trend changes. A unique feature of the AC susceptometer was the substitution of a conventional lock-in amplifier unit, like the *SR124-Analogue Lock-in Amplifier* designed by Stanford Research Systems, by a DSP system implemented using a personal computer and a data-acquisition electronic module. However, conventional lock-in amplifiers were used by many researchers to detect and measure accurately very small AC signals [3] [4]. For instance, M.I Yousif *et al* and Laurent *et al* used conventional lock-in amplifiers connected to a computer for data-acquisition purposes to characterise granular YBCO specimens [2] [3]. By the means of conventional lock-in amplifiers, AC susceptibility measurements were performed on high-T_c materials and using a critical state model such as Bean model, the critical current densities of the superconducting materials were estimated to characterise the granular structure of the materials [2] [3] [4].

The main motivation of designing a software-based lock-in amplifier was the high cost incurred in buying a dedicated lock-in amplifier unit like the *Standford Research SR124 Model* (which costs about $6500). Moreover, the implementation cost of the digital system was relatively low as it was implemented using a personal computer and a readily available data-acquisition module (the IOTech 2000 Daqbook module). Furthermore, unlike the conventional lock-in amplifier, it is versatile since it is programmable and the software platform used for its implementation is not entirely dedicated for the implementation of lock-in amplifiers. So, the lock-in amplifier can be easily customised when it is implemented in the software environment. At the time that the research was started, the material science laboratory had limited

experimental facilities to do AC susceptibility measurements. So, the DSP-enhanced lock-in amplifier implemented was expected to provide a flexible possibility of conducting reliable AC susceptibility measurements at low cost.

Bulk YBCO superconductor is notorious for having a low critical current. The problem of low critical current density of bulk YBCO samples is rooted in the fundamental microscopic structure of the material, in particular the intergranular material. This is due to the high anisotropic nature of the material and the countless number of grain boundaries in the material's lattice. The grain boundaries lead to the weak links effect which is a consequence of the weak couplings of the grains. So, YBCO lattice is made up of grains and grain boundaries which behave as networks of Josephson junctions, with the tunnelling of electrons at the weak links. Since the discovery of HTSs in 1987, scientists have extensively doped HTSs (such as YBCO, BSCCO) with a number of elements and compounds, for example silver and hydrogen, with the aim of improving the grain connections with mixed results. For instance, silver doping up to 10% wt has shown to improve grain connectivity, thus increasing the intergranular critical current density J_{ci} [5]. Hydrogen doping of YBCO leads to an increase in the resistivity of the material comparable to a "percolating system" with a large percolation factor [6]. This was attributed to a poorly conducting hydride phase or an inhomogeneous hydrogen distribution in the material [6].

The aim of hydrogen doping was to diffuse very small hydrogen molecules towards the grain boundaries by 'annealing experiment' (keeping the sample for some minutes at a constant cryogenic temperature which is higher than T_c), so as to relieve stresses at dislocations and improve the intergranular critical current which is stress dependent [7][8]. The intergranular critical current was deduced using the critical state model, modified version of Bean model, by measuring the AC susceptibility response of the material with respect to the magnetic field (< 20 mT) using the DSP-enhanced susceptometer. Knowing the variation of J_{ci}, information about the grain boundaries could be deduced.

The dissertation organisation is done as follows:

Chapter 2 introduces superconductivity, including a brief historical background and relevant theories that are related to this research. Furthermore, the critical state model, Bean model, used to estimate the critical current density of the specimens is discussed as well.

Chapter 3 discusses high-T_c materials in general, giving a particular attention to YBCO. The material science theory of grain, grain boundaries, dislocations and the formation of Cottrell atmosphere are also explored. It also details the effect of grain boundaries in HTSs ($YBa_2Cu_3O_{7-x}$).

Chapter 4 discusses the theory of AC susceptibility measurements and how this approach can be used to characterise superconducting specimens. The literature survey concerning AC susceptibility is also included.

Chapter 5 details the design and implementation of AC susceptibility apparatus. The software-based lock-in amplifier is also discussed in depth.

Chapter 6 details the bulk YBCO fabrication process and the hydrogenation experiment and it also covers the experimental works that were done for AC Susceptibility measurements and T_c characterisation.

Chapter 7 presents the results of the experiments. In depth discussion about the experimental results is covered. Moreover, the optical data gathered from scanning electron microscope is covered as well.

Chapter 8 concludes the dissertation's results and outlines the scope and directions for future work.

Part of the work detailed in this dissertation was published in a peer-reviewed conference journal, 2013 IEEE Africon conference. The title of the paper published is: "A DSP-Enhanced AC Susceptometer for Superconducting Samples".

Chapter 2   Superconductivity

2.1 Historical Background

In 1911, at the University of Leiden, Kamerlingh Onnes was investigating theories of electrical properties of metallic wires at low temperatures and he unexpectedly found that currents flow in certain materials without experiencing any resistance and without heat dissipation. He in fact discovered the superconducting state of materials [9]. The phenomenon of superconductivity was uncovered while Onnes was investigating the cooling of pure mercury with liquid helium. He discovered that pure mercury reaches superconducting state below a critical temperature, T_c of 4.2 K [9] [10]. Each superconducting material has a T_c, below which superconducting state is attained. Conversely, superconductivity cannot be defined only by the occurrence of zero electrical resistance at low temperature but also by the complete rejection of magnetic field (diamagnetism), which is another inherent property of a material in its superconducting state. The perfect diamagnetism of superconductors is referred to as the *Meissner effect*, named after Meissner, who discovered the perfect diamagnetism of superconductors in 1933. It is important to note that a superconductor has a transportation current (from terminal to terminal) and a screening current, which establishes a magnetic field equal and opposite to an external applied magnetic field (perfect diamagnetism characteristic of the superconductor). If the sum of the densities of these currents exceeds the critical current density J_c, superconductivity is destroyed. Furthermore, superconductors can be in general exposed to a certain amount of field, the critical magnetic field, beyond which superconductors lose their superconducting properties.

The discovery of the perfect diamagnetic response of superconductors by Meissner and Ochenfeld has led to the phenomenological theory formulated by the London brothers in 1935.

The London model describes superconductivity phenomenological and shows clearly that the super-current is confined to a certain surface penetration depth, known as the London penetration depth, λ, [11]. However, this theory does not explain the occurrence of the superconductivity phenomenon. Early attempts by scientists to explain the discovery of Onnes in 1911 were unsuccessful. John Bardeen, Leon Cooper, and Robert Schrieffer developed a microscopic quantum mechanical theory: the BCS theory (to be discussed later) in 1955. In the BCS framework, the interaction between electrons in the lattice vibration (phonons) is facilitated by the lattice itself and the interaction between electrons becomes attractive rather than repulsive. The electrons are bound together at low temperatures to form Cooper pairs [12].

Seven years before the BCS theory was formulated, Lev Landau and Ginzburg developed the Ginzburg-Landau Model of superconductivity. It was inspired from the Lev Landau's symmetry breaking theory during phase transition. A wave function which represents the number of superconducting carriers per unit volume was developed. From the expressions developed for the energy of superconductors, they included extra terms. One term included the fact that energy is saved if the superconducting charge carriers distribute uniformly and energy is required, if a sudden change in the number of carriers from one place to another occurs [13].

In the early 1950's, Alexei Abriskosov, a soviet physicist found that the superconductors can be classified into two types: type I and type II superconductors [14]. Type I shows a discontinuous response, if the magnetic field applied exceeds the critical value; whereas type II superconductors do not change abruptly to normal state once the critical field is attained.

In the 1960's, Brian Josephson fabricated a junction consisting of two superconductors connected through a weak insulator link where the Cooper electron pairs travel despite of the weak link [15]. This junction finds its application in SQUIDS magnetometer which can pick up very small magnetic field up to the order of one flux quantum.

The discovery of a superconducting material, which can withstand high magnetic field of the order of Tesla, is undeniably a significant application milestone in the construction of superconducting magnets. In this regard, Bernd Matthias, a German physicist, discovered in the 1960's that the Niobium Tin compound can withstand a magnetic field as high as 9 Tesla before reverting to normal state. This compound is still used in some superconducting magnet though

Niobium Titanium was discovered much later and has better physical characteristics and higher critical field. Throughout the 1970's, superconductivity went through a stage of consolidation and the transition temperature did not exceed 23 K (T_c for Niobium Germanium) until the 1980's when a major breakthrough occurred.

In 1986, Bednorz and Muller discovered superconductivity in ceramic, Ba-La-Cu-O system with a T_c approximately equals to 35 K [16]. Unsurprisingly, Bednorz and Muller won the Nobel Prize in Physics in 1987. After one year, Paul Chu and his collaborator Maw-Kuen Wu, from the University of Houston, discovered a ceramic superconductor similar to the 1986 discovery, Yttrium barium copper oxide, $YBa_2Cu_3O_{7-x}$ (0 < x < 6.5) with a T_c equal to 92.0 K. This was revolutionising because liquid Nitrogen, which has a boiling point of ≈ 77.0K under normal atmospheric conditions, could be used as a cooling agent to reach superconducting state. Nitrogen is a more widely available commodity than helium and the liquefaction of nitrogen is far less costly than that of helium. Since the discovery of YBCO, more copper oxide superconductors were discovered with even higher T_c.

2.2 Theories of Superconductivity in brief

2.2.1 Resistivity in Metallic Conductors

Researchers are familiar with metallic conductors such as copper wire. To understand the mechanism of electrical conduction in a piece of copper wire, it is important to use a simple material model. Copper is a crystalline solid. This means that it is made up of grains, atoms with the same crystallographic orientation arranged in a regular crystalline lattice. The atoms are in fact "swimming" in a sea of delocalised electrons. In other words, in the crystal lattice, there exist copper ions surrounded by delocalised electrons. If it is assumed that each copper atom gives up one electron, the density of free electron should be of the order of 10^{22} /cm^3. The positive copper ions and the electrons neutralise each other and copper is said to be electrically neutral, since the charges at quantum level are balanced. If an electric potential difference or an electric field is applied, the harmony of the electrons in the crystal lattice is disturbed and the

electrons will undergo an acceleration resulting in an electric current. For the sake of a thorough analysis, the ions are considered at 0 Kelvin in a perfect regular lattice. Since the atoms are arranged in a perfectly regular lattice, the delocalised electrons are not scattered during the conduction mechanism. However, the conduction electrons are scattered in practical situations due to imperfections present in the crystal lattice of the material. Examples of imperfections are dislocations, voids, interstitials, etc. The scattering of electrons contributes to the electrical resistance of the material

In practice, a piece of copper wire will eventually have an imperfect crystal lattice and consequently, conduction electrons are scattered at 0 K due to deviation of the material from the ideal crystallographic order of the material's lattice. The consequence of electron scattering in the crystal lattice is that the material develops some finite resistance at very low temperature. At zero kelvin, the material's resistivity is known as the residual resistivity, $\rho_{i.}$ With an increase in temperature, the electrons get scattered by thermal vibration of the lattice, known as phonons. Hence, both the imperfection in the crystal and the elevated temperature (which results in an increase in the kinetic energy of the atoms and electrons) contribute to the resistivity of the material. As a result, the resistivity of the material is proportional to the temperature. Resistivity due to the lattice vibrations is known as phonon resistivity, $\rho_p(T)$.

The equation below shows the temperature dependence for the resistivity of an imperfect crystalline metal,

$$\rho(T) = \rho_i + \rho_p(T). \tag{2.1}$$
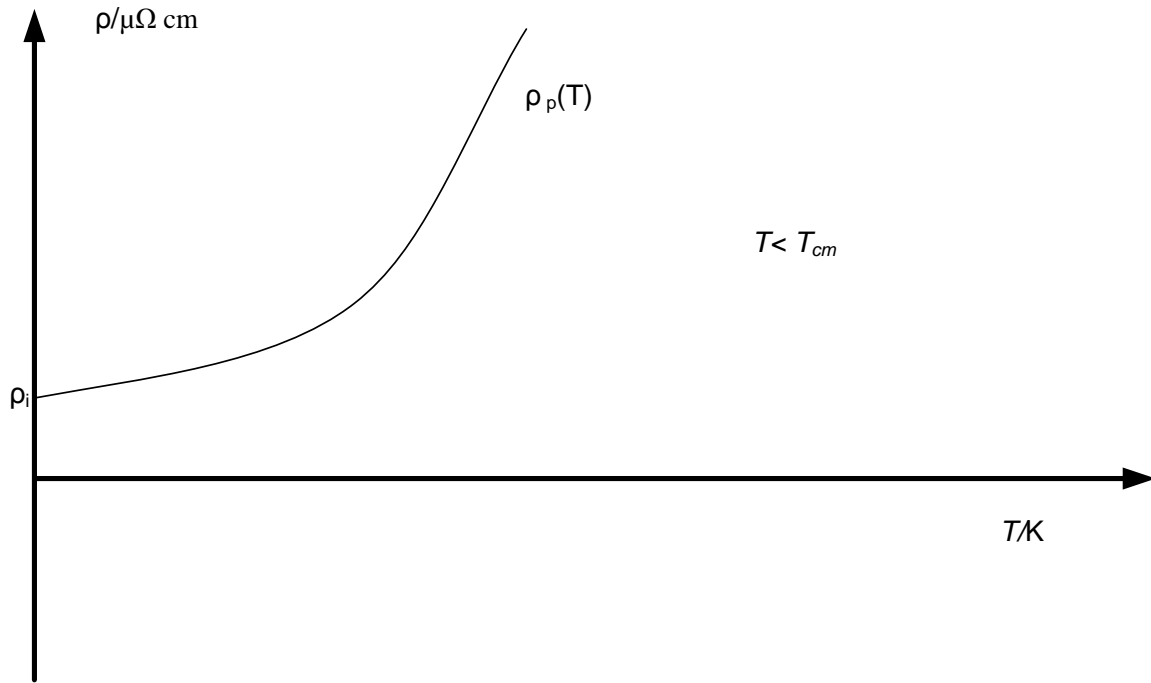
Figure 2. 1 Resistivity versus temperature for a typical metal.

Figure 2.1 shows how the resistivity of metallic conductors varies with temperature. At 0 K, ρ_i is zero due to crystallographic imperfection.

At absolute zero, the highest energy that electrons can possess is known as the Fermi energy, E_F,

$$E_F = \frac{(hc)^2}{8m_ec^2}\left(\frac{3n_c}{\pi}\right)^{\frac{2}{3}},\qquad(2.2)$$

Where h: Plank Constant $(6.62 \times 10^{-34}m^2\ kg\ /\ s)$

$\quad m_e$: mass of an electron

$\quad n_c$: number of charge carriers per unit volume.

$\quad T_{cm}$: curie temperature

The conduction electrons at Fermi energy propagate with the Fermi velocity, v_F. The Fermi velocity is related to the Fermi momentum, P_F,

$$P_F = m_e v_F,\qquad(2.3)$$

9

$$E_F = \frac{1}{2}P_F v_F. \tag{2.4}$$

$$E_F = \frac{P_F^2}{2m_e} \tag{2.5}$$

At $T = 0$ K, the conduction electrons propagate through the crystal with a characteristic Fermi velocity and they get scattered by impurities in the lattice of the material. Consequently, this gives rise to the concept of resistivity, i.e. the residual resistivity. The average distance covered by a conduction electron is known as the mean free path, l_e. The residual resistivity of a metal is given by the following equation,

$$\rho_i = \frac{m_e v_F}{n_c e^2 l_e}. \tag{2.6}$$

Note that in an isotropic material, the residual resistivity is equal in all directions whereas in anisotropic materials, the residual resistivity will vary with the different crystallographic orientation of the material and the resistivity in different directions in the material is tensors.

The shorter the average distance covered by the electrons, the higher will be the resistivity. So, the addition of impurities or increase in lattice imperfections will decrease the value of the average path and increase the resistivity. As described in the first section, superconductivity is the occurrence of zero resistivity taking place below a critical temperature. If a DC current flows through a superconductor, the current will keep on flowing indefinitely without decaying. If the theory which explains resistivity in metallic conductors is considered, this phenomena is rather puzzling because if we abide with the same model (electrons as charge carriers in the crystal lattice), it is rather impossible to correlate this theory to the fact that a metallic conductor like Hg loses its resistivity below a critical temperature. This gives rise to the question: *what happens to the scattered electrons?* Even at Fermi state, there is a path length which gives rise to the residual resistivity of the material. In the following sections, the theories which explain the phenomenon of superconductivity will be discussed.

2.2.2 BCS Theory

Before the BCS theory is explained, the discoveries which helped in the building up of this theory will be considered. A key finding which helped in the development of microscopic theory of superconductivity was the *Isotope Effect.* In 1950, Emmanuel Maxwell investigated the T_c of isotopes of different type I superconductors. The outcome of the experiments was that the transitional temperatures of the isotopes were dependent on the mass of the atoms. The critical temperature was found to be inversely proportional to the square of the atomic mass of the isotope concerned. So, it is evident that the mass of the atom influences directly the superconductivity phenomena. Bardeen, Cooper and Schrieffer found out that when a material is in its superconducting state, the electrons condense into a quantum fluid of highly correlated pairs of electrons [12]. Below T_c, an electron of a given momentum and spin, are weakly coupled with another electron forming a Cooper pair which does not obey exactly the Einstein-Bose distribution. Pairing of electrons is also a confounding concept because two electrons are not supposed to pair since they both carry a negative charge. Thus, there must be a mediator that causes the pairing and movement of electrons in the lattice. In fact, the mediator is the lattice which acts as an elastic wave mediating the pairing and motion of the electrons. The lattice consists of positive ions which disturbs the electron and results into a lattice distortion. Since the positive ions are massive (relatively speaking on a microscopic scale), they slowdown in the course and attract another electron. This is how the electrons pairing and motion are mediated. The distance between the two electrons is known as the coherence length. So, the superconducting properties of a material are affected by the mass of the positive ions in the crystal lattice (as demonstrated by the isotope effect) and the coherence length, ξ.

Based on the concept of Cooper Pairs, a superconductor can be considered as a mixture of two "fluids".
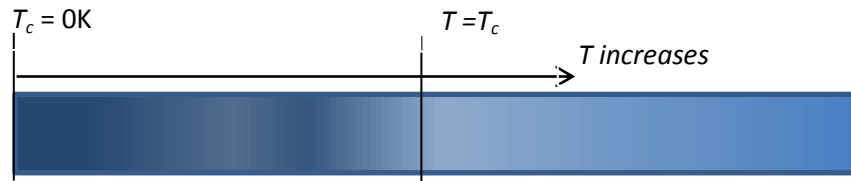
Figure 2. 2 Illustration of the Two Fluid Model showing the concentration of super electrons for temperatures lower than T_c.

As shown in Figure 2.2, at $T = 0$ K, all the electrons are Cooper Pairs (dark blue) whereas above T_c, all the electrons are normal electrons. As the temperature gets close to 0 K, the concentration of superelectrons increases, as indicated by the colour which becomes darker, as 0 K is approached.

2.2.3 The London Equations

In 1935, the London brothers proposed two equations which govern the electrical and magnetic properties in superconductors [11]. Their approach was a phenomenological one. They came to the conclusion that the electrodynamics equations have to be modified in order to describe the Meissner effect (the onset of screening current without a change in the magnetic field applied). Maxwell equations remain still valid. However, Ohm's law which deal with resistive conductors has to be modified to address superconductivity. To make this possible, the London brothers used a two-fluid model, considering two types of electrons: normal and superconducting ones. The phenomenon of superconductivity being associated with the non-scattering of superconducting electrons, the London brothers came with an approach which treats the non-scattered electrons as "super" electrons, where n_s is the number density of super-electrons. These electrons are not slowed down due to phonon vibration instead, they are freely accelerated by an Electric field E. The following equation of motion can be written as follows:

$$m\frac{dv_s}{dt} = eE,$$
(2.7)

v_s is the electrons' velocity.

Taking into consideration the existence of super electrons, the superconducting current density can be defined as follows:

$$J_S = n_s ev_s.$$
(2.8)

From Equation 2.7 and Equation 2.8,

$$\frac{dJ_S}{dt} = \frac{n_s e^2 E}{m}.$$
(2.9)

From the above equations, it is clear that the electrons undergo an acceleration which is proportional to the electric field showing the absence scattering due to phonon vibration or impurities. So Ohm's law (which defines resistance) is replaced by *accelerating superelectrons/supercurrent*. Note that E is the electric field, m is the mass of superelectron and e is the electronic charge of an electron.

Equation 2.9 shows the *First London equation* [11].

Using the Maxwell equation,

$$Curl E = -\frac{dB}{dt}. \tag{2.10}$$

Applying curl on both sides of Equation 2.9 and combining Equation 2.9 and Equation 2.10:

$$Curl \frac{dJ_s}{dt} = -\frac{n_s e^2 \mu_o H^{\cdot}}{m} \tag{2.11}$$

Note that

$$B = \mu_o H \tag{2.12}$$

Where B is the magnetic flux density, H is the magnetic field and μ_o is the permeability of vacuum.

B is considered on a macroscopic scale whereas H is considered on a microscopic scale, especially when dealing with the superconducting material at microscopic level.

Now considering Equation 2.11, Ohm's law and infinite conductivity, and assuming that:

$$\frac{dB}{dt} = 0,$$

$$Curl J_{\dot{s}} + \frac{n_s e^2 \mu_o H^{\cdot}}{m} = 0 \tag{2.13}$$

[11].

Equation 2.13 is the second London Equation [11]. It describes $B = 0$ at all-time in type I superconductor. This leads to flux expulsion and the definition of penetration depth, λ_l .

From the following Maxwell equation:

$$\mu_o J_s = CurlB, \tag{2.14}$$

Combining Equations 2.13 and 2.14 and the curl operator is then applied on both sides:

$$CurlCurlB^{.} + \frac{n_s\mu_o e^2 \, B^{.}}{m} = 0, \tag{2.15}$$

$$CurlCurlB^{.} = graddivB^{.} - \nabla^2 B^{.}. \tag{2.16}$$

(Note that $divB^{.} = 0$)

So, Equation 2.15 becomes:

$$CurlCurlB^{.} = -\nabla^2 B^{.}, \tag{2.17}$$

$$\nabla^2 B^{.} = \frac{B^{.}}{\alpha}. \tag{2.18}$$

Where;

$$\alpha = \frac{m}{n_s\mu_o e^2}. \tag{2.19}$$

Considering one dimension:

$$\frac{\delta^2 B^{.}}{\delta^2 x} = -\frac{B^{.}}{\alpha}, \tag{2.20}$$

$$B^{.}(x) = -\alpha \frac{\delta^2 \, B^{.}(x)}{\delta x^2}. \tag{2.21}$$

The solution to the above differential equation is:

$$B^{.}(x) = B^{.}_A \exp(\frac{-x}{\sqrt{\alpha}}). \tag{2.22}$$

Experiments have shown that for a superconductor : $B^{.} = B = 0$ within a superconductor.

Therefore;

$$B(x) = B_A \exp(\frac{-x}{\sqrt{\alpha}}). \tag{2.23}$$

Let $\lambda_L = \sqrt{\alpha}$

Where, λ_L is the London penetration depth.

B(x)

B_A

$B(x)= B_A \exp (-x/\sqrt{\alpha})$

x
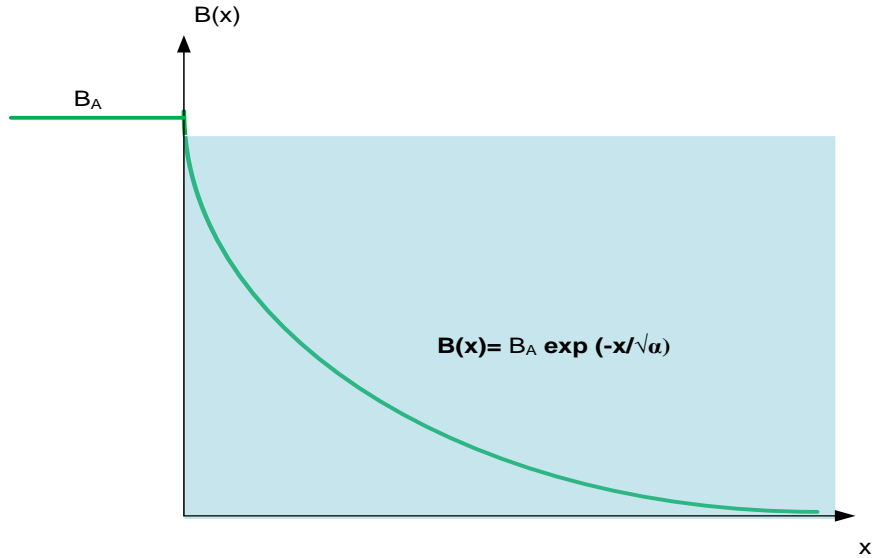
Figure 2. 3 Exponential decay of *B* as the magnetic field travels though the material.

The field decreases exponentially through the material until it reaches a value of zero when it goes through the length scale λ_L through the material as shown in Figure 2.3 (from Equation 2.14).

$$\frac{\delta B}{\delta x} = -\mu_o J_y \tag{2.24}$$

From Equation 2.23;

$$\frac{\delta B}{\delta x} = \frac{B_A}{\lambda_L} \exp\left(\frac{-x}{\lambda_L}\right), \tag{2.25}$$

$$J_y = \frac{B_A}{\mu_o \lambda_L} \exp\left(\frac{-x}{\lambda_L}\right), \tag{2.26}$$

$$J_y = J_A \exp\left(\frac{-x}{\lambda_L}\right), \tag{2.27}$$

So, we can conclude that the current flows within a penetration depth of λ_L through the superconductor as demonstrated by Equation 2.27. The supercurrent density decreases exponentially as the current gets into the material.

15

The London equations make way to a phenomenological model of superconductivity. They describe the phenomenon of superconductivity but do not explain it. Based on the fact that superconductors expel magnetic field from their interior core, the London brothers show the concept of penetration depth. It is demonstrated that the magnetic field does penetrate the material but it falls exponentially as the penetration distance increases, to zero. Moreover, the electric current flows only at the surface and it behaves in a similar way to the magnetic field, i.e., it falls exponentially on a length scale of λ_L.

2.2.4 The Coherence Length, ξ

From the London equations, a very important parameter, the penetration depth λ_L, was derived. However, the London brothers considered the charge carriers during superconducting state as being single electrons (since the existence of Cooper Pairs was unknown).

The mutual interaction and correlation of the behaviour of electrons in Cooper pairs over some distance is known as coherence in superconductivity, where the maximum distance is called the coherence length ξ_o (BCS coeherence length). ξ_o is related to the BCS energy gap $\Delta_o \approx K_B T_c$ by

$$\xi_o = \frac{\hbar v_f}{\pi K_B T_c}$$

(2.28)

[12].

Where K_B is the Boltzmann constant, v_f is the Fermi velocity, $\hbar$ is the reduced plank constant (1.1 x 10^{-34} J.s),

However, in 1953, Sir Brian Pippard introduced the Pippard coherence length ξ_p, while proposing a nonlocal generalisation of London Equation (Equation 2.9).

The Pippard coherence length can be related to the BCS coherence length by the following:

$$\frac{1}{\xi_p} = \frac{1}{\xi_o} + \frac{1}{\alpha l_e}.$$

(2.29)

16

α is known as a constant of order unity. As the mean path length of the super electrons decreases due to lattice scattering, the coherence length also decreases as shown by Equation 2.29. Equation 2.29 can be experimentally verified by the inclusion of impurities in a superconductor therefore, l_e decreases and thereby decreasing ξ_p. It was expected that a decrease in the electron mean free path l_e occurs due to scattering from impurities and ions, leading to a reduction in the coherence length.

An interesting result of the inclusion experiment is the penetration depth that increases as ξ_o exceeds l_e , allowing a type-II like behaviour by suitable microstructural modification of an otherwise type-I superconductor.

2.2.5 Magnetic Gibbs Free Energy

The transition from normal to superconducting state is classified as second order as the entropy and volume of the system are continuous at the transition temperature. There are no abrupt changes during this transition. In section 2.2.6, the Ginsburg-Landau theory which is related to second order transition will be discussed.

In nature, a system will tend to move from order to disorder, i.e., from low entropy to high entropy isolated system. The superconducting state is preferred over the normal state below the critical temperature, T_c, meaning that it is a lower energy state. Not only is the state of a superconductor sensitive to temperature but to the magnetic field as well. To study the effect of magnetic field on a superconducting isolated system, the Gibbs potential/Gibbs free energy, G (T,H) is used. In general, Gibbs free energy is an indicator of the spontaneity with which a reaction will take place [17]. In any spontaneous system, the latter will tend to decrease its enthalpy and increase its entropy. A combination of these two parameters leads to the indicator or concept, Gibbs free energy.

Gibbs free energy in general is given by:

$$G\,(T,H) = U - TS + U_M. \tag{2.30}$$

17

Where U, T, S and U_M are the internal energy, temperature, entropy and the magnetic energy respectively.

For a superconductor placed in an applied magnetic field, H_a, the magnetic energy is

$$U_M = \int_0^{H_a} \mu_o H dM = -\int_0^{H_a} \mu_o H \chi dH = -\frac{1}{2}\mu_o \chi H_a^2 , \qquad (2.31)$$

$$G(T, H_a) = U - TS - \frac{1}{2}\mu_o \chi H_a^2, \qquad (2.32)$$

$$dG = dU - TdS - SdT - \mu_o H dM - \mu_o M dH, \qquad (2.33)$$

χ is the magnetic susceptibility, M is the Magnetisation and μ_o is the permeability of vacuum.

From the second law of thermodynamics,

$$dU = TdS + \mu_o H dM. \qquad (2.34)$$

Therefore;

$$dG = -SdT - \mu_o M dH. \qquad (2.35)$$

Equation 2.35 is integrated on both sides for an isothermal magnetisation;

$$G(T, H_a) - G(T, 0) = -\frac{1}{2}\mu_o \chi H_a^2. \qquad (2.36)$$

In superconducting state, $\chi = -1$

$$G_s(T, H_a) - G_s(T, 0) = \frac{1}{2}\mu_o H_a^2. \qquad (2.37)$$

In normal state, $\chi \approx 0$

$$G_n(T, H_a) = G_n(T, 0). \qquad (2.38)$$

At the critical field H_c, the normal to superconducting phases are in equilibrium at the same temperature and field,

$$G_n(T, H_c) = G_s(T, H_c) = G_n(T, 0) = G_s(T, 0) + \frac{1}{2}\mu_o H_a^2 \qquad (2.39)$$

From Equation 2.37 to Equation 2.39, the following can be deduced;

$$G_n(T, 0) - G_s(T, 0) = \frac{1}{2}\mu_o \chi H_c^2. \qquad (2.40)$$

So, if $H_a > H_c$, $G_n(T,0) - G_s(T,0)$ (Equation 2.40) is smaller than the magnetic expression $\frac{1}{2}\mu_o\chi H_a^2$. Hence, the normal state prevails. Otherwise, the superconducting state prevails. This is illustrated in Figure 2.4.

G_n and G_s are Gibbs free energy in normal state and superconducting state respectively.

From Equation 2.39, the reduction of free energy in forming the superconducting state can be known. Therefore, it provides a direct measure of the condensation energy of the superconducting phase.
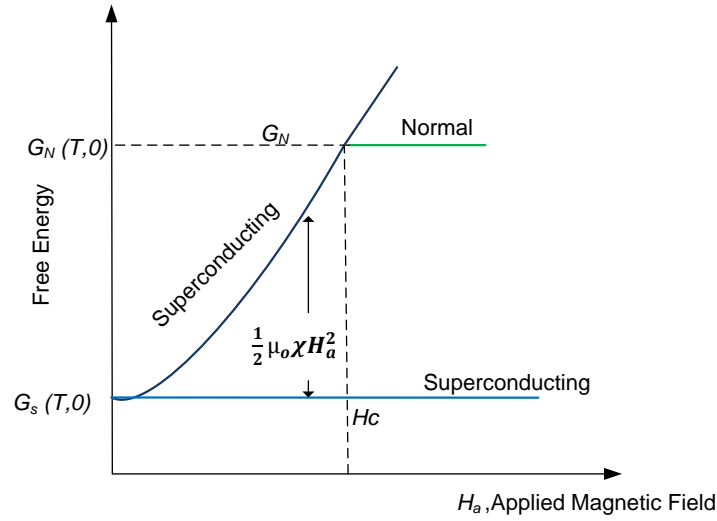
Figure 2. 4 Free energy v/s applied magnetic field.

Note that the entropy can be expressed as

$$S = - \left[\frac{\delta G}{\delta T}\right]_H.$$
(2.41)

From Equation 2.40 and 2.41;

$$S_{n=} S_s - \frac{1}{2}\mu_o \frac{d}{dT}(H_c^2),$$
(2.42)

$$S_{n=} S_s - \mu_o H_c \frac{dH_c}{dT},$$
(2.43)

The specific heat, is related to S and H_c:

$$C_v = T\left(\frac{\delta S}{\delta T}\right)H_c.$$
(2.44)

2.2.6 The Ginzburg-Landau Theory in brief

One simple example to demonstrate a second order transition is when a lump of iron loses its magnetism above a particular temperature known as the *Curie temperature*. For instance, the curie temperature of iron is 1043 K. Lev Landau used the concept of symmetry and order to explain such a transition [18] [19]. When a material is magnetised, the atoms are aligned in the same direction whereas the contrary happens when a material is demagnetised, the atoms are randomly oriented. The magnetised material is said to be more ordered but less symmetrical than the demagnetised material. In brief, the higher the symmetry, the lesser is the order and vice versa. This was the key analysis conducted by Lev landau. He suggested that there should be a parameter that measures order and this parameter is called the *order parameter.*

Landau concluded that any second order system can be considered in the same manner. Depending of the system, the magnetisation parameter used for magnetisation phenomena is replaced by another quantity which is the order parameter for any particular second order transition.

This approach inspired the development of the Ginzburg-Landau theory of superconductivity. The theory proposed the use of a macroscopic quantum wave function $\psi(r)$ which is equivalent to an order parameter.

The Ginzburg-Landau theory of superconductivity [20] which focuses mainly on superconducting electrons rather than on excitation was proposed in 1950, seven years before Bardeen, Cooper and Schrieffer came with the BCS theory. Previously, the London equations were derived. It can be seen that with the London Brothers' approach, the quantum phenomena of electron pairing is not considered (Cooper pairs were unknown to them at that time) and this theory has its limits when dealing with spatial inhomogeneities which are encountered by type-II superconductors in the mixed state. The Ginzburg-Landau theory (GL theory) predicted the type-II superconducting behaviour and magnetic vortices quantisation. Ginzburg and Landau proposed the first complete quantum theory of superconductivity. The Ginzburg-Landau theory is based on Quantum mechanics, electrodynamics and thermodynamics. It is thus better equipped to deal with the characteristics of spatial inhomogeneities.

The GL theory proposed an order parameter for any second order transition system. With regard to superconductivity, Ginzburg and Landau proposed a pseudo-complex microscopic wave funcion, ψ, as superconducting order parameter. ψ is related to the number density of super electrons by:

$$n_s = 2|\psi|^2. \tag{2.45}$$

The complex order parameter is expressed by the Equation 2.46:

$$\psi(r) = |\psi(r)|e^{i\varphi(r)}, \tag{2.46}$$

$\varphi(r)$ is a phase term related to current [20].

Base on the GL theory, it was deduced that near the second order transition, the order parameter is small and has a slow spatial variation and the free energy can be expressed as a power series in terms of $|\psi|^2$:

$$G_s(r,T) = G_s(r,T) + \alpha|\psi|^2 + \frac{\beta}{2}|\psi|^4 + \frac{1}{2m_e^*}\left|(-i\hbar\nabla - e^* A_p)\right|^2 + \frac{\mu_o h^2}{2} \tag{2.47}$$

$\alpha = a(T - T_M)$ which is approximated by a first order Taylor expansion, $\beta > 0$. A_p is a vector potential of magnetic field, defined as $\mu_o h = \nabla . A_p$.

2.2.7 TYPE-II Superconductors

Parameter k, known as the Ginzburg-Landau parameter is defined as

$$k = \frac{\lambda}{\xi_{GL}}, \tag{2.48}$$

k can be considered as a characteristic of a material.

Where,

$$\xi_{GL} = \frac{\hbar^2}{2m^*|\alpha|}. \tag{2.49}$$

ξ_{GL} is the GL coherence length, m^* is the mass of a Cooper pair, $\hbar$ is the reduced plank constant(1.1×10^{-34} J.s), λ is the penetration depth and α is a phenomenological parameter introduced by GL theory.

$$\alpha = -\frac{e^{*2}}{m^*}\mu_o H_c \lambda^2 \ . \tag{2.50}$$

Before the 1960's, the scientific community was unaware of the existence of type-II superconductors. Superconductors were not classified and were believed to have similar general characteristics. In 1957 (same year Bardeen, Cooper and Schrieffer proposed the BCS theory), Abrikosov published a paper [14] describing his investigation on the parameter k in the GL theory which is known *as Ginzberg-Landau parameter.* The GL parameter k is an important parameter that characterises superconductors as being type-I ($k < 1/\sqrt{2}$) and type-II ($k > 1/\sqrt{2}$). Abriskosov did investigate what would happen if the value of k is large instead of small, i.e., $\xi \ll \lambda$, leading to a negative surface energy. He found that for superconductors with negative surface energy, the subdivision into normal and superconducting domains proceeds until it is limited by the characteristic length ξ.

Surface energy is defined as,

$$\sigma_s = (\xi - \lambda)\frac{1}{2}\mu_o H_c^2. \tag{2.51}$$
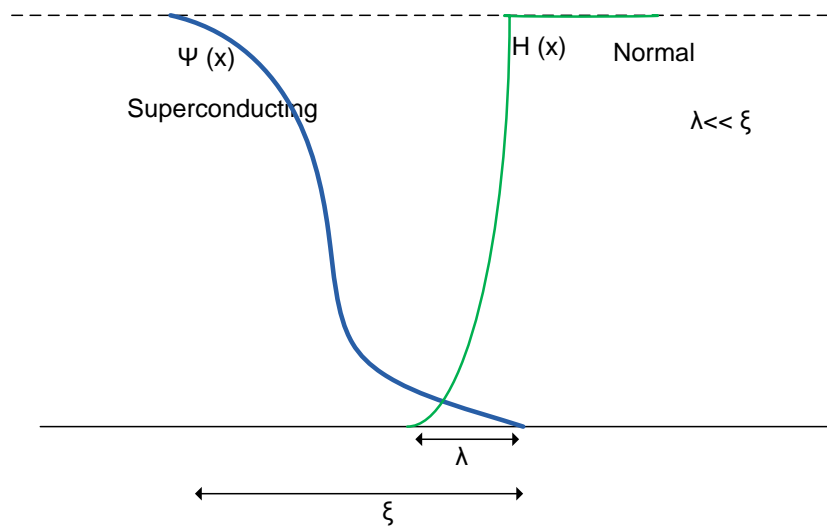
Figure 2. 5 Conditions for type-I superconductors.
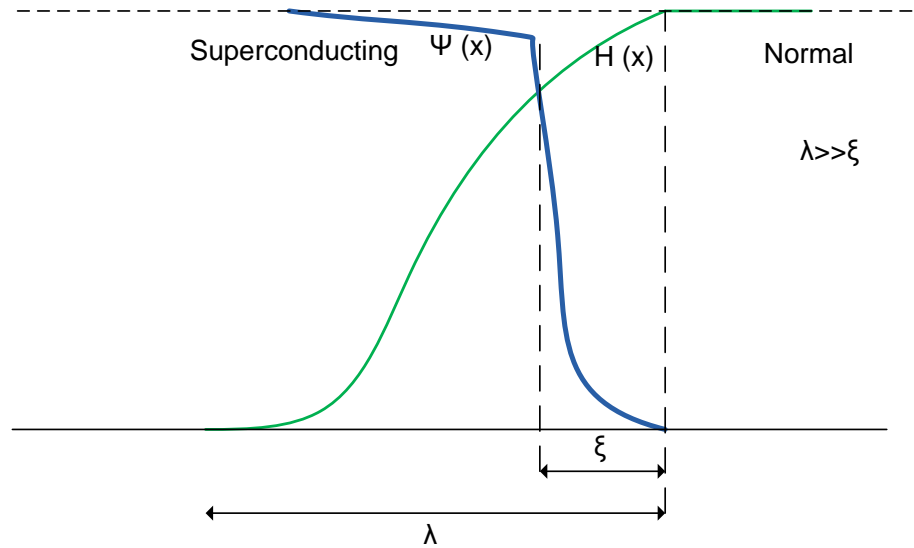
Figure 2. 6 Conditions for type-II superconductors.

As this behaviour is different from the intermediate state of conventional superconductors, Abrikosov classified superconductors as type-I ($\xi \gg \lambda$) and type-II ($\xi \ll \lambda$). Type-I superconductors' behaviour is shown in Figure 2.5. It is known that conventional superconductors show a discontinuous interruption in superconductivity when the critical field H_c is reached. However, Abrikosov found out that for type-II superconductors, there is not an instantaneous breakdown of superconductivity in first order transition at H_c. Figure 2.5 and Figure 2.6, represent spatial dependence of the order parameter$\psi(x)$ and the magnetic field $H(x)$ at the superconductor-normal interface, respectively type-I and type-II superconductors. The magnetic response of type-I and type-II superconductors will be discussed in details in Chapter 3.

2.2.8 Josephson Effects

Two metallic specimens in their normal state separated by a thin layer of insulation barrier are considered: for example, two pieces of Aluminium separated by a thin film of aluminium oxide. If the film is sufficiently thin, electrons will propagate through the insulating barrier from one side of the metal to the other. Otherwise, no electron propagation will take place. Hence, with a thin insulation barrier, there is a good probability that an electron will tunnel through the barrier. This is a well understood quantum phenomena and is known as tunnelling. Tunnelling not only takes place in junctions or physical barriers but in HTS's grain boundaries which are 'weak links', where the critical current is suppressed.

Dc Josephson Effect

Using the quantum mechanical theory and the BCS theory, Brian Josephson predicted in 1962 that if two superconductors are separated by a sufficiently thin layer of insulator, weak current of Cooper Pairs is probable to tunnel through the barrier with no potential drop across the insulator. This phenomenon is called the *Dc Josephson Effect* [15].

Let us consider two separate identical superconductors which are isolated from each other. Each superconductor is described by its wave function, $\psi_i = |\psi_i| e^{i\varphi(r)}$, which is not inter-related. Now these two specimens are brought together with a thin insulating layer between them. The amplitudes of the individual wave function are the same, if the two superconducting specimens are kept at the same temperature. The interaction of the wavefunctions results into a new wavefunction. The wavefunctions have the same amplitudes but different phases. Hence, phase coherence is directly related to the establishment of a 'weak link' contact.

In a Josephson junction, the wavefunctions on both sides of the junctions become locked with a phase difference $\gamma = \varphi_A - \varphi_B$ (between the two superconductors), a super current I_{cj} can tunnel between the two superconductors with no voltage drop [15].

$$I_{cj} = I_{cjo} \, sin\gamma. \qquad (2.52)$$

If the current through the junction I_{cjo} exceeds the maximum critical tunnel current $I_{cj}(0)$ (I_{cj} at zero Kelvin), the junction returns to normal resistive state and a potential drop appears across the junction.

The critical current varies as a function of temperature.

2.2.9 Bean Model

C.P Bean developed the critical state model, also known as the Bean model, for a slab hard superconducting material [21] [22]. The basic premium of this theory is the assumption that there exists two distinct macroscopic superconducting states [21] [22]. Bean defined the two states of current flow that are possible within the given axis of the magnetic field: zero current for the regions exposed to a magnetic field and maximum current flowing perpendicularly to the applied field axis (which can be positive and negative). The directions of the current depend on the orientation/direction of the applied magnetic field. The orientation of J_c results from the right-hand law. For instance, B which is acting in the y-direction, produces a critical current in the z-direction if the specimen is in the x-direction. From Amper law, $CurlB = \mu_o J$. This accounts for a decrease in the magnetic flux density with distance along the superconducting specimen (slab in shape).

Bean defines the maximum shielded magnetic field as H^*, $H^* = \frac{4\pi R J_c}{10}$ in Oersted (R is the mean radius of the sample) [21]. The corresponding magnetic flux density is defined as B^* for a filament sample; the maximum screenable field is reached at full penetration depth, if the radius of the specimen is larger than the London's penetration depth. In the critical state model, J_c is independent of the magnetic field. In this regard, the critical current density follows a step function which is reached despite a variation in the magnetic field and this function does not change (remains a step one) for different values of H as shown in the Figure 2.7. Only the penetration depth varies if the value of the external field changes.
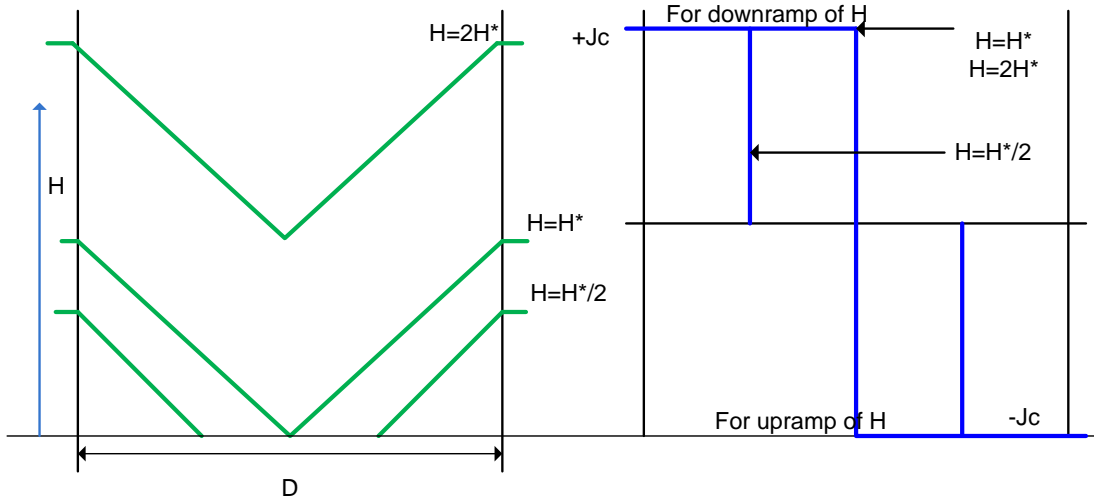
Figure 2. 7 Superconducting slab of width **D** with an external magnetic field **H** applied on the outside in accordance to Bean critical state model [21] [22].

Consider an applied magnetic field which changes orientation, current vectors which point in different directions are generated. The magnetic field in the interior of the material (slab cross-section sample) which extends infinitely in the y and z directions derives from Maxwell's equations:

$$Curl\ H^* = J_c\ ,\qquad\qquad (2.53)$$

$$\frac{\partial H_y}{\partial x} = J_c.\qquad\qquad (2.54)$$

Where J_c , the current density points in the z-direction.

If the applied field is oriented in the y-direction of the coordinate system, the critical current density will point in the z-direction, due to the right-hand law/rule for a slab-like sample with the width D (R= D/2) in the x-direction.

Equation 2.54 is valid in the plane of the superconducting slab cross-section and $J_c = J_z$ is constant according to the Bean model.

The penetration magnetic field, B_p, which is the magnetic flux density reached when the sample (of width D) gets fully penetrated is:

26

$$B_p = B^* = \mu_o J_c \frac{D}{2}.$$
(2.55)

For the Critical State Model, the maximum screenable field is identical to B^*.

Consider a superconducting slab subjected to a magnetic field. The distribution of J_c (perpendicular to the front section of the slab) is shown as well as the induced magnetic field, $B = \mu_o H$ along the slab axis orientation. Due to the fact that the magnetic field induced is independent of the current density, the slope of the field is assumed to be constant. The magnetic field profile for increasing magnetic field is shown in Figure 2.8.

(a)   (b)
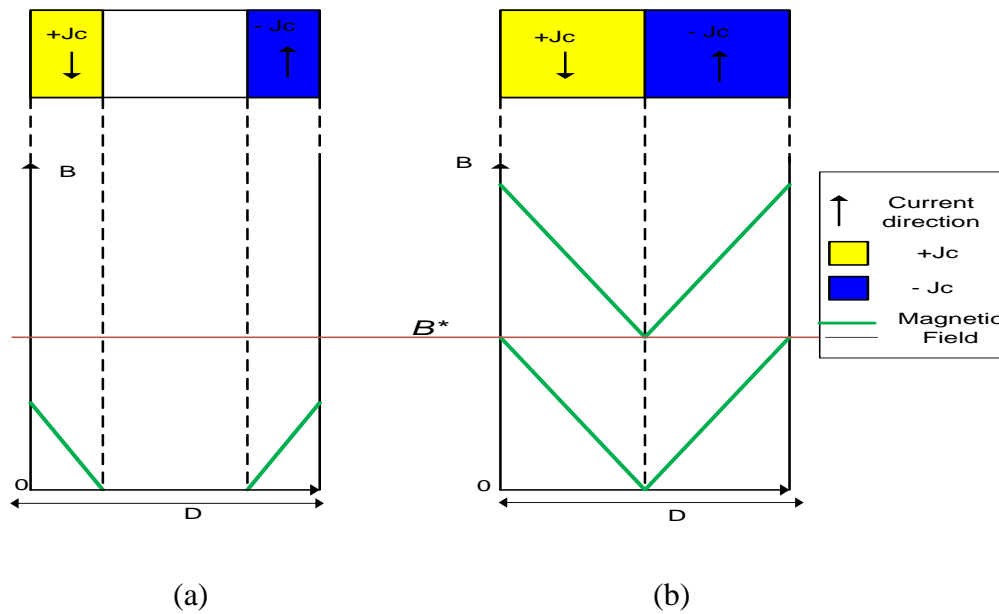
Figure 2. 8 Type-II superconducting slab of width D with one dimensional increasing external magnetic field H for different penetration states.

The magnetic field profile for decreasing magnetic field is shown in Figure 2.9.
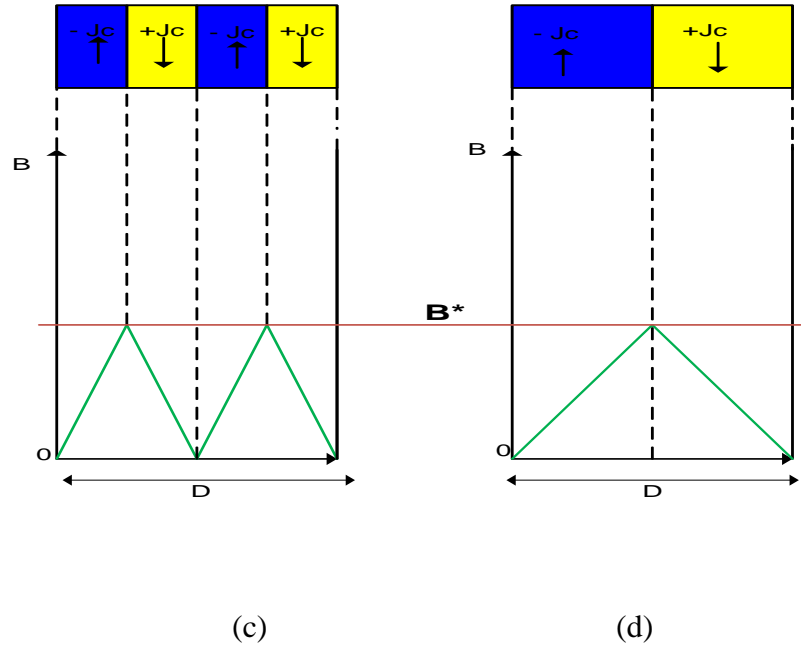
Figure 2. 9 Type-II superconducting slab of width D with one dimensional decreasing external magnetic field H for different penetration states.

Referring to Figure 2.8 and Figure 2.9:

(a) The external field is raised to a value below B^*. This results into field free region and so the slab is not fully penetrated.

(b) The external field is raised to a maximum value of B^* and above B^*. The field fully penetrates the slab.

(c) The applied field is now reduced when the previous field has been increased to B^*. An additional pair of bi-directional current is induced due to the formation of an emf. Even if the field decreases to zero, there is still magnetic flux trapped inside the superconducting slab.

(d) The superconducting specimen is fully penetrated ($B \geq B^*$) after reducing the magnetic field.

The Critical State Model (CSM) proposed by Bean is eventually a simplified CSM stating that J_c is independent of the magnitude of the applied field. Apart Bean Model, other models such as Kim Model advocates a Critical State Model where $J_c = f(H)$ [23]

Chapter 3 High Temperature Superconductors

3.1 General Description of High Temperature Superconductor

Hazen and Al. [24] and other groups of scientists have shown that Oxide High Temperature Superconductors (HTS) are members of crystallographic family, known as Perovskites. Perovskites are ceramics with a specific atomic arrangement. The general formula for perovskites is ABC_3. Pervoskites consist of cubes made of three distinct elements in the ratio of 1:1:3. A and B are metallic cations (like Y and Ba in YBCO). A is found at the centre of each cube, B ions occupy all the eight corners of the cubes and C, which is a non-metallic anions, is situated at the mid-point of the cube`s twelve edges as shown in Figure 3.1.
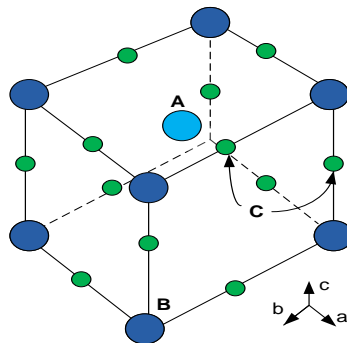
Figure 3. 1 ABC_3 perovskite structure of HTSs.

High temperature superconductors are mostly cuprate based compounds with a layered structured consisting of CuO_2 layers and each Cu atom in the CuO_2 plane is held by strong covalent bonds. Moreover, the Cu cations have mixed valency ranging from +2 to +3. Superconductivity is largely influenced by the transfer of charges to and from the copper oxide layers. It is interesting to consider the fact that when a rare earth element (RE) replaces Yttrium (Y) in a HTSC (such as $Y_1Ba_2Cu_3O_{7-x}$ which is also written as YBCO), the superconducting

properties do not change much. As shown in Table 3.1, the salient parameters such as ξ, J_c and H_c vary with respect to the crystallographic plane. This gives an indication that HTSs are highly anisotropic in nature. Apart from being anisotropic, HTSs are made up of countless number of grains and grain boundaries which influence the physical property of the HTSs. The granular nature of HTSs is discussed in section 3.4
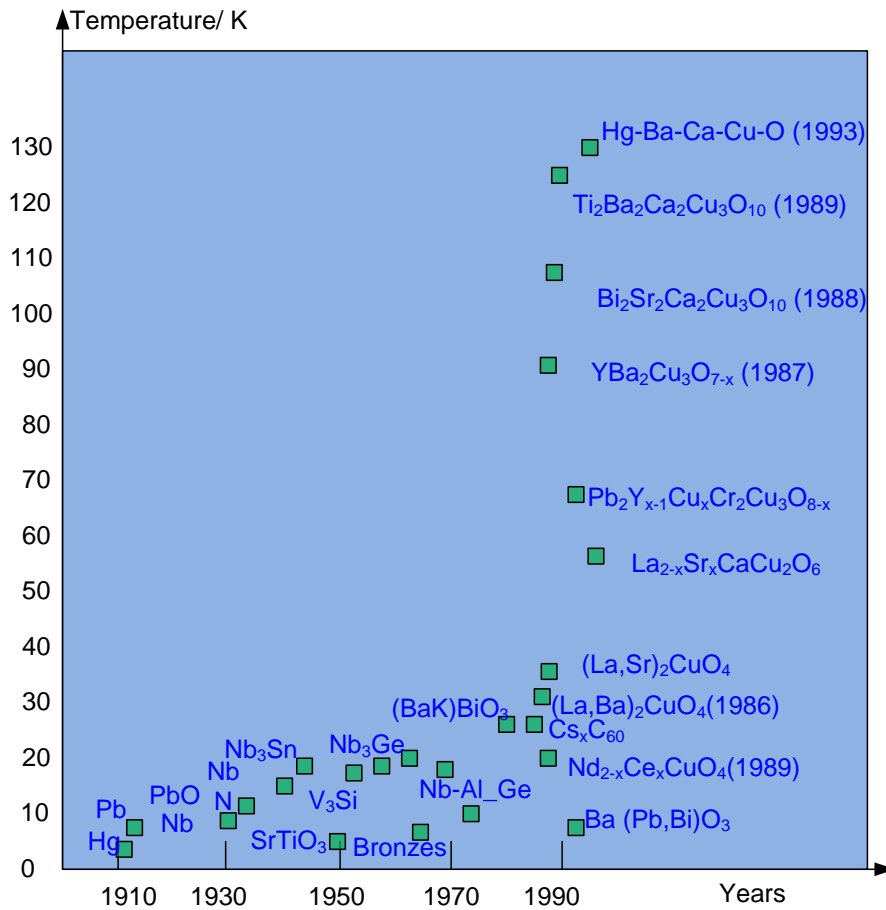
Figure 3. 2 Critical temperature v/s year of discovery.

The above graph shows the years of discovery and the T_c of superconducting compounds, including HTSs. HTSs were discovery in the 1980's and they are mostly copper oxide based compounds.

The main concern for this research work was about Yttrium Barium and Copper Oxide HTSs. They were synthetized and tested doing both AC susceptibility and resistive measurements.

3.2 Yttrium Barium Copper Oxide Superconductor

3.2.1 Discovery and General Description of YBCO

In 1987, Wu *et al* discovered a copper oxide superconductor; Yttrium Barium Copper Oxide, having the chemical formula of $YBa_2Cu_3O_{7-x}$, and which is commonly known as YBCO, with a T_c of 92.0 K [25]. YBCO is the superconductor that was used for this research. In general, YBCO is synthetized by mixing the correct ratio of constituent oxides, ground them and sintered them at about 920 ^{o}C under an oxygen atmosphere. For this research work, readily available YBCO powder was pressed and sintered at about 920 ^{o}C under an oxygen atmosphere to make YBCO pellets.

$YBa_2Cu_3O_{7-x}$ (x<0.6) has an orthorhombic crystalline structure, meaning that the a-axis length and the b-axis length are not equal (a =3.83 A, b = 3.88A). YBCO has a layered structure consisting of copper oxide planes together with Barium and Yttrium in the crystal structure.
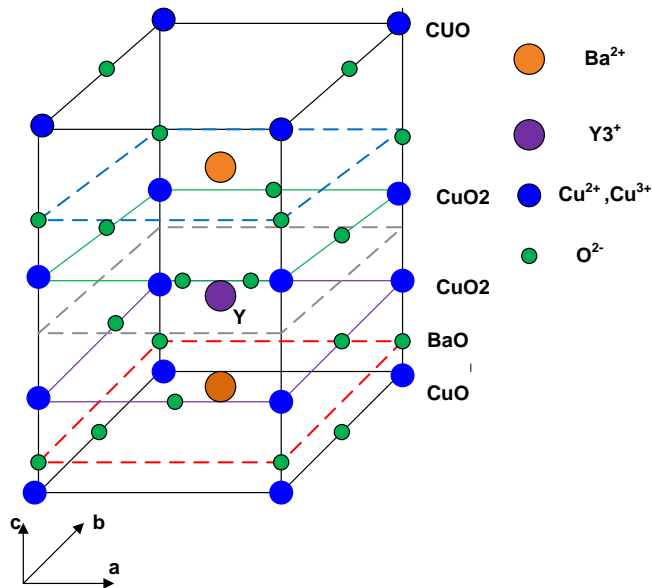
Figure 3. 3 Crystal structure of YBCO.

A unit cell of YBCO, as depicted in Figure 3.3, contains the following:

- A layer of barium, oxide (BaO)
- A layer of yttrium, short of four oxygen.
- A layer of copper oxide (Cu-O), where Cu2+ is surrounded by five oxygen anions to form a polyhedron.
- A layer of Cu-O having copper surrounded by four oxygen ions.

3.2.2 Variation of YBCO Properties with Oxygen Stoichiometry

Varying the oxygen contents directly affects the properties of $YBa_2Cu_3O_{7-x}$. The lattice parameters of YBCO vary with oxygen content as shown in the Figure 3.4 and Figure 3.5 [26]. The structure of YBCO is perfectly orthorhombic at $x = 0$. As the Oxygen content decreases, the structure of YBCO deviates from its orthorhombic configuration. Moreover, the oxygen content affects the onset of superconductivity of YBCO as shown by Figure 3.6, showing the relationship between T_c and the oxygen content of YBCO.

32
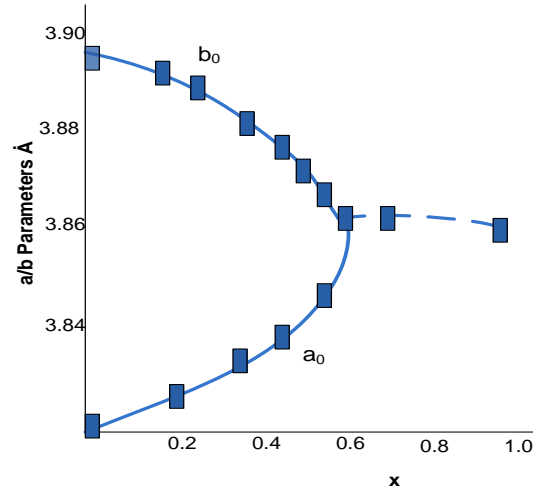
Figure 3. 4 Variation of unit cell a-b parameters of YBCO with oxygen stoichiometry.[26]
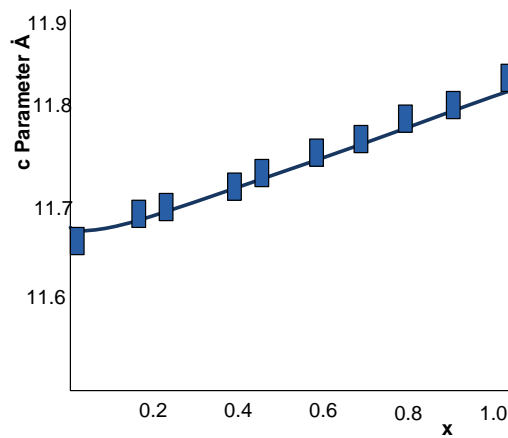
Figure 3. 5 Variation of unit cell c parameter of YBCO with oxygen stoichiometry.[26]

Moreover, the doping of YBCO with oxygen affects the amount of charge carriers impacting directly on the superconducting properties of $YBa_2Cu_3O_{7-x}$. Varying the oxygen content causes a transformation of the electrical property of $YBa_2Cu_3O_{7-x}$, which varies from insulating to superconducting.

For

$0.6 \leq x \leq 1.0$: $YBa_2Cu_3O_{7-x}$ is not superconducting.

The oxygen content can be easily varied by doping mechanism; either by increasing or decreasing the oxygen content along the b-axis. Understanding the dependence of the state of YBCO on the oxygen content is extremely important while synthetizing it. Hence, annealing in an oxygen atmosphere is a crucial step in superconducting YBCO sintering, so that the right amount of oxygen is absorbed.

The T_c of YBCO is around 90.0 K for x = 0 to x = 0.2. From Figure 3.6, a plateau is observed at 60 K for x = 0.3 to 0.4 [27]. T_c is approximately 50 K when x = 0.5. No clear oxygen vacancy ordering has been found in the plateau region (x = 0.3 to 0.4). For $YBa_2Cu_3O_{6.5}$ (x = 0.5), fully oxygenated copper oxide chains are present along the b-axis, alternating with vacant O_4 sites. Therefore, for x =1.0, T_c is 0 K since there is no chain of oxygen atoms.
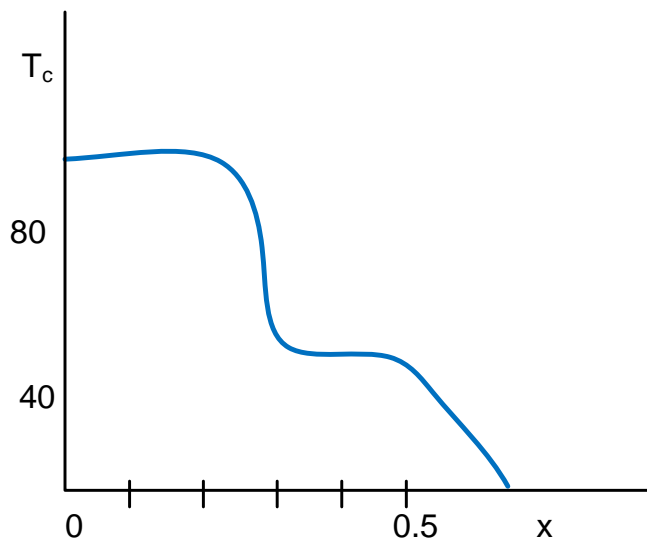
Figure 3. 6 Variation of critical temperature with x of $YBa_2Cu_3O_{7-x}$ with oxygen stoichiometry.[27]

3.3 Superconductivity in YBCO

3.3.1 Charge Carriers in YBCO

As described in section 3.1, Copper Oxide planes play a paramount role in superconductivity since charges are exchanged to and from the Copper Oxide layers. All cuprate superconductors can be described by the general compositional formula:

$$(AO)_m \, (Bo)_2 \, (M)_{n-1} \, (CuO_2)_n$$
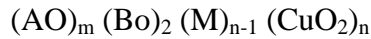
Figure 3.7 shows the structure of cuprate HTSCs can be classified as:

- Conduction layers (CuO_2),
- Charge reservoir layers.
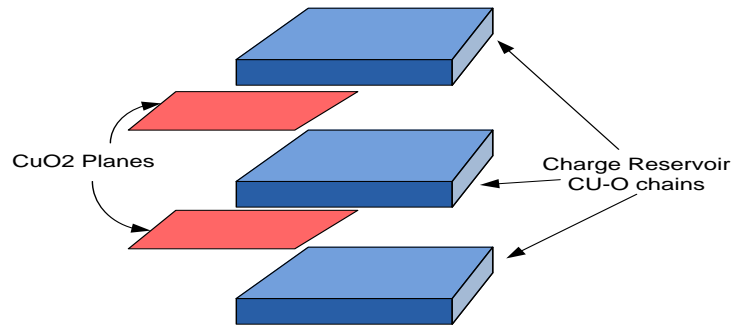
Figure 3. 7 Cu-O chains act as charge reservoir and CUO_2 planes act as conduction layers in YBCO.

Hole carriers come to existence in conduction layers when electrons are transferred to the charge reservoir layers. All cuprate superconducting compounds have a fraction of $0.05 - 0.3$ of mobile holes per CuO_2 unit cell in the ab planes.

Charge carriers are added by doping mechanism, like by adding oxygen to $YBa_2Cu_3O_6$, entering the compound as O_2^- and formingCuO chains. Such that a balance is maintained, electrons are removed from the copper oxide planes. Below T_c, the resulting holes are mobile and they form "Cooper pairs".

3.3.2 Anisotropy

YBCO is anisotropic in nature, meaning that its properties vary with respect to different crystallographic orientation. In general, HTSs are known to be inhomogeneous superconductors with superconductivity mainly associated to CU-O ab planes. The Cu-O planes are the main factors which accounts for the domination of anisotropy of normal and superconducting properties of HTSs. A crystal of YBCO has a larger coherence length in the ab plane than along the c-axis. Hence, the critical current is much bigger in the ab plane than along the c-axis as shown in Table 3.1. The energy gap also varies according to the crystallographic planes or directions. The energy gap is greater along the b directions and it is zero between the two axes.

Table 3.1 shows the superconducting characteristics of YBCO [27] and it can clearly deduce that the material is highly anisotropic from the crystallographic dependence of the superconducting parameters.

Table 3. 1 Anisotropic Properties of YBCO [27]

Parameter	*Parallel to c-axis*	*Parallel to ab-plane*
$\xi(\mathring{A})$	2 to 3	15 to 20
$\lambda(\mathring{A})$	1500	7500
J_c (A/cm^2 at 77 K)	10^4	10^6
H_{c2}(at 77 K)	150T	30T

Due to the anisotropic nature of YBCO, the penetration depth is eventually not constant in all directions. So, an average penetration depth λ_{av} needs to be considered. It is in fact the average of the penetration depth in the ab plane λ_{ab} and the c-axis λ_c .

3.3.3 Magnetic Properties of YBCO and HTS in general

Type-I superconductors are mostly elemental and type-II are compounds such as cuprate compounds. The initial distinction between type-I and type-II superconductors derived from the behavioural study of superconductors subjected to a magnetic field. Superconducting YBCO, which is a type-II superconductor, as the other cuprate superconductors, has a higher critical magnetic field than conventional superconductors (type-I). Two critical limits can be reached H_{c1} and H_{c2}. According to Abrikosov analysis of the G-L theory, YBCO has a surface energy $\sigma_s < 0$ (so do other cuprate superconductors) when it is placed in a magnetic field as discussed in section 2.28 [14]. The G-L parameter $k > \frac{1}{\sqrt{2}}$, is given by:

$$k = \frac{\lambda}{\xi_{GL}} \tag{3.1}$$

Where ξ_{GL} is the Ginzburg-Landau coherence length.

Figure 3.8 shows the magnetisation response for type-I and type-II superconductors with the applied magnetic field. As shown in Figure 3.9, below H_{c1}, YBCO exhibits perfect diamagnetism of the Meissner effect. Conversely to a perfect superconductor, YBCO is a flux expeller below H_{c1}. However, as H_{c1} is exceeded, the material enters into the mixed state and it splits into normal and superconducting domains since, this is energetically favourable.
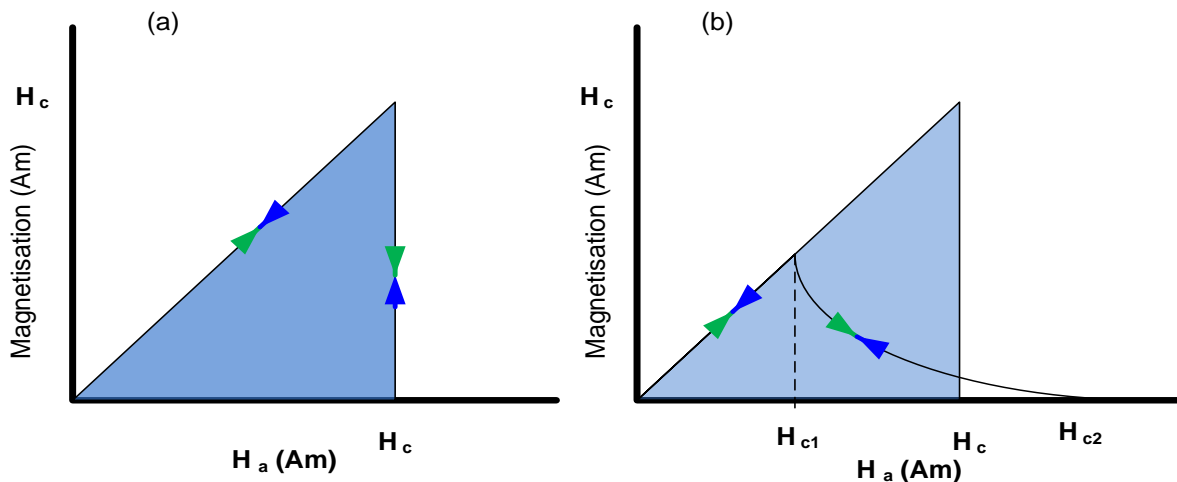
Figure 3. 8 Reversible magnetisation curves for (a) Type-I (b) Type-II superconductors
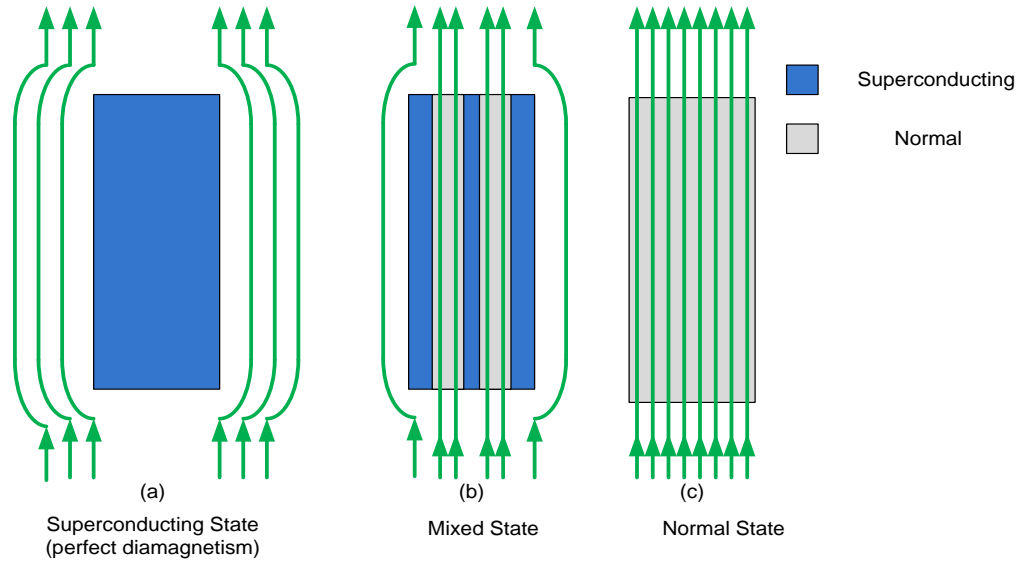
Figure 3. 9 Field profile of a superconductor: (a) Meissner state (b) Mixed state type-II (c) normal state for either type-I or type-II.

3.3.4 Critical Current of HTS (YBCO)

The critical current density is the maximum lossless value of current density above which the superconductor reverts into a normal material (undergoes resistive losses). Two types of current contribute to the critical current density: the transport current and the screening current. Transport current, is the current which flows on the surface of a superconducting specimen, transporting current in and out of a wire. J_i is the current density due to the transport current whereas the screening current, is the current that occurs due to the subjection of a superconductor to a magnetic field, shielding the interior of the material from the magnetic field. J_h is the current density due to the screening current.

$$J_t = J_i + J_h. \tag{3.2}$$

Where, J_t is the total current density.

If J_t exceeds the critical current density, superconductivity breaks. So, the Cooper pairs are imparted as the energy is greater than the binding energy of the pairs ($> \Delta_o$).

Sufficiently big current at the surface of the superconductor can lead to a value exceeding the critical current and the associated critical magnetic field. The critical magnetic field is associated with a critical current density, J_c. So, it can be concluded that the stronger is the applied magnetic field, the smaller will be the value of the critical current. When no magnetic field is applied, the only magnetic field generated is due to the transport current.

Consider a circular superconductor carrying a current. The current seems to flow in a dimensionless line down the middle of the conductor. At a distance x m away from a line current, according to Ampere's law, there is a magnetic field of strength:

$$H = \frac{I}{2\pi r}. \tag{3.3}$$

According to Silsbee's hypothesis [28],

$$I_c = H_c 2\pi x, \tag{3.4}$$

$$J_c = \frac{I_c}{2\pi r \lambda} = J_d, \tag{3.5}$$

Where:

r: radius of superconductor (*x* >> λ)

I: current,

I_c: critical current,

J_c: critical current density,

λ : penetration depth,

J_d : the depairing current density.

The depairing current for YBCO single crystal is very high. However, the critical current decreases significantly for YBCO samples which are granular in nature. The granular nature of YBCO limits the potential of the material for real life application. Complete depairing causes the material to change to normal when the critical current/critical field is exceeded. Before the critical field is reached, the material enters into a mixed state at H_{c1}. Mixed state means that, the HTS will have normal and superconducting domains. The material contains magnetic vortex lines, threading through the bulk in the form of triangular lattice known as flux line lattice (FLL). A vortex consists of a normal core, in which the magnetic field is large and is surrounded by a

superconducting region, in which a continuous supercurrent flows maintaining the magnetic field within the core of the material. Abrikosov predicted a square array of vortices [14] which was proved to be in fact triangular in nature due to the lower free energy of a triangular array of vortices. In the centres of the vortices, the order parameter is zero and the energy gap is inexistent leading to a loss in perfect conductivity. If transport current flows at the surface of the material, and is perpendicular to the magnetic vortices, Lorentz force will act on the vortices. The vortices eventually move in response to the Lorentz force resulting in power dissipation. This gives rise to resistance in the sample known as flux-flow resistance, which impedes on the current carrying capacity of HTS material.

In practice, YBCO and other HTSs are usually doped to induce pinning centres which will restrain the freedom of motion of the vortices and hence, improve the current carrying capacity of the material. For instance, in superconducting magnet, pinning centres are deliberately inserted to reduce joule losses due to interaction between flux vortices and high transport current.

Each Vortex carries a magnetic flux quantum of:

$$\Phi = \frac{h}{2e}$$ (3.6)

Where;

h is the Planck constant $(6.62 \times 10^{-34} m^2 \, kg \, / \, s)$

 e is the electronic charge of an electron $(1.6 \; x \; 10^{-19} C)$.

3.4 Polycrystalline Nature of HTS

HTSs are polycrystalline superconductors, meaning that the material lattice is composed of grains and grain boundaries, GBs. Polycrystalline materials have critical currents which are negatively affected due to the granular nature of type-II superconductors [29] [30]. The stress/strain field at the grain boundaries contribute to the weak link effect and hence the deterioration of the critical current at the grain boundaries [29] [30]. The granular nature of HTSs, YBCO and BSCO for instance, affects the current carrying capacity of the material [31].

The critical current density is sensitive to the grain orientation angles. The critical current density deteriorates for increasing misorientation angle θ [32] [33]. The presence of impurities such as hydrogen at GBs has been reported to impede on superconductivity of HTSs such as in YBCO, by disconnecting the weak links [34]. Bigger atoms such as Calcium has been reported to expand the dislocation cores at grain boundaries and hence relieving stresses at grain boundaries and provide additional charge carriers, thereby strengthening the grains' connections [35] [36] and improving the critical current density. Grains in polycrystalline materials do not have the same orientation. This gives rise to grain boundaries as interfaces between the grains. HTSs have short range coherence length, ξ, to which the critical current is sensitive. The consequence of this short coherence length is that the grain boundaries act as weak links [37]. The grain boundaries act as weak links Josephson junctions where quantum tunnelling takes place. In granular superconductors, both the intergranular and the intragranular critical current contribute to the critical current density of the superconductors. The intragranular current is controlled by the pinning centres in the polycrystalline lattice, while the intergranular critical current is a measure of the ability of the current to flow from one grain to an adjacent grain. The maximum value of the intergranular current reached provides an indication about the strength of the weak links. The higher the maximum intergranular current, the better are the grains' connections.
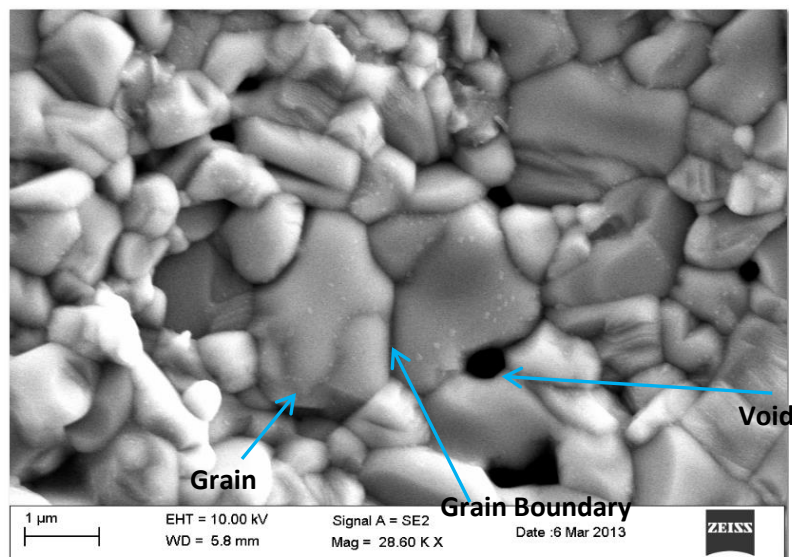
Figure 3. 10 SEM picture of polycrystalline YBCO which was sintered in the material science lab.

Figure 3.10 shows an SEM picture of a bulk polycrystalline YBCO specimen sintered in the material science lab. Clearly, the grains and grain boundaries can be distinguished. Many models have been proposed to study the way in which current tunnels from grain to grain in an anisotropic superconducting oxide lattice [37]. These models confirmed that the proportion of intergranular links is maximised by grain alignment. So, to improve the superconducting properties of granular an HTS, the latter is textured so that the c-axis of the crystal is close to being in a direction normal to the direction of flow of the transport current, and that the ab planes are almost parallel to each other. The process of texturing reduces the misorientation angle, leading to an increase in the value of the critical current density [38].

The focus of this research work was to design and implement an AC susceptometer to study the grain boundary behaviour of hydrogen-doped granular YBCO specimens. It is important to point out that the superconducting wavefunction (order parameter) is suppressed due to an increase in the stress field at the dislocations in the grain boundaries and this enhances the weak link effects at grain boundaries (acting as Josephson weak links) [30] [39] [40]. To understand the phenomena of stresses and dislocations in GBs and its associated problems, relevant material science theories were studied to be able to address the weak links problems discussed above. Hydrogen as dopant was used as H_2 molecules readily diffused to the grain boundaries where they could alleviate some stresses at the grain boundaries, even though it is known that the hydrogen impedes on superconductivity [6] [34]. The experimental procedures about hydrogen doping are detailed in Chapter 6. The next section is dedicated to dislocations and stresses at grain boundaries.

3.5 Dislocations

Dislocations are linear defects present in material's lattice as illustrated in Figure 3.11. They are defined as a distortion in the interatomic bonds causing a deviation from the ideal lattice pattern. The presence of dislocations in the material lattice is paramount for the formation of *Cottrell atmosphere* (to be discussed in the next section).
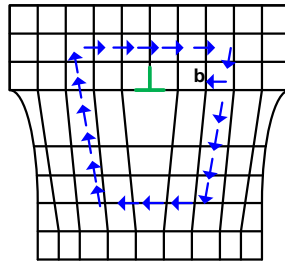
Figure 3. 11 Dislocation in a material lattice.

Dislocations are characterised by the *Burger vector*, **b**. The latter gives a description of the size and direction of the dislocation. The burger vector is found by making a circuit in the material's lattice from atom to atom. For a misaligned lattice with a dislocation, the circuit will not close. The vector closing the circuit gives the burger vector.

Dislocations can be classified as follows:

- Edge dislocations
- Screw dislocations
- Mixed dislocations

Edge dislocations have Burger vector, b, and perpendicular to the dislocation line.

Screw dislocations are parallel to the direction of the crystallographic plane.

Mixed dislocations are a blend of edge and screw dislocations.

Dislocations normally propagate into the materials' lattice and they get pinned at the grain boundaries, resulting into grain boundary strengthening as it requires more energy for the dislocations to shift directions and move to adjacent grain. So, dislocations cause

hardening/strengthening of materials [41] which is often a desired mechanical property of materials such as in metals.

In situations where stresses are applied to the material, the dislocations propagate into the crystalline lattice until a grain boundary is encountered, at which a large repulsive stress is experienced by the moving dislocation due to atomic mismatch. Consequently, the dislocations piled up at the grain boundaries due to their inability to move across the mismatched regions. Evidently, the dislocations exert accumulated repulsive force at the mismatch regions. As a result, grain boundaries are high stress/strain field regions in the crystal lattice. Despite the fact that the presence of grain boundaries and dislocations can be beneficial in some situations such as in metal hardening, the existence of grain boundaries and dislocations have a detrimental effect on HTS. For instance, strain fields around grain boundary dislocations in $YBa_2Cu_3O_{7-x}$ thin films substantially suppress the local critical current density J_c[29]. Dislocations are mainly present at grain boundaries GB.

An edge dislocation is considered for analysis. At the dislocation, there is a stress field as shown in Figure 3.12 .
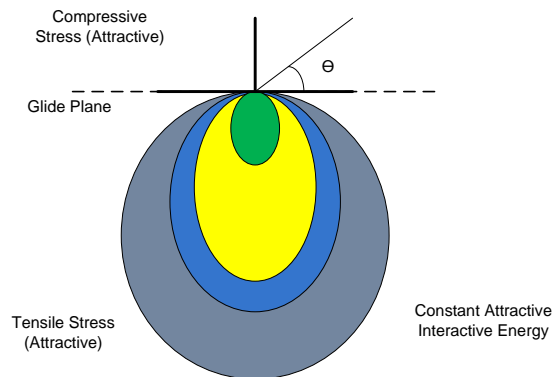
Figure 3. 12 Stress field due to an edge dislocation.

Stresses act in all directions (x y z) and their combination leads to a parameter known as the hydrostatic pressure at a vector element of the material, due to displacement of a point in a strained body. Equation 3.7 is used to calculate the hydrostatic pressure P_{ii}, which is an important parameter in the analysis of the formation of Cottrell atmosphere. Equation 3.7 relates P_{ii} to the above mentioned stresses.

$$P_{ii} = - \ \frac{1}{3} \ (\sigma_{xx} + \sigma_{yy} + \sigma_{zz}) \qquad (3.7)$$

Where σ_{xx} , σ_{yy} and σ_{zz} are the stresses in the x-direction, y-direction and z-direction respectively

3.6 The Cottrell Atmosphere

The Cottrell Atmosphere is defined as the segregation of solute atoms near dislocations, relieving the stresses around dislocations, to form an equilibrium atmosphere. Large atoms are gathered in the dilated part, whereas small ones accumulate in the compressed part. This concept was put forward by Cottrell and Bilby in 1948 [42]. In fact, Cottrell along with Bilby published a paper in 1948, describing the yield and strain ageing of iron by considering the 'condensation' of the atmosphere on dislocations.
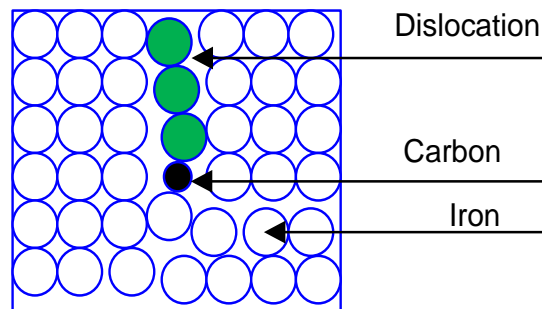
Figure 3.13 Cottrell atmosphere due to carbon interstitial.

In that same paper, Cottrell and Bilby pointed out that the stress field around the edge dislocation can be relieved by interacting carbon atoms. Figure 3.13 shows a typical Cottrell atmosphere, due to a carbon atom near a dislocation core. In an elastic isotropic medium, the solute atoms hardly interact with a shear stress field but only with hydrostatic pressure [42]. Consequently, atoms hardly interact with screw dislocations. Thus, only edge dislocations will be considered for the investigation of the formation of Cottrell atmosphere.

When interstitials get into a crystal lattice, they will distort the lattice slightly and there will be associated residual stress field surrounding the interstitials. This stress field at the dislocations can be relaxed by the interstitials or substitutional solutes, diffusing towards the dislocations containing a small gap as shown in Figure 3.13. So, the formation of Cottrell atmosphere is expected to relieve the stress field along dislocation line, which are prone to occur in grain boundaries, with the expected result of improving the critical current.

The stress field created by the dislocation is in fact the driving force for the segregation of the solute atoms. Consequently, this leads to the segregation of solute atoms along the dislocation lines and the formation of relatively high concentration solute atoms regions known as the *Cottrell atmosphere*.

The first calculations of the interaction between solute atoms and dislocations are due to Cottrell (1948) who calculated the potential $V(R, \theta)$ (polar coordinate) of a solute atom in the hydrostatic stress (Equation 3.7) field of an edge dislocation and obtains :

$$V(R, \theta) = \frac{4}{3}[(\mu \varepsilon r^3 \lambda)/R]\frac{(1+v)}{(1-v)}\sin\theta, \tag{3.8}$$

Where μ is the shear modulus, $\varepsilon = \Delta V/V$ (i.e. the lattice dilation due to a substitutional atom), λ is the slip distance, v is the poisson's ratio of the material and r is the radius of the solute atom. Substituting $\theta = \pi/2$, $v = 1/3$ and $\lambda = r = \boldsymbol{b_0}$ (Burger vector) into Equation 3.8 gives:

$$V(R, \theta = \pi/2) = \frac{8}{3}[(\mu \varepsilon b_0{}^4)/R] \tag{3.9}$$

However, the inclusion can be of interstitial nature and a general form for the interaction energy is:

$$V(R, \theta) = \frac{1}{3}P_{ii}\Delta v \tag{3.10}$$

Where P_{ii} is the hydrostatic pressure (Equation 3.11) associated with the edge dislocation, Δv is the change in volume (calculated from Equation 3.12) that occurs when an interstitial atom gets into an interstitial site in the lattice.

$$P_{ii} = \frac{1}{3}\left(\sigma_{xx} + \sigma_{yy} + \sigma_{zz}\right) \tag{3.11}$$

$$\Delta v = \frac{4}{3}r^3\pi\,[(1+\delta)-1] \approx \frac{4}{3}r^3\pi 3\delta \tag{3.12}$$

Where $(1+\delta)r$ and r are the radii of the solute atom and that of the spherical hole (interstitial site) respectively.

The conditions required for the formation of Cottrell atmosphere are:

(i)   an adequate concentration of solute , i.e. the number of available solute atoms per dislocation per atomic plane is given by [42] :

$$n = \frac{1}{\varrho} \tag{3.13}$$

Where, ϱ is the dislocation density.

(ii)   a sufficient time. This will depend on the diffusion coefficient and therefore on the temperature.

(iii) $V \leq K_B\,T$. Equating $V(r, \theta = \pi/2)$ to $K_B\,T$ gives the effective size of R_o of the Cottrell atmosphere. Where K_B is the Boltzmann constant and T is the temperature in Kelvin.

3.6.1 Elastic Approximation

The key parameter for the formation of the Cottrell atmosphere is the interaction energy of the solute atoms in the stress field near a dislocation line. The equations in section 3.6 are based on the elastic isotropic theory. They are mostly based on the work of A.H Cottrell. Douthwaite and Evans repeated the calculation of A.H Cottrell using anisotropic elastic model to obtain the stress field [43]. Between an isotropic and an anisotropic material, only the value of the hydrostatic pressure will differ but the approach to calculate the other parameters such as interaction energy and rate of ageing stays the same. E. Clouet *and al* calculated the interaction energy using both isotropic and anisotropic models, which obey qualitatively with experimental and simulation results [44]. Moreover, Equation 3.8 is approximately true for the case of an anisotropic medium, since spatial variation of the hydrostatic pressure over such small volume of the point defect can hardly be significant [45].

3.6.2 Summary

In this chapter, the relationship between the granular nature of YBCO, dislocation and critical current density was elaborated. The alleviation of stresses in YBCO material's lattice, should lead to an improvement in the average critical current density. It was proposed that hydrogen may act as interstitial dopant of YBCO and as such, relieve stress at dislocations in forming Cottrell atmospheres and also increase critical currents in the grain boundaries.

Chapter 4 AC Susceptibility

4.1 Introduction

Since the discovery of high temperature superconductors in 1986 [16], the measurement of AC susceptibility has been recognised to extract certain superconducting properties. It is an inductive method which senses the magnetic response from an entire volume of a superconducting specimen [46]. In brief, the susceptometer is made up of a primary coil connected to an AC source and two similar, oppositely wound pickup coils, connected in series, which are positioned within the primary coil. The specimen is inserted into one of the secondary coils. Figure 4.1 shows a typical arrangement of a primary and secondary coils which compose an AC susceptometer. The material's response, measured by the pickup coil, is fed to a lock-in amplifier which acts as a discriminating voltmeter. The latter measures the in-phase (real) and the out-of-phase (imaginary) AC susceptibility components of the material. Most of the suceptometer designs reported make use of one primary coil and two secondary coils. Moreover, the secondary coils are made up of at most two layers of coils with the number of turns not exceeding one thousand [46] [47] [48]. A large number of turns at the secondary coil eventually produce a good signal-to-noise ratio at the secondary coil [49]. AC susceptibility is a very appealing measurement technique since it is contactless and is a very powerful characterisation tool to study superconducting materials [4]. Superconducting parameters such as J_c, T_c and λ can be obtained [2]. The complex AC susceptibility can be deduced from the penetration depth and the width of the specimen using an expression derived by *Kes et al* [50]. During the transition from normal to superconducting phase, the interaction of screening current and penetrating sweeping AC magnetic field will cause the dissipation of energy. Thus, the heat generated due to oscillating magnetic field can also be deduced from AC susceptibility measurement [51]. For high temperature superconductors, this method has been particularly

useful to study the dynamics of flux vortices and phase transition in the vortex state [46] [52] [53]. In certain situations, only the relative susceptibilities were enough to characterise a sample [54]. So, there was no need in calibrating the susceptometer, to cater for the demagnetisation factor, since the logging of the relative susceptibility with temperature was enough to deduce the T_c of a particular YBCO sample. However, for very accurate susceptibility measurements, the susceptometer should be calibrated and the demagnetising factor, based on the shape of the sample, has to be taken into consideration. For calibration purposes, it has been reported that a coil having the same shape as the specimen to be characterised was used to mimic the sample [3]. Hence, for correct measurements, the values of AC susceptibility measured should be corrected for demagnetisation based on the shape of the sample. For instance, for ellipsoid specimen, the formula derived by Osborn J.A can be applied to estimate the demagnetisation factor [55]. Correcting for the demagnetisation effect is capital if a sensitive parameter, such as the magnetic energy stored in the space occupied by a superconducting sample, is to be calculated from accurate measurements of complex AC susceptibility [56]. However, determining physical quantities such as H_c , J_c, T_c, etc., would have been impossible without a good cooling system to effectively cool the sample placed in an AC field. There exist several ways of cooling a superconductor in an oscillating magnetic field for AC susceptibility measurements. The use of a closed cycle liquid helium cryostat has been reported [54] [57]. The helium based cryostat can be an open-loop cryostat as well, with the secondary coils attached to quartz tubing and the entire system is cooled by a liquid helium exchanger (open-loop system) and a heater is used in conjunction with a temperature controller for temperature regulation [46].
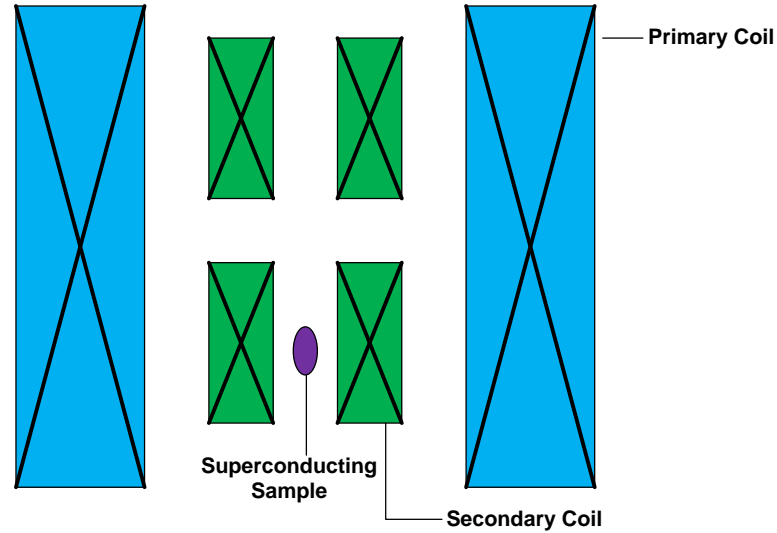
Figure 4. 1 Typical AC susceptibility set up, showing the primary coil and the secondary coils.

4.2 Magnetic Susceptibility

The magnetisation, M of a magnetic material is described as the magnetic dipole moment per unit volume . The S.I unit of magnetic dipole moment is $A.m^2$ and thus, the S.I unit of magnetisation is A/m. A possible magnetisation model of a bulk material specimen is the occurrence of abundant number of atomic current loops in the material's interior. On the material's surface, microscopic current loops circulate and this result in a surface current density (current per unit length) M×**n** where **n** is the surface normal vector. For a constant axial magnetisation M throughout a cylindrical sample, the magnetisation is $M = nI$ $(B = \mu_o nI \ for \ a \ solenoid)$ since the current circulates round the material and is analogous to a current circulating around a solenoid.

$n: Number \ of \ coils \ per \ unit \ length.$

For magnetisation throughout a long cylindrically-shaped specimen, it is equal to M**:**

$$M = nI. \tag{4.1}$$

The B field (Magnetic flux density) inside the material can be written as:

51

$$B_{in} = \mu_o M. \tag{4.2}$$

The magnetic field outside the material is zero, i.e.

$$B_{out} = 0. \tag{4.3}$$

If the sample is placed in an axial magnetic field, B_a (field parallel to the axis of the sample), such that the magnetic field $B_a = \mu_o H_a$. On application of a magnetic field to a sample, the net magnetic field B_{net} is:

$$B_{net} = B_a + B_{in,} \tag{4.4}$$

$$B_{net} = \mu_o(H_a + M), \tag{4.5}$$

$$M = \chi H_a, \tag{4.6}$$

Hence, the magnetisation is proportional to the applied H-field, H_a (magnetic intensity) and Equation 4.7 define magnetic susceptibility of a material, χ. Susceptibility of a material can thus be defined as a measure of a sample's magnetisation in response to an applied magnetic field [46].

For a sample in its superconducting state, $\chi < 0$ and this characterises the diamagnetic nature of a superconductor. For a fully superconducting specimen, χ = -1. When $\chi > 0$, the magnetic response is known as paramagnetic.

$$\chi = \frac{dM}{dH_a} . \tag{4.7}$$

Consider a superconducting specimen subjected to an oscillating magnetic field, varying sinusoidally along the sample's axis:

$$H = H_0 \cos\omega t. \tag{4.8}$$

Where, ω ($2\pi f$) is the angular frequency of the signal.

The material responds to the applied AC magnetic field, resulting in a distorted B- field with some phase lag with respect to the H-field, which cannot be expressed by a pure sinusoidal

wave. Since the response is periodic, the resulting B field can be expressed by a fourier expansion:

$$B = \mu_o H_o \sum_{n=1}^{\infty} [\mu_n' \cos(n\omega t) + \mu_n'' \sin(n\omega t)]. \tag{4.9}$$

μ_n' and μ_n'' are the real and imaginary permeability of the nth harmonics respectively. The relationship between permeability and susceptibility is given by:

$$\mu_n = 1 + \chi_n, \tag{4.10}$$

$$\mu_n = \mu_n' + j\mu_n'', \tag{4.11}$$

$$\chi_n = \chi_n' + j\chi_n'', \tag{4.12}$$

and

$$\chi_n' + j\chi_n'' + 1 = \mu_n' + j\mu_n'', \tag{4.13}$$

[46].

Comparing real and imaginary:

$$\mu_n' = 1 + \chi_n', \tag{4.14}$$

$$\mu_n'' = \chi_n''. \tag{4.15}$$

Now, both sides of Equation 4.9 ($n = 1$) is multiplied by $cos(\omega t)$ and integrate from 0 to $2\pi/\omega$ (one period) :

$$\int_0^{2\pi/w} [B \cos \omega t] dt = \mu_a H_o \left(\frac{\pi}{\omega}\right) \mu_1'. \tag{4.16}$$

Both sides of Equation 4.9 ($n = 1$) is then multiplied by $sin(\omega t)$ and integrates within the same limit:

$$\int_0^{2\pi/w} [B \sin(\omega t)] dt = \mu_o H_o \left(\frac{\pi}{\omega}\right) \mu_1''. \tag{4.17}$$

Combining Equations 4.14 to 4.16 and considering the first harmonic:

$$\chi_1' = \frac{\omega}{\pi \mu_o H_o} \int_0^{2\pi/\omega} [B \cos \omega t] \, dt - 1 .$$ (4.18)

Combining equations 4.15 to 4.17 and considering the first harmonic:

$$\chi_1'' = \frac{w}{\pi \mu_o H_o} \int_0^{2\pi/\omega} [B \sin (\omega t)] dt.$$ (4.19)

For a specimen in the superconducting state, $\chi_1' < 0$, for complete Meissner expulsion, $\chi_1' = -1$, and for full flux penetration, the integral is 1 and thus the value of $\chi_1' = 0$. In the superconducting state χ_1'' carries a small positive value, that reflects AC losses in the superconducting specimen [2] [46].

Consider a primary solenoid whose length $l \gg R$, where R is the radius of the solenoid.

The self-induced flux through the solenoid is:

$$\Phi_s = NAB.$$ (4.20)

Where, N is the total number of turns, B is the magnetic flux density in Tesla and A is the area of cross-section of the solenoid (πR^2).

$$\Phi_s = LI_s.$$ (4.21)

L is the self-inductance ;

$$L = \frac{\mu_o N^2 A}{l}.$$ (4.22)

I_s is the current flowing through the solenoid.

Applying Faraday's law of electromagnetic induction, the induced e.m.f in the pickup coil due to the primary coil:

$$V = -\frac{d\Phi}{dt},$$ (4.23)

$$V = -L \frac{dI_s}{dt},$$ (4.24)

The magnetisation is given by:

$$M = \frac{NI_s}{l},$$ (4.25)

Therefore;

$$V = -l \frac{L}{N} \frac{dM}{dt} . \tag{4.26}$$

The oscillating magnetic field is:

$$H = H_0 \cos(2\pi f)t. \tag{4.27}$$

Considering only the first harmonic:

$$M = \chi_1 H, \tag{4.28}$$

$$M = \chi_1 H_0 \cos(2\pi f)t, \tag{4.29}$$

$$V_{rms} = \frac{LlH_o 2\pi f \chi_1}{N\sqrt{2}}, \tag{4.30}$$

$$V_{rms} = \frac{LlH_{rms} 2\pi f \chi_1}{N}, \tag{4.31}$$

In practice, the value of L is not computed but a calibration constant α' is rather calculated, which reflects the secondary coil's geometry (α' is calculated in Chapter 5)

The susceptometer is composed of a primary coil and two N_s turns secondary coils, of cross section radius r each, are positioned symmetrically inside the primary solenoid. Moreover, the two secondary coils are oppositely wounded and connected in series opposition. The superconducting specimen is placed into one of the secondary coils as shown in Figure 4.1.

The total magnetic flux Φ induced will be due to the two secondary coils placed into an oscillating magnetic field (given by Equation 4.27) and the magnetisation M due to the superconducting sample.

$$\Phi = \mu_o \pi r^2 N_s \left[(M + H) - H \right] . \tag{4.32}$$

$(M + H)$ is the total magnetisation at the secondary coil holding the superconducting sample, whereas H is the total magnetisation at the empty secondary coil.

Therefore, the total magnetic flux through the N_s turns oppositely wound secondary coils is:

$$\Phi = \mu_o \pi r^2 N_s M(t) \ . \tag{4.33}$$

Applying Faraday's law of electromagnetic induction:

$$V(t) = -\mu_o \pi r^2 N_s \frac{dM}{dt}, \tag{4.34}$$

$$M(t) = H_o \sum_{n=1}^{\infty} [\chi_n^{'} \cos(n\omega t) + \chi_n^{''} \sin(n\omega t)] \ , \tag{4.35}$$

$$V(t) = \mu_o \pi r^2 \omega N_s H_o \sum_{n=1}^{\infty} [\chi_n^{'} \sin(n\omega t) - \chi_n^{''} \cos(n\omega t)] \ , \tag{4.36}$$

$$V_o = \mu_o \pi r^2 \omega N_s H_o, \tag{4.37}$$

$$V_1(t) = V_o [\chi_1^{'} \sin(\omega t) - \chi_1^{''} \cos(\omega t)]. \tag{4.38}$$

Equation 4.38 gives the first harmonic of the voltage induced at the pickup coils. Two components constitute the induced voltage: the in-phase and the out-of-phase voltage components. A lock-in amplifier which acts as a discriminating voltmeter was used to measure each voltage component independently. The real and imaginary components of the AC susceptibility can be deduced from the voltages locked by the AC susceptometer.

4.3 Superconducting Parameters Determined from AC Susceptibility

From the in-phase and the out-of-phase components measured by the lock-in amplifier, the real and the imaginary AC susceptibilities can be determined. Susceptibility measurements, with respect to physical quantities such as temperature and magnetic field, have the potential to reveal important information about a superconducting specimen as stated in Chapter 1. The following details how AC susceptibility can be used to characterise a superconducting specimen to determine its superconducting parameters.

4.3.1 Energy Converted

The physical interpretation of the imaginary susceptibility $\chi^{''}$is the energy, W_q, converted into heat energy after one cycle of the AC field [51] due to magnetic field penetrating the sample .

Only positive values of $\chi^{''}$ exist since they are physically possible. If the time average of the power dissipated is defined by Equation 4.39, only positive W_q is energetically possible. So, if the AC susceptibility measurement is carried out correctly for a superconducting sample, the values of $\chi^{''}$ should be positive. Equation 4.39 gives the energy which is converted into heat energy during one cycle of the AC field.

$$W_q = -2\pi\frac{\chi^{''}B_a^2}{2\mu_o}.\qquad\qquad(4.39)$$

The real AC susceptibility is interpreted as the magnetic energy stored in the volume occupied by the sample [56]. The magnetic energy stored is:

$$W_m = \frac{\chi^{'}B_a^2}{2\mu_o}.\qquad\qquad(4.40)$$

4.3.2 Critical Temperature and AC Susceptibility

AC susceptibility measurements have been extensively used to determine the critical temperature of superconductors [2][3][46][54]. A superconductor subjected to AC susceptibility measurements will allow the magnetic field to penetrate through it in normal condition. However, the magnetic field is instantaneously shielded when the superconductor goes from normal to superconducting phase due to the setting up of a screening current that accounts for the diamagnetic response of the superconducting sample. Consequently, a sharp increase in the real susceptibility occurs as the material goes superconducting. The logging of the real susceptibility with respect to temperature is a very common and effective practice in determining the critical temperature of a superconductor. The logging of susceptibility (both real and imaginary) will be

discussed in more detail in Chapter 6 and the experimental results will be elaborated in Chapter 7.

When the sample is fully superconducting, under complete Meissner expulsion and below the critical temperature, the real susceptibility has reached its maximum value of -1. Usually, a magnetic field of the order of micro Tesla is applied for T_c characterisation [2][3][46][54].

4.3.3 Critical Current Density and AC Susceptibility

The granular characteristics of HTSs are responsible for the weak link effects leading to low critical current in bulk high temperature superconducting material. An AC susceptometer can be used effectively to measure the critical current density [58] [59] [60] [61]. The first and second peaks in $\chi^{''}$ and $\chi^{''}$, from $\chi^{''}$ against B graph, correspond to the intergranular and intragranular field penetration respectively [60] [61]. The intergranular current provides information about the grain couplings, whereas the intragranular current reveals the pinning capabilities of the specimen tested [61]. The simple critical state model, the Bean model, which treats the superconducting specimen only macroscopically, considers only two states: J_c and zero critical current. *"The simplest critical state of Bean"* [61] defines the following equation when the sample gets fully penetrated:

$$B_p = B^* = u_o J_c R \ .\tag{4.41}$$

The penetrating magnetic flux density $B_p = B^*$ when the sample is fully penetrated, R is the radius of a cylindrical superconducting sample and J_c is the critical current density. Figure 4.2 shows an ideal graph for $\chi^{''}$ against B for a superconducting specimen. This graph is adapted from the work of *D.X Chen et al* and *M.Ciszet et al* [60] [61].

Referring to Figure 4.2, the first peak in $\chi^{''}$ occurs at B_{pi}^*. The first peak is related to the magnetic flux which just reaches the centre of the sample. At B_{pi}^*, the AC field penetrates the grain fully (supercurrent reaches the centre of the superconducting sample). The intergranular critical current density can be estimated from:

$$B_{pi}^* = u_o J_{ci} \frac{D}{2} \; . \tag{4.42}$$

Where J_{ci} is the intergranular critical current density, and D is the width of the sample.

Knowing the value of B_{pi}^* , the value of the intergranular critical current, J_{ci} , can be estimated from Equation 4.42.

Similarly, knowing the value of B_{pg}^* , applied magnetic field at which the second peak in χ'' occurs, the intragranular critical current density, J_{cg}, can be estimated using the Equation 4.43[61].

$$B_{pg}^* = u_o J_{cg} \frac{D}{2} \; . \tag{4.43}$$

The second peak in χ'', which appears at B_{pg}^* , is associated with the granular losses in the form of Abriskosov types vortices for $B > B_{c1}$, the first critical magnetic flux density.
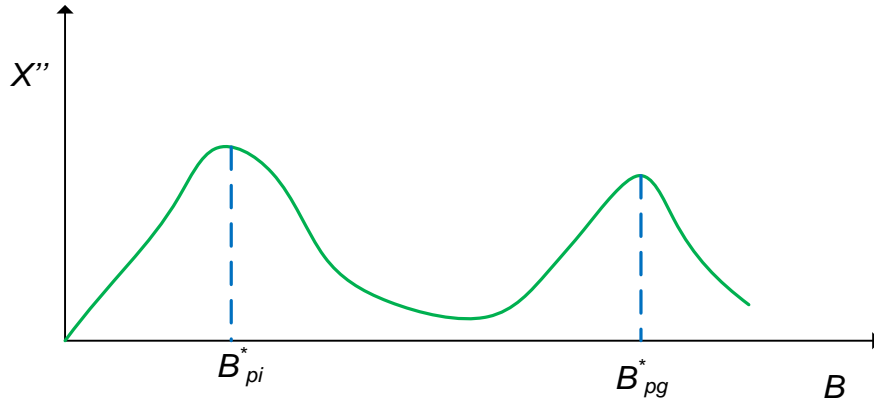
Figure 4. 2 Ideal graph of χ'' against B for a superconducting specimen at a constant temperature below T_c [60], [61].

4.3.4 Penetration Depth

For a superconducting slab of width $2R$ in a parallel magnetic field, the following expression for the complex susceptibility in terms of R and penetration depth δ was derived by *Kes et al,* [50]:

$$\chi' = \left[\frac{\delta}{2R}\right]\left[\frac{sinh\left(\frac{2R}{\delta}\right)-sin\left(\frac{2R}{\delta}\right)}{cosh\left(\frac{2R}{\delta}\right)+cos\left(\frac{2R}{\delta}\right)}\right] - 1, \tag{4.44}$$

$$\chi'' = \left[\frac{\delta}{2R}\right]\left[\frac{sinh\left(\frac{2R}{\delta}\right)+sin\left(\frac{2R}{\delta}\right)}{cosh\left(\frac{2R}{\delta}\right)+cos\left(\frac{2R}{\delta}\right)}\right] - 1. \tag{4.45}$$

R is the radius of a spherical superconducting sample.

Using the AC susceptometer, the values of the complex susceptibility can be measured. Using Equation 4.44 or Equation 4.45, the penetration depth can be estimated.

Chapter 5 AC Susceptometer Design

5.1 Introduction

Basically, a typical AC susceptometer comprises of a primary coil and two secondary coils connected in series and wound in opposite direction [2] [46]. The secondary coils are inserted inside the primary coil and they are subjected to a varying magnetic field from the primary coil, $H = H_o\, cos(\omega t)$. Ideally, without any sample at one of the secondary coil, the net voltage at the pickup coil should be equal to zero. However, in practice, this is difficult to achieve because the two secondary coils are not perfectly identical. While winding the secondary coils, much effort was put in decreasing the mismatch between them but still, perfectly identical coils are difficult to build. As a result, an offset voltage exists due to this mismatch when the pickup coils are empty.

For conventional AC susceptometer, the induced signals at the secondary coils are fed to an analogue lock-in amplifier (a dedicated apparatus), which acts as a discriminating voltmeter, capable of measuring the in-phase and the out-of-phase components from which the real and imaginary AC susceptibility components were deduced. The AC susceptometer designed and implemented for this research can be classified as a DSP-enhanced susceptometer because it made use of a digital-based lock-in-amplifier which was designed and implemented in a software environment.

In this chapter, the full design of the AC susceptometer is discussed

5.2 AC Susceptometer's System Requirements.

The scope of the research was to design and implement a DSP-enhanced AC susceptometer to characterise granular YBCO specimens, such that the intergranular connections can be assessed.

The DSP-enhanced AC susceptometer designed should satisfy the following requirements:

- the length of the primary coil should be less than 300.0 mm for it to be able to fit into the cryostat.
- the secondary coil needs to accommodate a slab-like superconducting sample whose linear dimensions do not exceed 20.0 mm x 4.0 mm x 2.0 mm.
- the current flowing through the primary should not produce excessive Joule heating which can damage the coil.
- the data-acquisition system is expected to detect signal of nanovolt resolution to ensure that the susceptometer can pick up the diamagnetic response of the YBCO specimens.
- the susceptometer design should cater for a flexible system with the possibility of varying the magnetic field in the range of 0 T to 30.0 mT.
- a sampling frequency of at least 100 KHz is required to execute high resolution measurements at different experimental signal's frequencies.
- the material used to make the coils should be of non-magnetic nature. Otherwise, the magnetic response of the coils' material will interfere with the diamagnetic response of the superconducting sample.
- the voltage offset at the secondary coils should be effectively reduced for accurate AC susceptibility measurement.
- a software-based lock-in amplifier implemented in a robust software environment for effective measurements of the magnetic response of the superconducting specimen.
- the software-based lock-in amplifier should be able to effectively filter the small diamagnetic signal (of the order of nanovolt) having a frequency of 50 Hz from a noisy environment.
- the real and the imaginary components of the diamagnetic signal should be extracted by the lock-in amplifier.

The ideal requirements for the AC suscepctometer were summarised above. However, experimental and design limitations were encountered, as the material science laboratory has restricted resources. Hence, as far as possible, the requirements were satisfied by making compromises while using the readily available laboratory equipment.

5.3 The Proposed AC Susceptometer

The AC susceptometer system consisted of one primary coil, two pickup coils, wound in series opposition, a lock-in amplifier implemented by the use of a DSP computer program. An analogue to digital converter interfaced the magnetic experimental signals to the computer for analysing.

The complete susceptometer system was constructed in the material science lab and in the mechanical workshop in the Electrical, Electronic and Computer Engineering department. The winding system was set-up to make the coils, using a small lathe equipped with an analogue turn's indicator. The speed of the lathe and distribution of the windings were controlled by hand. This technique enabled the accurate control of the number of turns.

Figure 5.1 shows a simplified version of the proposed AC susceptibility measurement system. The balancing of the signal at the pickup coils was achieved by using an electronic system. The sample was cooled to cryogenic temperatures for the AC susceptibility experiments. The susceptibility measurement system relies on inductive coupling to measure the material's susceptibility. The secondary coils were placed at the centre of the primary coil for maximum field coupling and undesired capacitive coupling was minimised by wrapping the secondary coils with cryogenic adhesive tape, which is compatible at low operational temperatures, as shielding reduces capacitive coupling. The presence of a superconducting specimen at one of the secondary coil disturbed the inductive coupling and thus a change in self-inductance occurred as well as a change in the magnetisation signal's phase (with respect to the applied field). At T_c and below, the diamagnetic response was detected by the secondary coils and fed to the computer, which processed the signal through a lock-in amplifier program to measure the complex AC susceptibility response with respect to temperature or magnetic field.

For T_c characterisation, the Lakeshore Model 336 temperature controller was used to control the temperature of the sample stage of the experiment by regulating a heater, using a closed loop PID algorithm. The sample was slowly cooling at 0.2 K per minute for T_c characterisation.
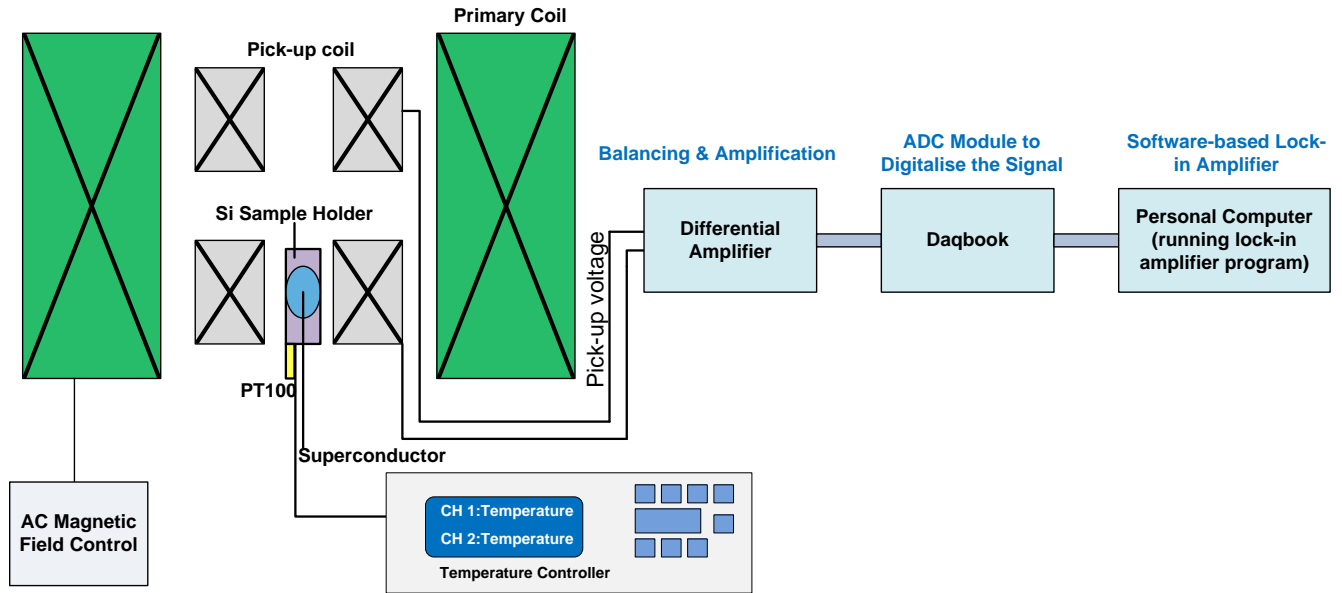
Figure 5. 1 Simplified diagram of the AC susceptometer system.

5.3.1 Design of the Primary Coil

Before designing the susceptometer, it was important to decide which type of sample would be used, whether it was a bulk sample or a thin film specimen. Furthermore, the dimensions of the sample to be used, had to be decided in order to size the coils correctly. For the scope of this research, the susceptometer should be able to accommodate a flat slab bulk samples with maximum linear dimensions of 20.0 mm x 4.0 mm x 2.0 mm. The design of the primary coil was done before considering other aspects of the AC susceptibility measurement device. Particular attention was given to the magnitude of the alternating magnetic field which is influenced by the coils' dimensions. For instance, if the field was close to the critical magnetic flux density of the YBCO specimen, it would affect the onset of superconductivity.

Furthermore, the dimensions of the wire should be sized with respect to the magnitude of the desired operating magnetic field, which is current dependent.

Equation 5.1 describes the magnetic flux density inside the primary coil as a function of the coil's dimension parameters, in the x plane,

$$B = \frac{\mu_o NI}{(4r^2+l^2)^{1/2}} \; \hat{x} \; .$$

(5.1)
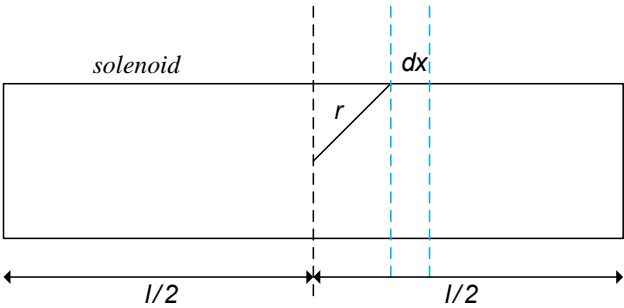
Figure 5. 2 Longitudinal cross-section of coil with strips of width dx.

Where,

B = flux density, T

μ_o = permeability of vacuum, H/m

I = current through solenoid, A

l = length of solenoid, m

r = radius of solenoid, m

N = number of turns

At the centre of a long solenoid, Equation 5.1 approximates to,

65

$$B = \frac{\mu_o NI}{l}, \qquad (5.2)$$

when $l \gg r$ but it is an acceptable approximation even though l is not much larger than r.

In practice, the length of the coil cannot be infinitely long to give a uniform field inside the coil. The sample was positioned at the centre of the coil where the field was more uniform, exposing the latter to the maximum magnetisation possible.

The impedance of the primary coil depends on the coil's resistance and self-inductance.

The coil's resistance was found using,

$$R = \frac{\rho l}{A'}, \qquad (5.3)$$

where R is the resistance of the coil, l its length, A' is the area of cross-section of the wire and ρ is the resistivity.

The coil's self-inductance was calculated from,

$$L = \frac{\mu_o N^2 A}{l}. \qquad (5.4)$$

A is the area of cross section of the coil.

To calculate the current flowing through the coil (voltage/impedance), its impedance Z should be known.

$$Z = \sqrt{R^2 + (\omega L)^2}, \qquad (5.5)$$

where, ω is the angular frequency.

Figure 5.3 shows the different plots of axial magnetic field inside the primary coil against the number of turns at different frequencies for a fixed supply voltage (5V).

From these plots, it could be deduced that in an attempt to increase the magnetic field, B, by increasing the number of turns, the self-inductance L was also increased even by a faster rate, resulting in a decrease in the coil's magnetic flux density B. This could obviously be an obstacle when a high magnetic field was required. To counteract this decrease in magnetic field (calculated using Equation 5.2), a power amplifier could have been used to supply a larger current. But a larger current would incur more power dissipation across the coil.

The current rating of the wire is proportional to the wire's diameter. AWG 23 wire, whose diameter is 0.57404 mm, was chosen. The AC current rating of the AWG 23 wire used for the primary coil is 729 mA (at room temperature and 53 KHz).
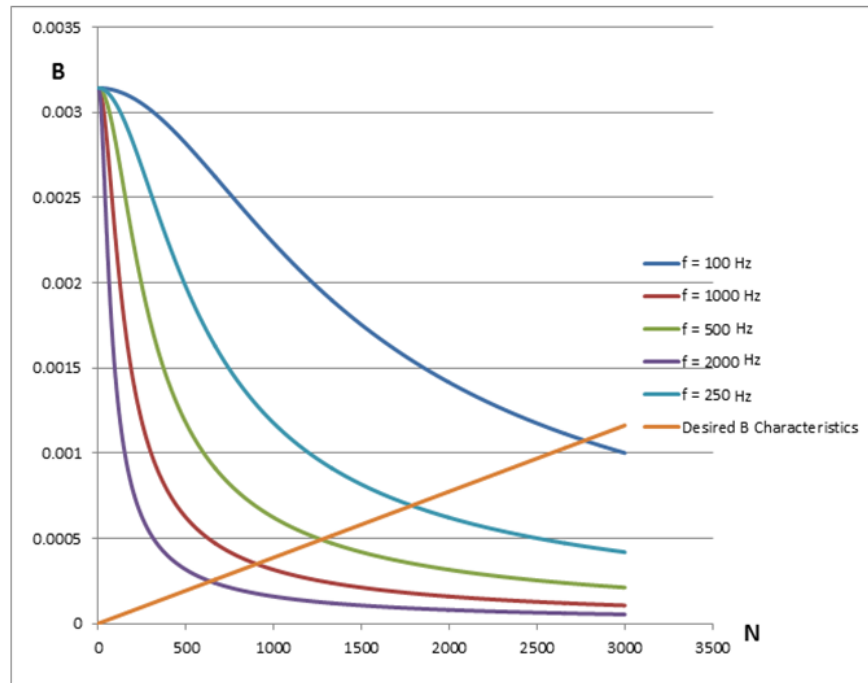
Figure 5. 3. Magnetic flux density B (in Tesla) vs. number of turns N at a constant input voltage of 5V.

The primary coil was meant to operate at currents which were well below the rated current (729 mA), so as not to put unnecessary electrical stress on the wire under room conditions. The desired characteristics for B (in orange) were drawn. The length of the primary coil and the maximum operating current (for T_c characterisation) are the constants, while B and N are the variables (Equation 5.2 was used). The length of the coil was made 120.0 cm long, for it to fit into the limited space of the cryostat and then other parameters were determined to make

the coil operational. From Figure 5.3, the points of intersections give the optimum number of turns and magnetic flux density at the different operating frequencies. It was decided to keep the maximum frequency of the signal at 100 Hz in order to keep the noise level lower than the signal generated due to the diamagnetic response of a superconducting specimen at the pickup coil. From Figure 5.3, it could be deduced that if a frequency of 100 Hz was used, a maximum magnetic flux density of 1085 μT was produced. The maximum operating current was limited to 37 mA for critical temperature characterisation. With this current, a maximum magnetic field of 1085 μT could be obtained. So, at 100 Hz, the number of turns that gives the optimum solution is about 2800 turns. However, a magnetic field of 1085 μT could hinder the experiment of T_c characterisation. A magnetic flux density above 100 mT affects the susceptibility curves, resulting into less steep transitions (normal to superconducting) for the χ' against temperature curves for T_c determination, accompanied by a decrease in T_c [34][46].

Nevertheless, the magnetic field (calculated from Equation 5.2) could be controlled by regulating the current by adjusting the voltage applied at the primary coil.

Table 5.1 gives the parameters of the primary coil which was designed and built:

Table 5. 1 Primary coil's parameters

Parameter	Value
Magnetic Flux density, B (in mT)	0–23
Number of Primary coil	1
Number of turns	2800
Length of primary coil (in mm)	120
Inner diameter (in mm)	25
External diameter (in mm)	28.5
Current rating at a frequency of 53 KHz (in mA)	729

A primary coil of 120.0 mm long, 42.0 mm wide and having an internal diameter of 25.0 mm was built. A two-dimensional drawing of the primary coil is shown in Figure 5.4. The current fed to the primary coil was adjusted by varying the voltage across it to obtain the appropriate

magnetic field. Figure 5.5 is a picture of the actual primary coil used for AC susceptibility measurements.
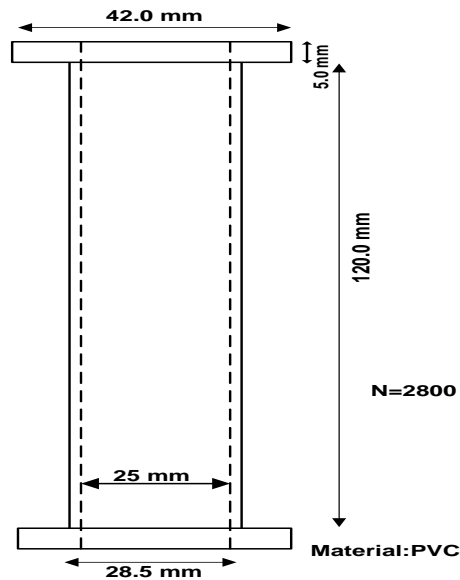
Figure 5. 4 Primary coil's schematic.

Case Study 1:

Using Equation 5.2

$I = 4.0\ mA \quad at \ \ B = 0.117\ mT$

$I = 0.40\ mA \quad at \ \ B = 11.7\ \mu T$

The average resistance of the coil could be calculated using Equation 5.3

Take resistivity ϱ for copper as 16.9 nΩ/m under room conditions.

$R = 18.4\Omega$

The inductance of the coil was calculated from Equation 5.4;

$L = 52.4\ mH.$

From Equation 5.5;

$Z = 37.7\ \Omega\ \ at\ f = 100\ Hz.$

Figure 5. 5 Picture of the primary coil built.

This is the theoretical impedance of the primary coil at a maximum frequency of 100 Hz. A low frequency was chosen with the aim of decreasing the amplitude of the undesired harmonics produced at the secondary coil. However, the practical values of R, L and Z deviated from the theoretical values. The main cause of these deviations was the fact that the wire was subjected to stress and strain during the fabrication process and consequently the end result was a coil made up of torn wire with non-uniform diameter.

5.3.2 Design of the Secondary Coil

There exist two secondary coils connected in series and wound in opposite direction such that the voltage induced in each empty secondary coil, cancels each other. In the presence of a superconducting sample at one of the secondary coils, the resultant voltage across the secondary coils is not zero due to the superconducting sample's magnetisation. The dimensions of the secondary coils were chosen so that they could be accommodated into the primary coil. Moreover, the secondary coils should provide adequate space to house bulk samples.

Referring to Equation 5.6 and Equation 5.7, it can be deduced that the number of turns per unit length n of the secondary coil and the sample's volume V_{sample} influence directly the value of the induced voltage at the secondary coils due to the diamagnetic response of the superconducting specimen. This voltage should at least be equal to the resolution of the IO Tech

70

Daqbook 2000 data acquisition system which was used to read the induced voltage. So, a trade-off was made between the size of the pickup coils, which depends on the number of turns and sample's volume, and the magnitude of the voltage induced. The number of turns does not exceed 200 per secondary coil as shown in Figure 5.6. AWG 39 wire, whose diameter is 0.0897 mm, was chosen for the secondary coil to increase the number of turns in a limited space.

(a)   (b)
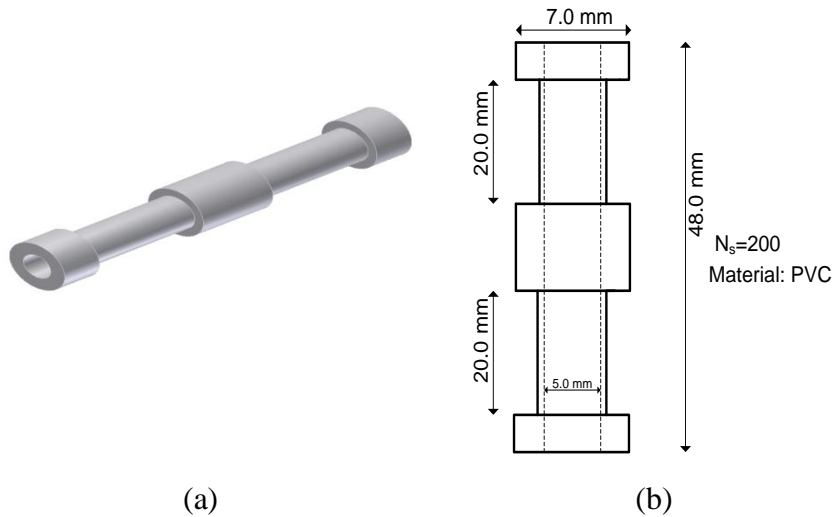
Figure 5. 6 (a) 3D diagram for secondary coil used for bulk samples (b) Schematic of the secondary coil built for bulk samples characterisation.

The pickup coil for the bulk samples is shown in Figure 5.6. The induced voltage produced at the secondary coil (calculated from Equation 5.6) should at least be equal to the resolution of the 16 bits daqbook, IOTech DaqBook 2000 data acquisition card, to be picked-up by the latter. The daqbook has a resolution of 2.38 μV. The measured voltage at the pickup coil is given by Equation 5.6. The rms voltage induced is proportional to the amplitude of the fundamental of the AC susceptibility χ and the frequency f of the AC voltage and the rms value of the applied alternating magnetic field H_{rms} and volume of the sample V_{sample}. According to Couach and Khoder [48] and Goldfarb and Minnervini [62], the rms induced voltage V_{rms} for a small cylindrical sample inside one of the secondary coil is given by,

$$V_{rms} = \frac{1}{\alpha'} V_{sample} f H_{rms} \chi. \tag{5.6}$$

Where α' is a calibration constant which represents the mutual inductance between the secondary and primary coils.

If the dimensions of the sample were small compared to those of the pickup coil, the calibration coefficient α' could be determined by the geometry of the secondary coil [2]:

$$\alpha' = \frac{10^7}{8\pi^2} \frac{(l^2 + 4d^2)^{1/2}}{N_s}, \tag{5.7}$$

l is the length of the secondary coil, d is the diameter of the coil and N_s is the number of turns at the secondary coil.

From Equation 5.6, it can be deduced that the volume of the sample should be sufficiently big and the value of α' should be sufficiently small so as to maximise the voltage induced. This is explained by the fact that the induced voltage was measured by comparing the flux displaced in the occupied coil with the empty pickup coil. The AC susceptibility stage should be designed in such a way that the sample subjected to AC susceptibility measurements gives a good signal (induced voltage) to noise ratio for accurate measurement of the sample's AC susceptibility.

Case Study2:

The secondary coil used to characterise the bulk sample was assigned the following parameters:

$l = 20.0 \ mm; \ d = 6.0 \ mm; \ N_s = 200; \ \alpha' = 14.8 \ A \ m^2 V^{-1} s^{-1}$;

The minimum $V_{sample} = 72 mm^3$

The minimum applied $H_{rms} = 9.33 \ A - t/m$ at the primary coil

From Equation 5.6

$V_{rms} = 0.454 \ \mu V$ at $\chi_1 = 0.1$

Clearly, the available daqbook did not meet the specified nanovolt resolution. So, the voltage induced at the pick-up coil should be sufficiently large enough for it to be detected by the 16 bits IOTech DaqBook 2000 module. The minimum average volume of the sample was estimated to be $7.2. x\ 10^{-8} m^3$ and the minimum rms current through the primary coil was 0.4 mA. From a theoretical approach, neglecting the demagnetisation effect, the minimum voltage for the sample was estimated to be $0.454\ \mu V$ at a frequency of 100 Hz and a susceptibility of 0.1 (using Equation 5.6). Owing to demagnetisation and losses, it was assumed that this value dropped to $0.227 \mu V$ (50% of theoretical value). The voltage output from the secondary coil was then amplified by a differential amplifier by a factor of 51 to increase the sensitivity of the susceptibility measurement system, yielding to a voltage of magnitude $11.6\ \mu V$. The 16-bits IO Tech DaqBook 2000 module, which can work with a minimum reference voltage of $\pm 0.156V$ (2.38 μV resolution), was able to measure the minimum voltage of $11.6\ \mu\ V$ (at $\chi_1 = 0.1$). The voltage could be further amplified if the need arises.

5.4 Testing and Validation of the Primary Coil and the Secondary Coil

The primary coil was tested to verify if the desired range of magnetic field could be produced. The material science laboratory was not equipped with a Hall effect sensor at the time when the research was conducted. So, the secondary coil was used as a magnetic field sensor to measure the magnetic field produced at the center of the primary coil. At the same time, the ability of the secondary coil to pick-up magnetic field was assessed. Figure 5.7 shows how the coils were set up for testing and validating their functionality. The primary coil was connected in series with an AC voltage source (function generator or variac). The power resistor was used as a current sensor. An ammeter was connected in series with the primary coil to monitor and measure the current flowing through the coil.
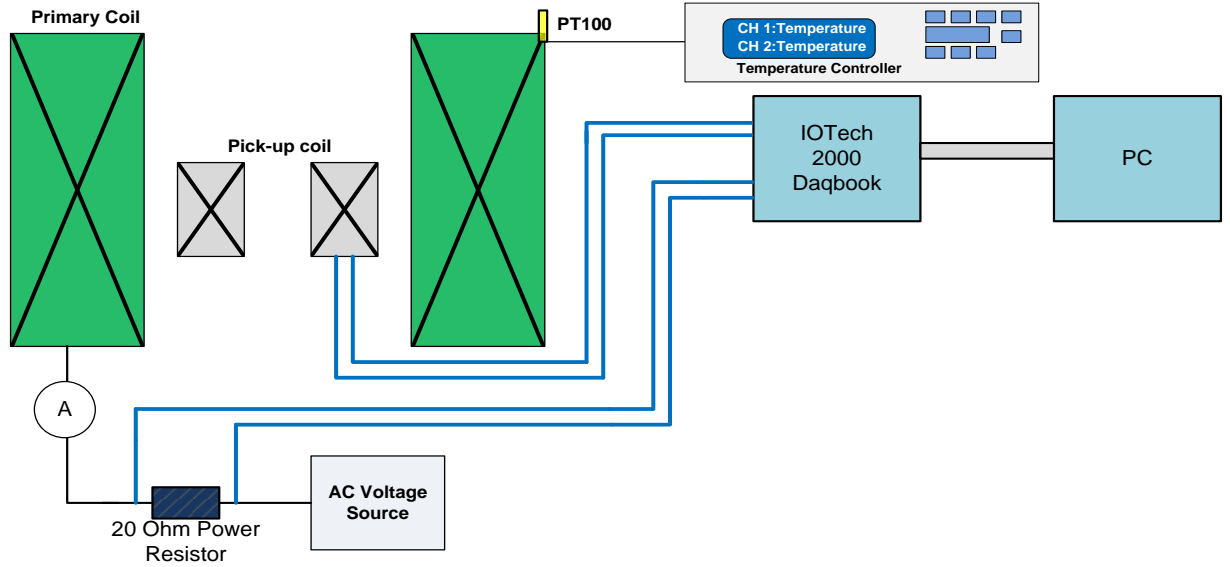
Figure 5. 7 Apparatus set up for testing and validating the primary and secondary coils.

The voltage across the power resistor was fed to the IOTech DaqBook 2000 data acquisition card for current measurement and logging.   The voltage picked up by the secondary coil, which is centered inside the primary coil, is fed to the daqbook for real-time measurement and logging. A program written in DaisyLab software was used to interface the data-acquisition card with a PC and to manage the data logging. The PT-100 was used to monitor the temperature of the primary coil.

Equation 5.2 was used to calculate the magnetic field produced inside the primary coil. The primary and secondary coils operate satisfactorily as long as the desired range of magnetic field is detected inside the primary coil by the sensing coil.
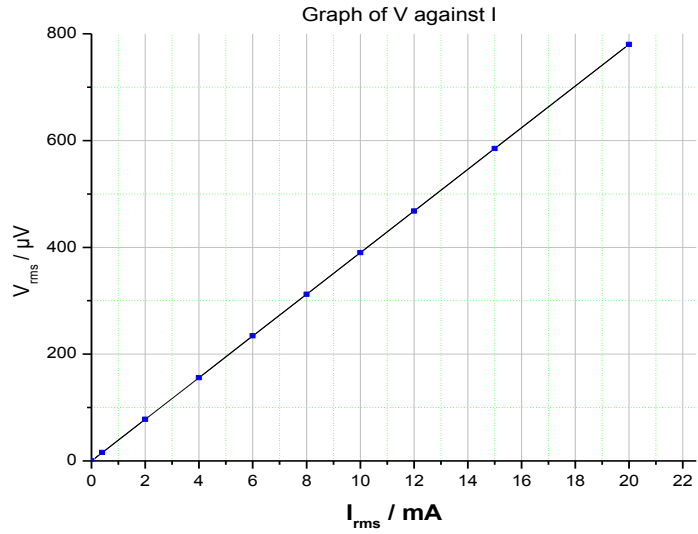
Figure 5. 8 Graph of V_{rms} against I_{rms} for I_{rms} in the range of 0 to 20 mA.

Figure 5.8 shows the variation of the voltage picked up at the centre of the primary coil by the sensing coil when the primary coil is fed with AC current in the range of $0\ to\ 20\ mA$. A current of $0.4\ mA$, giving rise to a magnetic field of 11.7 μ T, would be used for AC susceptibility characterisation against temperature. In the range of $0\ to\ 20\ mA,$ the primary coil operated satisfactorily with no excessive Joule heating noted under cryogenic conditions.
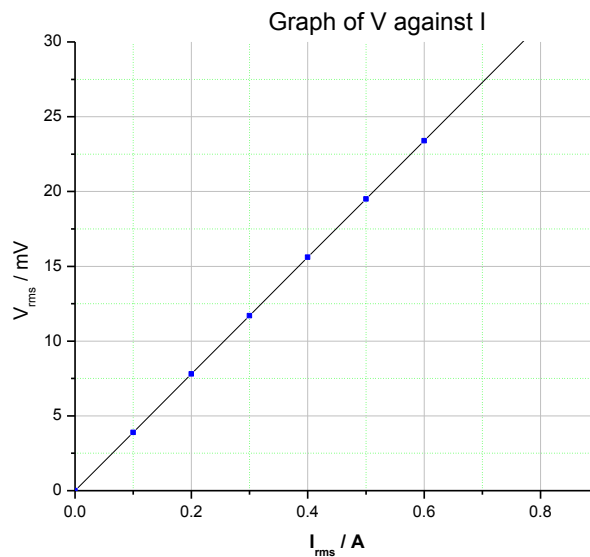
Figure 5. 9 Graph of V_{rms} against I_{rms} for I_{rms} in the range of 0 to 0.8 A.

Figure 5.9 shows the variation of the voltage picked up at the center of the primary coil by the pick-up coil when the primary coil is driven with alternating current in the range of 0 to 0.8 A.

High current (of up to 0.8 A) was used for susceptibility measurement against magnetic field under cryogenic conditions. The primary coil would be placed into a nitrogen bath for AC susceptibility measurement against magnetic field. Indeed, under cryogenic conditions, Joule heating would have little negative impact on the functionality of the primary coil. Hence, the primary coil could produce a maximum field of 20 mT (from Equation 5.2, it can be deduced that $B = 20.5\, mT$ when, $I = 0.7A$) without damaging the coil. During testing, the current was allowed to flow for a maximum time of 2.0 s. The apparatus was then switched off to prevent excessive Joule heating.

In conclusion, the primary coil and the secondary coil met the design specifications. The primary coil can produce the specified range of magnetic field, while the secondary coil can satisfactorily detect the magnetic field produced inside the primary coil.

5.5 Material Selection

The sample to be studied was cooled using a Cryomech Model GB15 closed loop helium cryo-cooler. The material with which the sample would be in direct contact for the cooling purpose should have the following properties:

- low heat capacity material such that the cooling of the stage took place quickly.
- the material needs to have an insignificant magnetic moment.
- The material should be malleable to some extent, such that it could be transformed to suit the tailored made application.

Few materials satisfy all these three characteristics. Ideally sapphire, Al_2O_3 , which has a thermal conductivity of the order of 3.0 $x\ 104\ W/mK$ at 77 K [63] should have been used for the stage fabrication because it satisfies all these three properties. For this design, it was decided to use silicon wafer, which has a thermal conductivity of about 2.0 $x\ 10^4\ W/mK$ at 77

K [64], instead of sapphire which was not available. The thermal conductivity of silicon and sapphire varies with temperature and sapphire has an overall better thermal conductivity than silicon. But silicon is less expensive and its thermal conductivity is rather good. However, the Si wafer is very brittle. Cautionary measures, like using a very sharp scriber, were taken and a piece of Si was successfully cut. For T_c characterisation, the Si sample holder was attached to a copper stage for AC susceptibility measurements. Aluminium probe instead of Si was used for AC susceptibility measurements in the determination of critical current densities of superconducting specimens. Aluminium is a non-magnetic material and has a thermal conductivity of the order of 10^3 W/mK at 77 K [63]. However, there was some eddy current response associated with aluminium.

 PVC was used to make the core of the primary coil. PVC is a non-magnetic material with very poor thermal conducting properties. Furthermore, PVC is cheap and readily available.

5.6 The Lock-in-Amplifier

The output signal from the susceptometer was fed to a lock-in amplifier which acted as a discriminating voltmeter, measuring the in-phase and out-of-phase fundamental voltages. As it could be deduced from Equation 4.38 in Chapter 4, the real and imaginary component of AC susceptibility could be found from the in-phase and out-of-phase voltages.

A lock-in amplifier was expected to measure very small AC signal in a noisy environment. The software-based lock-in amplifier should measure voltage signal at a desired frequency accurately even if the noise level is much higher than the magnitude of the signal. It must reject noisy signals at frequencies other than the reference frequency. The lock-in amplifier was presumed to be practical and accurate in measuring very small signal with a bandwidth as small as 0.01 Hz.

5.6.1 The Mathematics and Theory behind the Function of the Lock-In Amplifier

The lock-in amplifier was implemented in DASYLab 10 software environment. It used a reference signal at a chosen frequency to detect a signal component at the reference frequency from a noisy environment. The reference signal was an external signal which was a sine output from a function generator. The computer via the16 bits daqbook, IO Tech Daqbook 2000, digitalised signals via an on board analogue to digital converters. The digitalised signal (from the pick-up coil) was then filtered by a bandpass filter and then multiplied with the reference signal, which was phase-shifted, as shown in Figure 5.10. The lock-in amplifier, described in Figure 5.10, was implemented in DASYlab environment (refer to Appendix A)
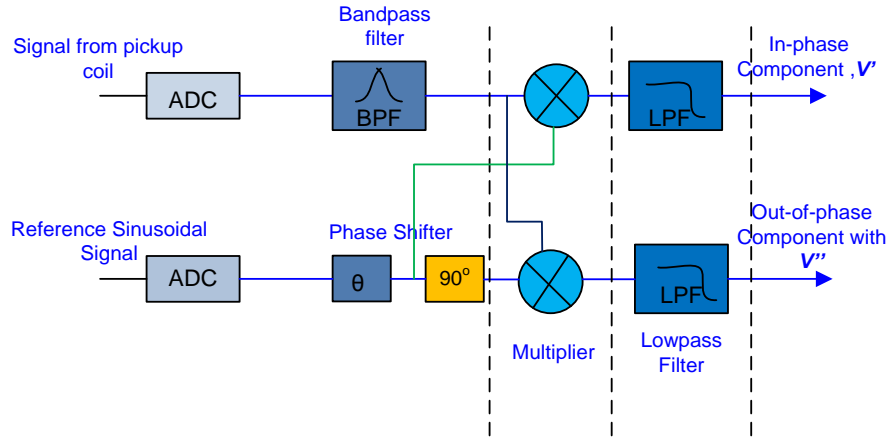
Figure 5. 10 Block diagram of lock-in amplifier implemented in DASYLab 10.

The mixer multiplied the input experimental signal with the reference signal after being band-passed filtered as shown in Figure 5.10. The resulting signal from the mixer was low-pass filtered to extract the experimental real and imaginary signal components, which were at the reference frequency.

The input signal, due to the diamagnetic response of a superconducting specimen, came from the pick-up coil and it was in the form as represented by Equation 5.8;

$$V(t) = V_0 \sum_0^\alpha [\chi_n' \sin(n\omega t) - \chi_n'' \cos(\omega t)] . \qquad (5.8)$$

The fundamental signal was given by:

$$V_1(t) = V_o[\chi_1' \sin(\omega t) - \chi_1'' \cos(\omega t)], \qquad (5.9)$$

V_o is calculated from Equation 4.37.

Since the origin of time is arbitrary, the fundamental signal V_1 and the reference signal V_{ref} could be rewritten in the form:

$$V_1 = V_s \cos(\omega t), \qquad (5.10)$$

$$V_{ref} = V_r \cos(\omega t + \alpha), \qquad (5.11)$$

α is the phase angle between the experimental signal and the reference signal.

A phase shift of θ was deliberately introduced to ensure that there is a phase difference between the reference voltage and the signal from the pickup coil.

V_s and V_r are the amplitudes of V_1 and V_{ref} respectively. V_r is known whereas V_s needs to be determined to estimate the real and imaginary AC susceptibilities as explained below.

The detection process involved the multiplication of the fundamental signal across the pick-up coils and the reference voltage. For the analysis, only the fundamental was considered since higher order harmonics would be automatically filtered by the band-pass and low-pass filters (having a cut-off frequency slightly higher than the fundamental frequency) which were part of the lock-in amplifier. The voltage signal obtained after multiplication:

$$V = V_s \cos(\omega t) . V_r \cos(\omega t + \alpha), \qquad (5.12)$$

$$V = V_s . V_r \cos(\omega t)(\cos \omega t \cos \alpha - \sin \omega t \sin \alpha), \qquad (5.13)$$

$$V = \frac{1}{2} V_s . V_r \cos \alpha + \frac{1}{2} V_s . V_r \cos(2\omega t + \alpha) . \qquad (5.14)$$

The higher order harmonics in Equation 5.14 were low-passed filtered, leaving only the DC component;

$$V' = \frac{1}{2} V_s . V_r \cos \alpha. \qquad (5.15)$$

Now the reference voltage was further shifted by 90° yielding into the imaginary reference signal:

$$V'_{ref} = V_r \cos(\omega t + \alpha - 90^0) \,. \qquad (5.16)$$

The fundamental signal from the picked up coil (Equation 5.10) was multiplied with the shifted reference voltage (Equation 5.16).

$$V = V_s \cos(\omega t) \,. V_r \cos(\omega t + \alpha - 90) \,, \qquad (5.17)$$

$$V = \frac{1}{2} V_s V_r \sin\alpha + \frac{1}{2} V_s V_r \sin(2\omega t + \alpha) \,. \qquad (5.18)$$

After the signal was low passed filtered, the DC component from Equation 5.18 was extracted by lock-in amplifier:

$$V'' = \frac{1}{2} V_s V_r \sin\alpha. \qquad (5.19)$$

V' and V'' are measured and recorded by the software-based lock-in amplifier implemented in DASYLab environment.

Since the origin of time is arbitrary, the signal with respect to the reference voltage (with phase difference of $+\alpha$) could be represented as follows:

$$V_1 = V_s \cos(\omega t - \alpha), \qquad (5.20)$$

$$V_1 = (V_s \cos\alpha)\cos\omega t + (V_s \sin\alpha)\sin\omega t. \qquad (5.21)$$

As explained in Chapter 4, the first harmonics of the induced voltage at the secondary coil due to the diamagnetic response of the superconducting specimen is:

$$V_1 = V_0 \chi'_1 \sin(\omega t) - V_0 \chi''_1 \cos(\omega t) \,, \qquad (5.22)$$

V_0 was estimated from Equation 4.37.

Comparing Equation 5.21 and 5.22;

$$V_s \sin\alpha = V_0 \chi_1',$$ (5.23)

$$V_s \cos\alpha = -V_0 \chi_1'',$$ (5.24)

From Equation 5.15, Equation 5.19, Equation 5.23 and Equation 5.24, the values of the in-phase and out-of-phase components of the material's susceptibility could be calculated. For the purpose of this research, the exact values of the material's susceptibility were not required as we were interested in the relative susceptibility values, in order to establish trend changes which have the potential to provide us with information about the material's characteristics as temperature and magnetic field vary.

The desired harmonics could be extracted by simply changing the frequency of the reference signal to the desired signal component's frequency.

The real susceptibility, χ' and the imaginary susceptibility χ'' are directly proportional to the phase angles α and $\alpha - 90^0$ respectively. If the temperature of the primary coil varied, the amplitude of the in-phase and the out-of-phase components would vary due to a change in the coil's impedance. As a result, the phase angle would change. So, if the primary coil's temperature varied, so did the phase angle and the measurements of the real and imaginary susceptibilities would not be accurate. A stepper motor could be used to compensate for a variation in the phase angle by moving the sample up and down along the vertical axis of the primary coil [2] [46]. For this research, no stepper motor method was used. For T_c characterisation, the current used was set to 0.4 mA. A negligible rise in temperature of the coil occurred, owing to a small resistive power (which was approximately 2.7 µW), and was dissipated across the primary coil. For the generation of a high magnetic field to study granular connection in superconductors, the primary coil was kept in a liquid nitrogen bath (at 77.0 K) minimising joule heating when the coil carried a current up to 0.7 A.

5.6.2 Implementation and Testing of the Lock-in-Amplifier in DASYLab

The lock-in-amplifier was implemented in DASYLab DSP type software environment (Appendix A). Different block available from DASYlab library, mainly consisting of a multiplier block, a delay block, an input module and a filter block, were connected to implement the software-based lock-in-amplifier.

The DSP lock-in amplifier was tested with the injection of a square wave which is analogous to a noisy signal made up of odd harmonics. Then, the program was tested with two combined signals, 90 degrees out of phase.

5.6.2.1 Testing the Lock-in-Amplifier Filtration Ability

The general form for a square wave is given by a Fourier series given by Equation 5.25 and it can also be written in the form given by Equation 5.26, where A, B and C are constants dependent on the magnitude of the square wave.

$$S(t) = \frac{4}{\pi} \sum_{n=1,3,5,\cdots}^{\infty} \frac{1}{n} \sin\left(\frac{n\pi x}{L}\right) , \tag{5.25}$$

$$S(t) = A \sin(\omega t) + B \sin(3\omega t) + C sin(5\omega t) + \cdots \tag{5.26}$$

A 60 Hz sinusoidal signal, generated from by a signal generator, was used as the reference signal. Figure 5.11 shows the fast Fourier transform before the square wave was fed to the lock-in amplifier.

82
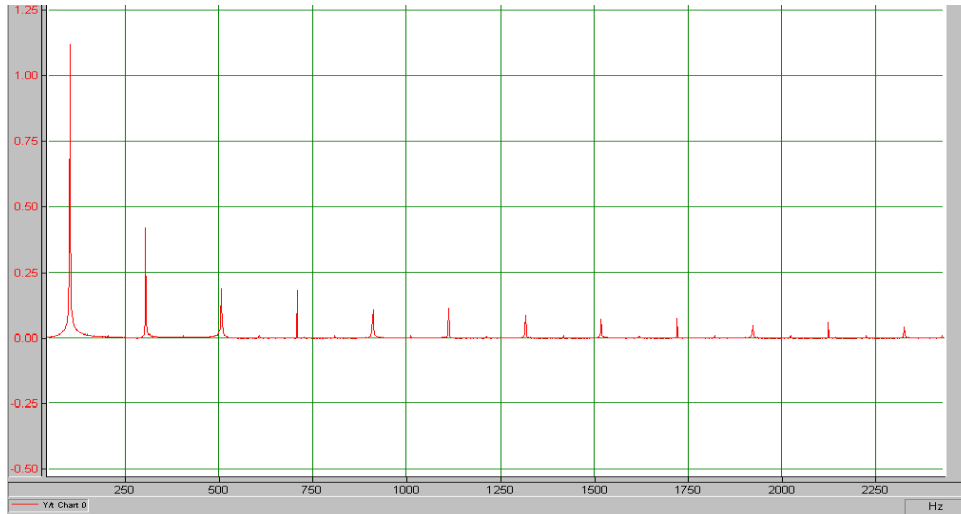
Figure 5. 11 Screen shot of the Fast Fourier transform of square wave.

The lock-in amplifier extracted the first harmonic of the square wave and the following was obtained:
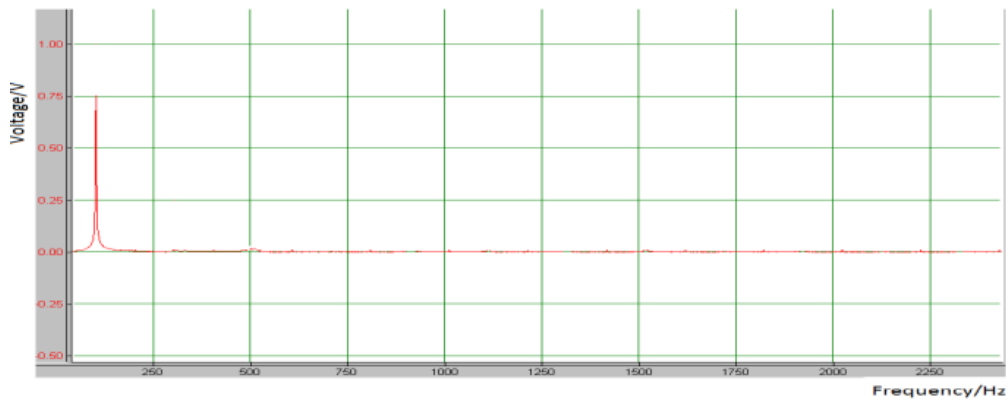
Figure 5. 12 Screen shot of Fast Fourier transform of square wave fundamental extracted by the lock-in-amplifier.

In conclusion, the program was able to extract the fundamental components of the square wave out of the other harmonics. The magnitude of the extracted fundamental is less than its true value shown in Figure 5.12. This was due to the filtration process. Since we were interested in the relative values AC susceptibility for trend changes, the output was taken as given by the program with no adjustment to restore the true amplitude of the fundamental voltage.

5.6.2.2 Testing the Lock-in-Amplifier's Ability to Act as a Discriminating Voltmeter.

After testing the ability of the lock-in-amplifier, implemented in DASYLab, to act as an efficient filter, the latter was tested for its effectiveness in acting as a discriminating voltmeter to extract the in-phase and the out of phase fundamentals of the signal.
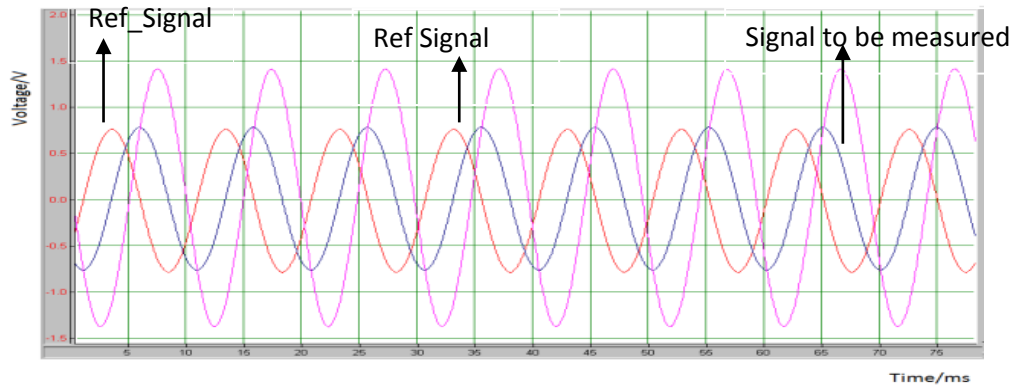
Figure 5. 13 Screen shot of the reference signals and the experimental signal to be measured.

The testing signal shown by Equation 5.27 was generated in DASYLab from an external signal from a function generator. The testing signal and the reference signals are shown in Figure 5.13.

$$V(t) = A\sin(\omega t) + B\cos(\omega t) \tag{5.27}$$

The values of A and B were varied and then measured (by lock-in amplifier) and calculated values for the in-phase (V') and the out-of phase (V'') components were tabulated in Table 5.2.

Table 5. 2 In-phase component V' and out-of-phase component V''.

A	B	V'' (measured)	V'' (calculated)	Error/%	V' (measured)	V' (calculated)	Error/%
0.95	-1.425	0.4410	0.4513	2.28	-0.6381	-0.677	5.75
1.53	-2.295	1.171	1.705	-0.176	-1.709	-1.756	2.75
1.97	2.955	1.983	1.9405	2.15	-2.865	-2.910	1.55
1.19	1.785	0.7026	0.7081	0.777	1.092	1.062	-2.83
2.28	3.42	2.677	2.599	-3.00	3.9067	3.899	-0.197

The measured in-phase component V' and the measured out-of-phase component V'' extracted by the lock-in-amplifier agreed satisfactorily with the calculated or theoretical values as shown in Table 5.2. It can be concluded that the lock-in-amplifier was successfully implemented in DASYLab environment. The lock-in amplifier was capable of acting as a discriminating voltmeter, extracting the in-phase and the out-of-phase components of a signal. Moreover, the software-based lock-in-amplifier effectively extracted the fundamental component of a square wave signal composed of odd harmonics. The software-based lock-in amplifier was then used to measure the fundamental in-phase and out-of-phase components of the magnetic response of superconducting samples.

5.7 Summary

The DSP-enhanced susceptometer was implemented and tested at the material science laboratory. The performance of the primary and the secondary coils were evaluated. The primary coil was able to produce a magnetic field within the specified range and the secondary coils satisfactorily detected the magnetic experimental signal. Due to limitations like small budget, lack of equipment, etc., some of the specifications of the lock-in-amplifier, defined in section 5.2, were not met. For instance, the magnetic and reference signals were sampled at 25 kHz instead of 100 kHz and the resolution was in the order of microvolt instead of nanovolt. However, even though the susceptometer has a few practical limitations, its performance was assessed to be satisfactory. The low-pass filtering ability of the lock-in amplifier was tested with a square wave, which is made up of odd harmonics, and it was able to extract the fundamental component. Moreover, the ability of the lock-in amplifier to act as a discriminating voltmeter was also evaluated. The in-phase and out-of-phase voltage components were extracted with less than 6% error (compared to the theoretical values). Overall, the performance of the software-based lock-in-amplifier is decent.

The traditional way to measure small signals buried in a noisy environment is to use an expensive stand-alone lock-in amplifier. The implementation of a software-based lock-in amplifier is defined by low cost PC-based technologies (hardware and software) in creating a virtual instrumentation to measure small magnetic signal and the development time is

significantly reduced (compared with the development of a traditional lock-in-amplifier). The paradigm shift happened as the functions of a conventional lock-in amplifier were performed by a PC and an off-the-shelf data-acquisition system. The DSP-enhanced susceptometer was able to measure signal of microvolt magnitude in a noisy environment. A reference voltage of 50 Hz was used to enable the lock-in-amplifier to focus in a narrow bandwidth while extracting the fundamental signal. The hardware functionality of the lock-in amplifier could be customized in a versatile software environment to suit specific needs of the instrumentation. So, the customized software-based lock-in-amplifier could also be classified as a flexible solution.

Chapter 6 Experimentation

Bulk YBCO discs were prepared in the material science laboratory by sintering pressed high purity YBCO powder in an oxygen atmosphere. The pellets were sintered then cut into rectangular slices. YBCO bulk specimens were doped with hydrogen and then investigated by conducting resistivity and AC susceptibility measurements.

6.1 YBCO Pellets

6.1.1 YBCO Pellets Fabrication

Conventionally, YBCO bulk samples are fabricated via the 'shake and bake' method using yttrium oxide, barium carbonate and copper (II) oxide, combined in the right proportion, followed by annealing in an oxygen atmosphere. The chemical formula for the reaction is:

$$Y_2O_3 + 2\ BaCO_3 + 3\ CuO \rightarrow 2\ YBa_2Cu_3O_7.$$
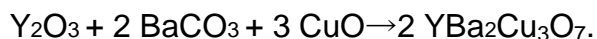
However, for the purpose of this research, YBCO was not fabricated as described above. It was rather sintered from commercially available high purity YBCO powder in the materials science laboratory. The YBCO powder, with a purity of 99.9%, was pressed into pellets. Pellets had a weight of 2.00 g and a diameter equal to 20.0 mm and 5.0 mm thick. Contamination of the precursor powder was minimised by always cleaning the balance's tray, the spatula and the die (used to press the YBCO) with ethanol prior to weighing and pressing. Moreover, minimum adhesion of YBCO powder to the spatula and the tray used for weighing purposes was observed.

Figure 6. 1 Tube furnace used for the sintering of YBCO pellets**.**

After pressing YBCO discs, using the hydraulic press, under a pressure of 2000 KPa, the discs were placed in an alumina tube (which has a melting point of about 2000 ^{0}C) and then loaded into a tube furnace. The furnace was flushed for a few minutes with Argon before sintering in an oxygen atmosphere. The oxygen was continually supplied from a pressurised oxygen cylinder, maintaining a positive flow of oxygen from one end of the tube to the other until the sintering was completed. Figure 6.2 shows an YBCO disc sintered in the material science laboratory.

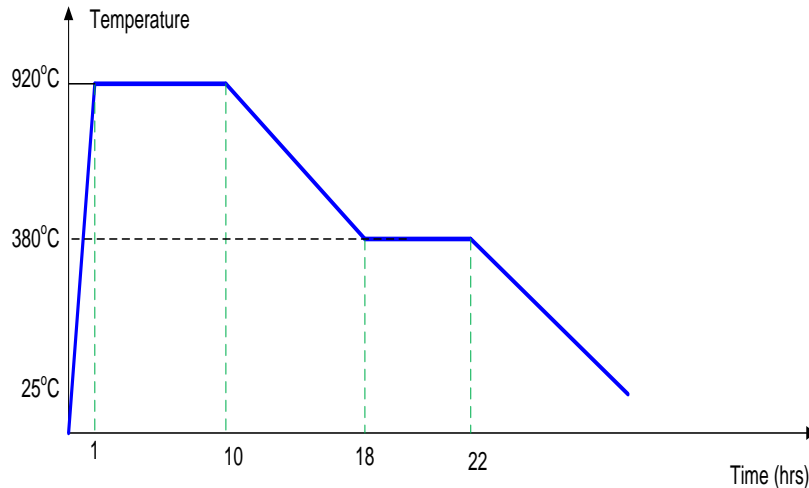Figure 6. 2 Top view of YBCO disc sintered in the tube furnace.

Figure 6. 3 Heat profile for YBCO disc sintering.

Figure 6.3 shows the heating profile for the sintering of bulk YBCO discs. The loaded discs were heated up to 920 ^{0}C, then kept constant at 920 ^{0}C for a duration of 9 hours in an atmosphere of flowing oxygen. Pellets were then cooled at a rate of 1.13 ^{0}C per minute to 380 ^{0}C. The YBCO pellets were held at 450 ^{0}C for eight more hours still under an oxygen atmosphere. After a total of 22 hours of heat treatment, the furnace was cooled to room temperature, by switching it off.

6.1.2 Cutting of Bulk $YBa_2Cu_3O_{7-x}$ Specimens

The pellets needed to be cut after sintering into rectangular slabs such that they could be characterised by doing resistance and AC susceptibility measurements. The cutting was performed using a low speed Buehler diamond blade driven by an electric motor. Acetone was used as coolant during the cutting procedure. A coolant is necessary to enable the blade to cut properly extracting the heat generated due to friction between the blade and the YBCO specimen. Water was not used as it was reported that water degrades superconductivity [65] and this is not the case with acetone. The pellets were carefully clamped using the in-built clamp with which the cutting machine is equipped providing satisfactory mechanical support. The specimens were slowly cut into thin and long rectangular slabs. Long slabs with small

89

area of cross-section were desired so as to get a good signal-to-noise ratio with minimal current drawn for resistivity measurements. Moreover, minimum current led to minimal joule heating of the YBCO samples and the current leads. Relatively larger sections were cut for AC susceptibility measurement since the volume magnetisation eventually increases as the size of a specimen increases.

6.2 Hydrogen Doping

Hydrogen doping of HTS has been extensively done since the their discovered in the 1980's [61] [66] [67]. For this research, hydrogen doping was performed into a thick sealed stainless steel cell, shown in Figure 6.4, equipped with pressure gauge to monitor the pressure inside the cell and with a heater to heat the YBCO specimens, for diffusion purposes. First and foremost, a thin rectangular YBCO slab not exceeding 20.0 mm long, 4.0 mm wide and 2.0 mm thick was clamped to the heater inside the cell. Before the hydrogen was administered into the cell, the latter was first sealed and then flushed with argon for 5 minutes to remove potential contaminants initially present in the vessel. In general, hydrogen is absorbed by numerous metal and non-metallic compounds at relatively low temperature [68]. The hydrogen atoms interact rather weakly with foreign atoms both substitutional and interstitial sites in the materials' lattice to form hydride [69].

Pressurised hydrogen was introduced into the vessel. The vessel was pressurised to 1 atmosphere at room temperature before the heater was turned on and the pressure inside the cell was not allowed to drop to below 1 atmosphere. No absorption of H_2 occurs in the YBCO specimens at room temperatures [6]. The heater was turned on to heat the specimen to a temperature of 180 ^{0}C. Absorption occurs at around 170 ^{0}C [6] [61] and it was risky to go beyond a temperature of 200 ^{0}C as desorption of oxygen might occur [6]. Hydrogen diffused through the stainless steel and through the YBCO specimen. The YBCO specimen needed to be tested (AC susceptibility tests) to establish whether a significant amount of H_2 was absorbed by the specimen. No controller was attached to the doping system and consequently, the temperature regulation was done manually by controlling the voltage input fed to the heater. Eventually, the control was not as good as that of a well-tuned PID controller but it was rather

satisfactory. The average temperature did not exceed 190 ^{0}C
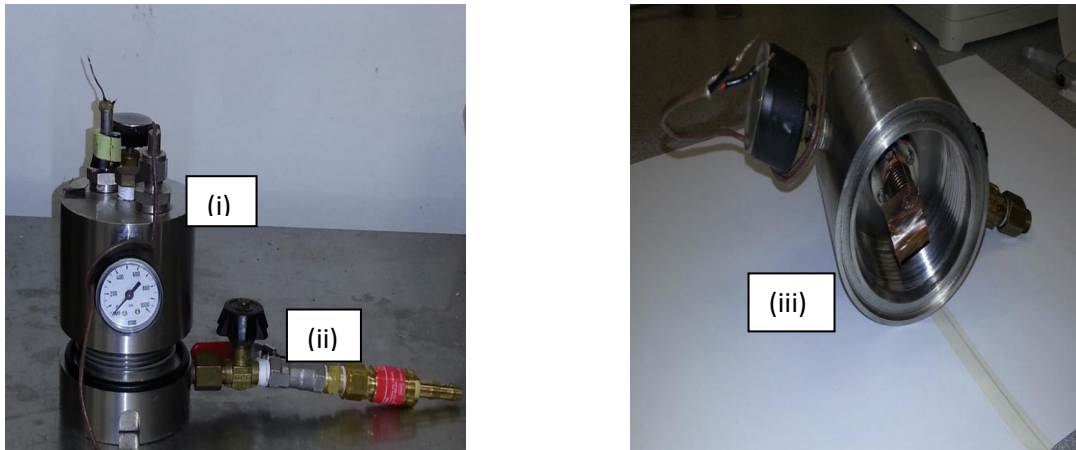
Figure 6. 4 Taylor-made vessel for hydrogenation of YBCO specimens. (i) hydrogen cell (ii) gas inlet (iii) specimen holder with heater.

One way to determine the amount of hydrogen absorbed by the YBCO sample is through X-ray diffraction. This was not done. The amount of time that the sample was exposed to hydrogen inside the cell, under the same conditions of pressure and temperature, was used as a parameter to determine the relative amount of hydrogen absorbed by the doped specimen. Table 6.1 summarised the doping that was done on one specimen. The specimen was successively doped with hydrogen and tested (AC susceptibility and resistive measurements for some).

Figure 6.5 explains and summarises the hydrogenation procedure through a flowchart.

Figure 6. 5 Flowchart explaining the hydrogenation procedure.

Table 6. 1- Summary of hydrogenation

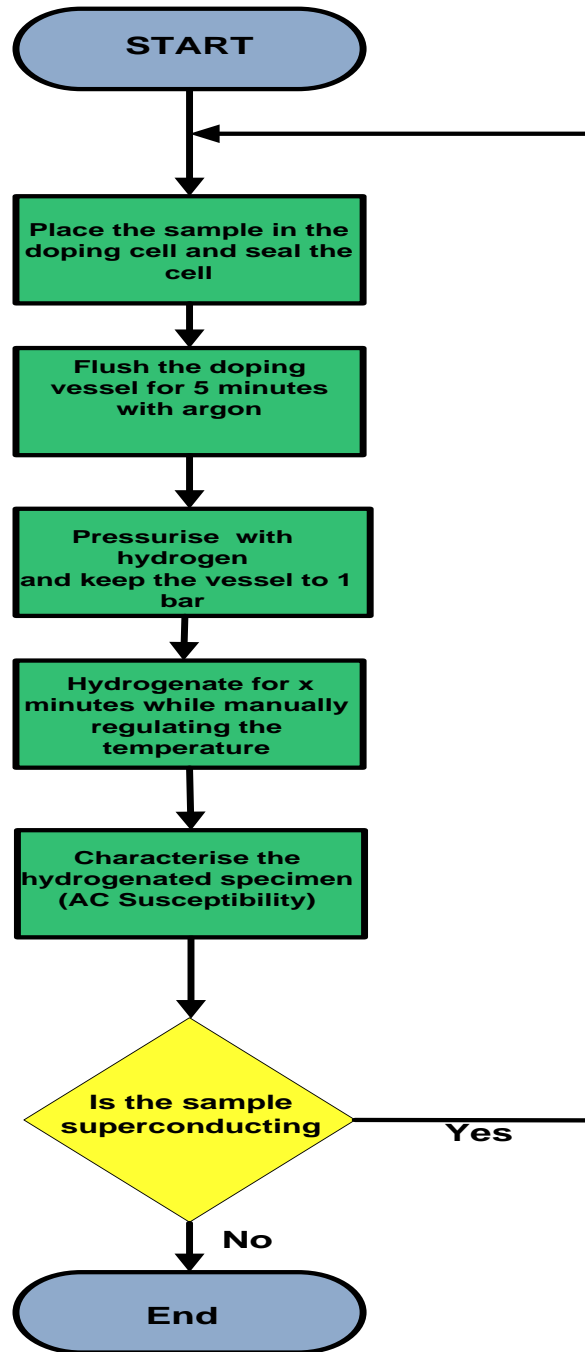| Sample	Total Doping time
Original Sample (undoped)	0
Hydrogenation_1	30
Hydrogenation_2	30+30
Hydrogenation_3	30+30+30
Hydrogenation_4	30+30+30+180
Hydrogenation_5	30+30+30+180+130
Hydrogenation_6	30+30+30+180+130+250

Table 6.1 shows the total time a sample (sample_1) was hydrogenated after each successive hydrogenation. Hydrogen was first administered into the cell which was pressurised to 1 atmosphere at room temperature and hydrogen was topped up to prevent the pressure from decreasing to below 1 atmosphere as long as the doping was going on. Hydrogen is a small molecule and it is readily absorbed by the materials (the stainless steel and the YBCO specimen). Since the hydrogenation was carried out at about 170 ^{0}C, no deoxygenation occurred [66]. So, the hydrogenation time was used as an indicator of the relative amount of hydrogen absorbed by a particular doped specimen. The hydrogen absorbed by the YBCO specimen was proportional to the total doping time (under the same conditions of pressure and temperature).

6.3 Resistance Measurements

Four-wire resistance measurements were done on YBCO specimens (bulk samples and bi-crystal). A constant current was fed to the sample to be tested and the voltage across the samples was measured. Good electrical contact was required to be able to conduct resistance measurements.

6.3.1 Contacts

Four wire resistance measurements were conducted on all specimens and required good electrical contact of wire and specimen. Contacts must also exhibit sufficient high mechanical strength to avoid rupturing of the contacts during setting up and under experimental cryogenic conditions. Under cryogenic conditions, contacts breaking occurred mainly due to the difference in thermal expansion coefficients of the superconductor and the contacts, placing additional stress on the contacts. Time was spent investigating methods, which provided the most effective electrical contacts. This section details the techniques and outcomes of the different types of electrical contacts investigated on rectangular YBCO samples having dimensions not exceeding 20.0 mm x 4.0 mm x 2.0 mm.

Indium and Copper Wire Contacts.

Indium soldering wire was used to join thin copper wires to a clean and polished YBCO surface. Copper wire was wrapped a few times around the YBCO slab and melted indium (melted using a soldering iron) was applied over the copper and the YBCO to bind them together as shown in Figure 6.6.
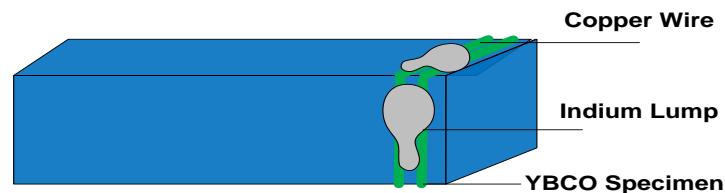

Figure 6. 6 Contact using indium and copper wire.

The indium lumps failed to adhere effectively to the surfaces of YBCO specimen and the copper wires. The lumps shortly came off after a few minutes as they were unable to withstand the stresses to which they were subjected due to cryogenic conditions. Moreover, the mechanical adhesion of indium to YBCO's surface was very poor.

Indium, Gold Sputtering and Copper Wire Contacts

In an attempt to create better adherence of indium lump with YBCO's surface, the surface of an YBCO specimen was sputtered with thin layer of gold after it had been polished and cleaned. Then, a few turns of copper wire was wrapped around the specimen before applying molten lumps of indium. This is illustrated in as shown in Figure 6.7.
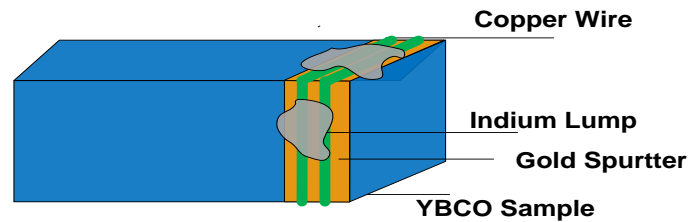
Figure 6. 7 Contact using indium, gold sputter and copper wire.

The resultant connections did not meet the mechanical adhesion criteria and the indium lump came off the surface even though the surface of YBCO was coated with gold.

Silver Paste and Stainless Steel Wire Contacts

Stainless steel wires of 0.2 mm thick were joined to YBCO's surface using silver paste. Silver bands (four in total) were painted on polished and cleaned YBCO's surface and the wires were wrapped a few times around the bands. Then, lumps of silver paste were applied carefully over the wires making sure that neighbouring bands did not intersect. Finally, a blower was used for drying. The specimen was exposed to the hot air blown until the silver paste was completely solidified bonding the steel wires with the YBCO.

Figure 6. 8 Contact using silver paste and stainless steel wires.

The mechanical adhesion between silver paste, the YBCO surface and the steel wire was very good. However, the contact poorly met the mechanical contraction criteria under cryogenic conditions. Under 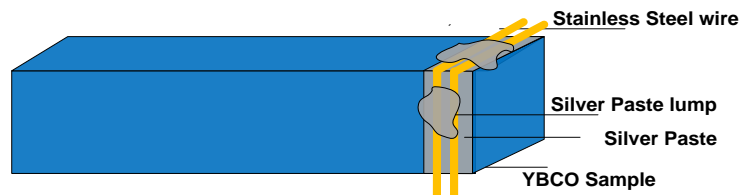cryogenic conditions, the contacts failed as the coefficients of linear thermal expansion of steel and silver paste differ. They contract at a different paste and consequently the steel wires got disconnected to YBCO's surface under cryogenic conditions.

Silver Paste and Silver Wool Contacts

To remediate to the problem of the difference in the linear thermal expansion coefficients of silver and steel, the contact had to be made with similar materials having more or less the same thermal coefficient. In this regard, silver paste and silver yarn (from silver wool) were used. Silver bands were painted and a few turns of silver yarn was carefully wrapped around the YBCO specimen and the yarn was covered with lumps of silver paste as shown in Figure 6.9. The silver paste was dried using a blower. Silver yarn was not used initially due to the fact that the silver wire available in the lab is very thin and it was very challenging to handle the silver yarn without breaking the yarn.

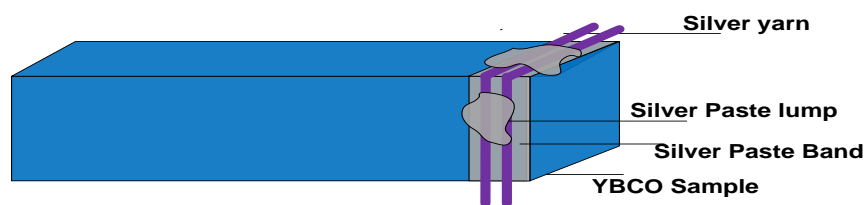Figure 6. 9 Contact using silver paste and silver wire.

The combination of silver paste and silver wool resulted into good electrical contacts. The mechanical adhesion was very good and no problems regarding mechanical stresses cropped up as it was the case for the other types of contacts described above. So, for resistive measurements of bulk YBCO samples, the contacts were made using silver paste and silver wool.

6.3.2 Resistive Testing

Thin slabs of YBCO were cut using a rotating diamond blade. Silver paste and silver wires were used to establish the contact for the 4-wires measurement technique used for resistive characterisation. The YBCO specimen was mounted on a purposed-made copper stage. Between the sample and the copper, a mica sheet of thickness 0.2 mm was placed using Apiezon N thermal grease to establish a good thermal contact but maintain electrical insulation. The silver yarn from each contact spot on the specimen's surface was carefully soldered to copper wires for current feeding and voltage measurements purposes. The distance between the voltage bands was made as large as possible to ensure a good voltage signal to noise ratio. Moreover, it is a good practice to keep a relatively large distance between the current and voltage contacts which aided to achieve a uniform current density.
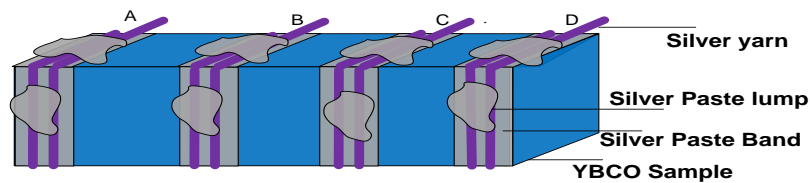

Figure 6. 10 The set-up for four-wire measurement technique for resistive characterisation.

Figure 6.10 shows how the contacts were placed along an YBCO specimen for resistive measurements. Leads A and D were used for current feeding whereas leads B and C were meant for voltage measurements.
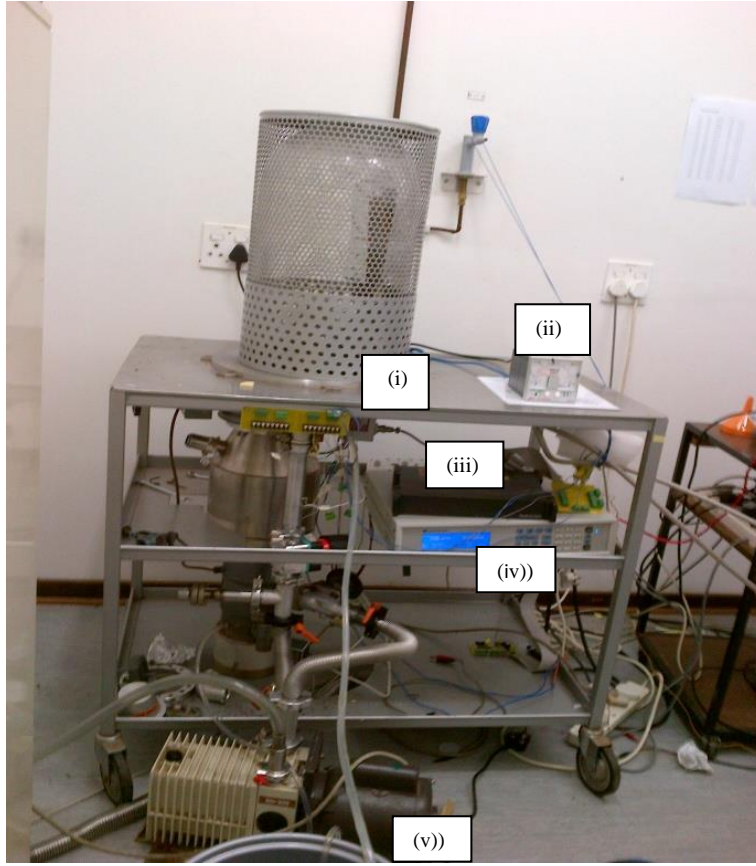
Figure 6. 11 Cryostat at work for resistance measurment experiment. (i): Bell jar cryostat (ii): Pressure gauge (iii) IOTech DaqBook 2000 (iv) Lake Shore Model 336 temperature controller (v) Rotary pump.

Figure 6.11 shows the bell-jar cryostat at work, measuring the resistance of a bulk YBCO specimen with temperature. The cold head of the cryostat was surrounded by a copper radiation shield, wrapped with several layers of Mylar, was attached to the first stage of the cold head. With the radiation shield in position and without a thermo-molecular pump, a minimum operating temperature of 65 K was achieved (which is cold enough to characterise YBCO specimens which normally have a $T_c \approx 92.0\ K$). A few turns of Lake Shore nichrome heater wire was wrapped around the copper stage to make the heater. Furthermore, a PT-100 temperature sensor was also clamped to the flat copper stage just next to the sample. The four silver wires from the silver bands on the specimen's surface were soldered to the current and voltage leads.

The initial attempt in using the Lake Shore Model 120 as a current Source was

problematic. This module generates a direct current, flowing between leads A and D, the measured voltage drop between B and C was very noisy in nature and a filter was not effective in removing the noise which was substantially higher than the signal. A solution to this problem was to use an AC current. In this regard, an AC current at a frequency of 60 Hz generated by a function generator was fed to the HTS specimen through leads A and D. A 100 Ω resistor was connected in series with the function generator and the specimen being tested. The voltage from the function generator was adjusted to 70 mV pk-pk when the specimen and the resistor were connected. The measured resistance of the specimen (measured by the IOTech Data acquisition system) was about 0.8 Ω at room temperature and the resistivity decreases as the specimen was cooled. So, a rather continuous and constant current having a rms value of about $0.35/\sqrt{2}$ mA was generated and fed to the specimen. Leads B and C were connected to the input of the IOTech Daqbook 2000 card. The IOTech DaqBook 2000 interfaced with DASYLab software over an Ethernet connection. A program was written in DASYLab to process the signal measured across leads B and C. The voltage across B and C was digitalised and filtered to remove the undesired high frequency noise.
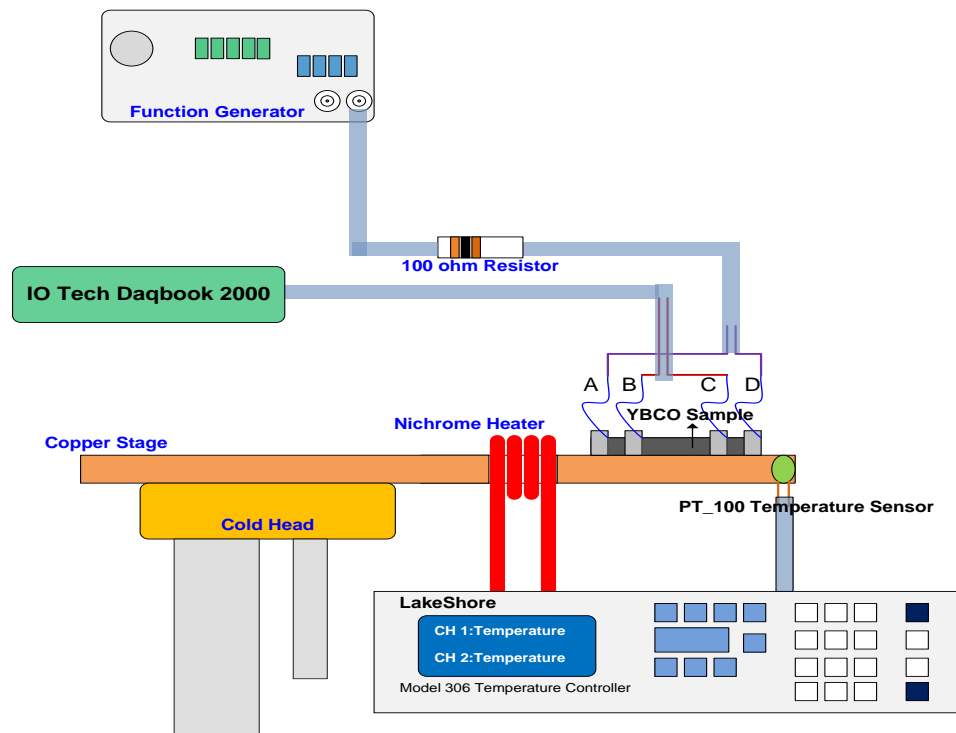

Figure 6. 12 Instrumentation and apparatus used for T_c characterisation of YBCO specimens.

6.3.2.1 Temperature Control

The Lake Shore Model 336 temperature controller was used for temperature control for resitivity testing experiment. The Lake Shore temperature controller was used in conjunction with a nichrome heater wound on the copper stage and a calibrated PT-100 thermometer attached to the stage as shown in Figure 6.12. PID output from the temperature controller drove the heater and stability was around within 55 mK. The current source from the temperature controller module was always kept on to avoid temperature transients which may arise in the specimen, the contact wired or anchored wiring. The stage was cooled at a rate of 0.1 K/min resistive testing. A slow cooling rate caused a significant decrease in the temperature gradient between the YBCO specimen and the copper stage to an almost negligible value. The current fed to the superconducting specimen was produced by an AC voltage source (function generator) connected in series with a 100 Ohm resistor and the superconductor as shown in Figure 6.12. The current remains almost constant as the resistance of the resistor is much larger than the superconductor's resistance, which is less than $1.0 \, \Omega$ at room temperature. A computer program (Appendix B) interfaced the Lake Shore Model 336 temperature controller over the Ethernet for remote temperature data logging and control. Simultaneously, the voltage data measured across leads B and C by the IOTech Daqbook 2000 module system were logged synchronously in DASYLab. The result for the resistivity experiment is shown in Appendix E.

6.3.2.2 Liquid Nitrogen-cooled Open Cycle Cryostat

Initially, the cryostat used for the experimentations was made up of a Cryomech cold head which was cooled by a closed loop helium circulation system, a Cryomech compressor and a bell jar mounted on stainless steel base-plate to keep vacuum as shown in Figure 6.11. This cryostat was used to characterise a virgin bulk sample specimen and the undoped bi-crystal specimen. *However, in February 2013, the Crymech Cryo-Cooler (GB-15 Model) stopped operating correctly due to a mechanical problem preventing the helium to reach the cold finger.* As a result, the system was unable to cool to a temperature below 269 K (It was

impossible to repair the cold head in the lab and the latter had to be returned to the Cryomech workshop in the USA for repair. Sending the cold head to Cryomech and receiving back would have taken several months.). A solution needed to be found, and that was to use a liquid nitrogen-cooled open cycle cryostat which was found in the lab as shown in Figure 6.13.
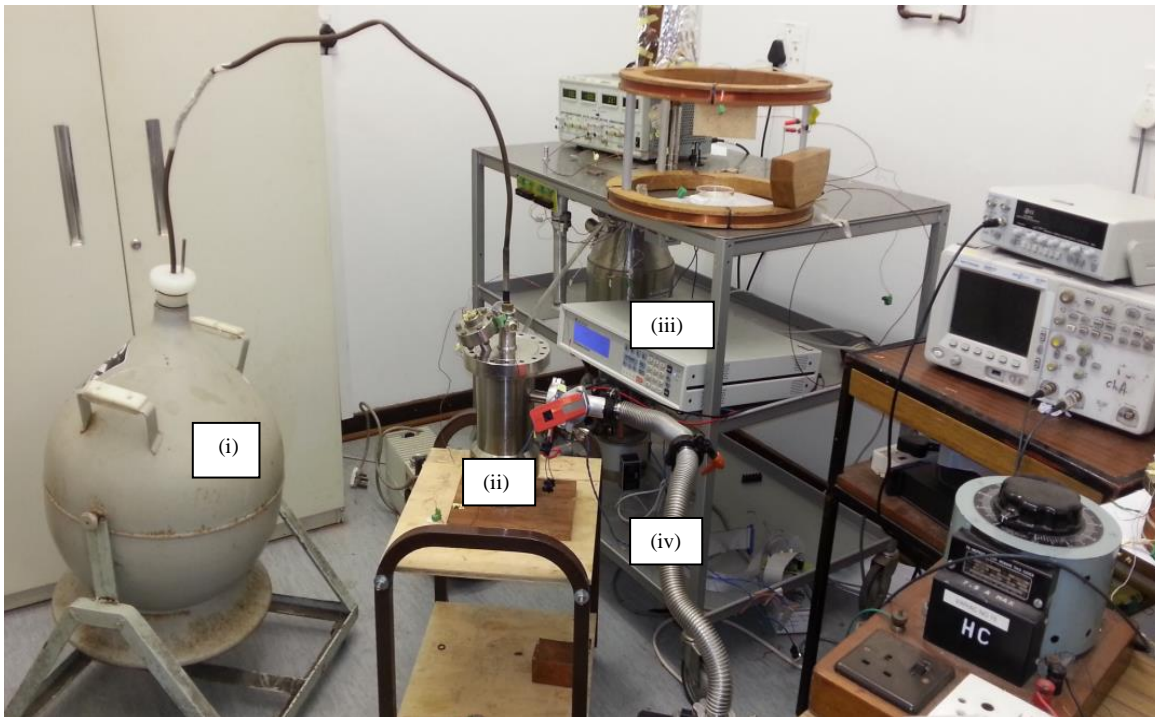
Figure 6.13 Liquid nitrogen cooled cryostat wired for experiment. (i) Liquid nitrogen dewer (ii) Cryostat (iii) Lake Shore 336 temperature controller (iv) Flexible pipe connecting cryostat.

The cryostat was small: 300.0 mm deep and 155.0 mm internal diameter. As a result, it was very difficult to fit the copper stage and the radiation shield inside the 'new' cryostat. This cryostat was inappropriate for resistance and AC susceptibility measurements.

6.4 AC Susceptibility Measurements

6.4.1 Critical Temperature Measurements

AC susceptibility measurements were first used for T_c characterisation of a virgin bulk YBCO sample using the setup shown in Figure 6.14. The specimen experienced an alternating magnetic field of 12.0 μ T produced by the primary coil of the susceptometer. The change in the diamagnetic response of the sample was measured by the secondary coils. The voltage signals at each secondary coil were fed to the inputs of the differential amplifier (whose details are given in Appendix C) which was used for balancing and amplifying the signal from the pick-up coils. The output voltage at the amplifier was then fed to the IOTech Daqbook 2000 card (operated at a reference voltage of ± 0.156V, 2.38 μV resolution) for further processing by the DSP-enhanced lock-in amplifier implemented in DASYLab environment.
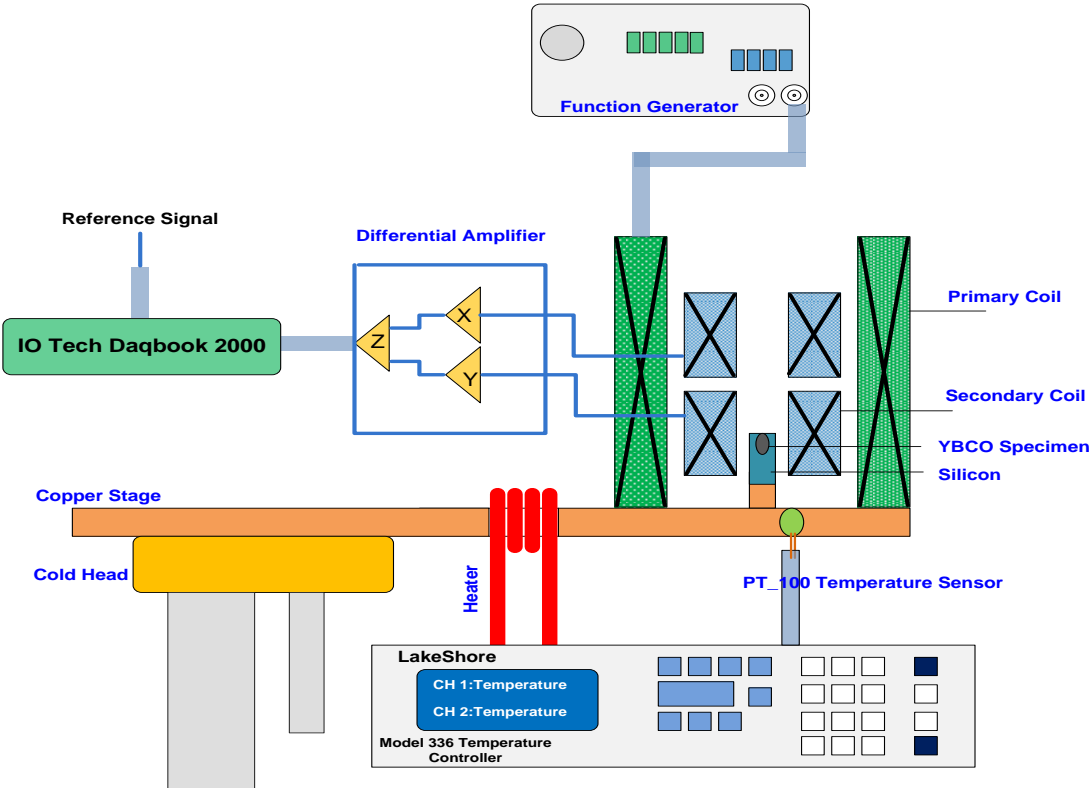

Figure 6. 14 AC Susceptibility experiment setup for T_c characterisation.

The real and the imaginary susceptibilities were measured by the lock-in amplifier and logged every 2 seconds by a function implemented in DASYLab. Simultaneously, the temperature of the sample was synchronously logged using the same technique as for resistive measurements (section 6.3.2.1). Temperature control was achieved using the Lake Shore Model 336 temperature controller which was interfaced using tailor-made software (Appendix B) over the Ethernet for remote temperature logging and control. For T_c characterisation, a cooling rate of 0.2 K/min was used. The slow cooling rate ensured a low temperature gradient between the sample and the PT-100 thermometer. Temperature data was logged synchronously by the Lake Shore Module.

It was not possible to carry out further AC susceptiblity measurements with respect to temperatures as the new close cycle cryocooler that was not fitted to the "belljar" and the small cryostat used as substituition was too small to accomodate the AC susceptometer (designed for "belljar" cryostat). In this regard, the sample and the AC susceptometer were immersed in liquid nitrogen bath at 77.0 K and the magnetic field to which the sample was subjected was varied. The real susceptibility and the imaginary susceptibility were logged with magnetic field.

6.4.2 AC Susceptibility Measurements as a Function of Applied Magnetic Field

The focus was to design and implement a working AC susceptometer that could be used to characterise a superconducting specimen (in this case YBCO). AC susceptibility measurements against magnetic field were done to investigate about the grain couplings of YBCO, which is one of the numerous characteristics that can be investigated with an AC susceptometer.

6.4.2.1 Experimental setup

The susceptometer together with the YBCO specimen were submerged in a liquid nitrogen bath. As shown in Figure 6.15, the YBCO sample was fixed to an aluminium probe using Apiezon thermal grease. Aluminium was selected because it is non-magnetic and the diamagnetic response of the YBCO sample is high compared to the magnetic response of aluminium. The purpose of this setup was to measure the AC susceptibility response of the specimen tested with respect to magnetic field generated at the primary coil. From susceptibility against magnetic field plots, information about the critical current density can be obtained using a modified version of Bean critical state model [22] and information about the grain coupling.
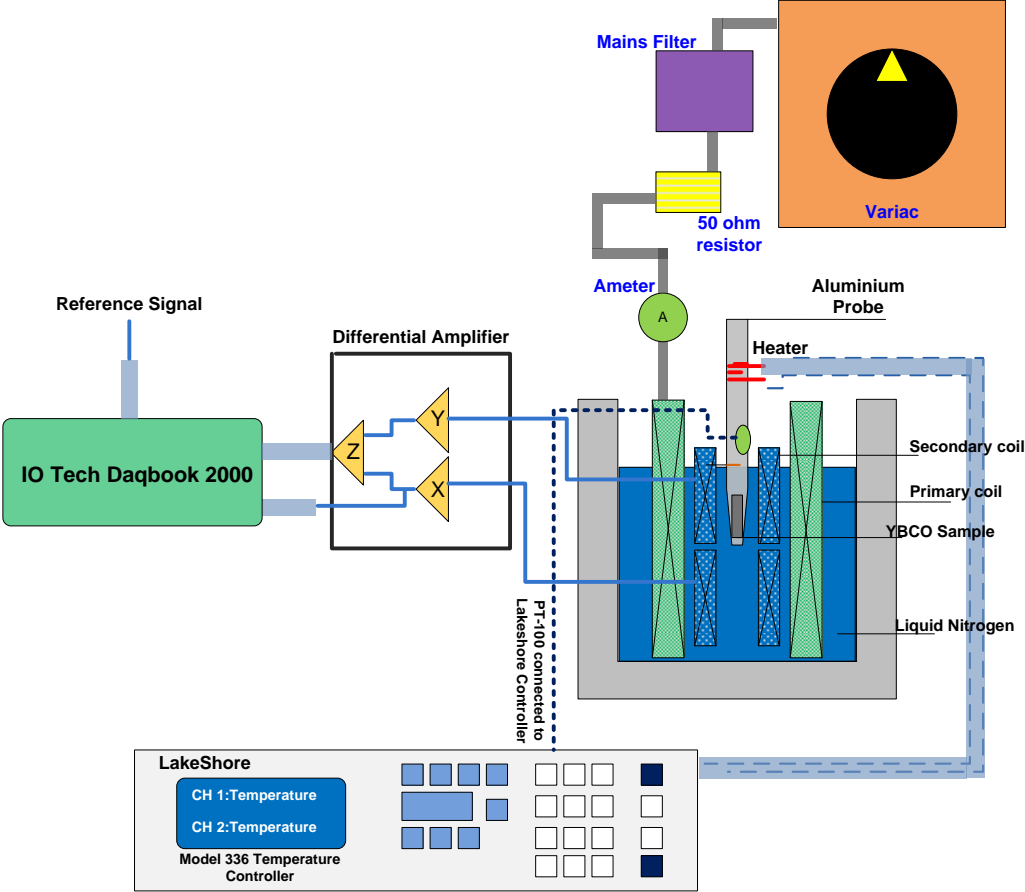

Figure 6. 15 AC Susceptibility setup at constant temperature for J_{ci} characterisation.

The liquid nitrogen bath kept the experiment at a constant temperature of 77.0 K and the magnetic field at the primary coil was varied by altering the current input to the primary coil. To generate the current, a variac together with a mains filter to filter high harmonics, were used. The maximum magnetic field produced was about 20 mT (estimated analytically from the current driving the primary coil generated by the variac). The resolution of the variac was improved by connecting a 50 Ω high power rating resistance in series with the variac and the primary coil as shown in Figure 6.15.

At the time this research was conducted, the material science laboratory was not equipped with hall effect sensors to measure magnetic field. So, an alternative way was developed to measure magnetic field generated at the primary coil. The 'empty' balanced secondary coil was used as a sensor to measure the magnetic field at the primary coil. In fact, even though the values for magnetic field measured were not very accurate, that was not a serious issue as long as the measurements were consistent – initially we were looking for trend changes. The sensor was calibrated at 77.0 K (in liquid nitrogen bath) and its repeatability was accessed (refer to Appendix D for calibration curve). The results were very reliable showing good repeatability. After each experiment, the sensor was recalibrated at 77.0 K. The calibration curves agreed perfectly with each other. No adjustment of the gains of the differential amplifier was required.

Since the magnetic field inside the primary coil changes with position or distance along the coil's interior, the secondary coils were ensured to remain at the same position inside the primary coil for each experiment. The secondary coils were temporarily sealed during experiment to prevent them from moving or vibrating during experiments. If movements or vibrations occurred, this could have corrupted the experiments carried out.

The voltages induced at the secondary coils were fed to the inputs of the differential amplifier for balancing and amplification purposes. The output from the amplifier X (input voltage at the empty secondary coil) and amplifier Z were fed to the IOTech Daqbook 2000 card (operated at a reference voltage of ± 5.0, $76.3\,\mu V$ resolution). The values output at X were processed by DASYLab to measure the magnetic field generated and the values from Z was processed by the software-based lock-in amplifier implemented in DASYLab to measure the real and the imaginary voltage components from which χ' and χ'' values of the sample

could be estimated .

The Lake shore module 336 was used to measure the temperature of the aluminum probe and the liquid nitrogen. It was also used to regulate the temperature during the hydrogen 'annealing' experiment.

6.4.2.2 Annealing Experiment

After each magnetic experiment 'run', the specimen was subjected to 'annealing' experiment under zero magnetic field. The PT-100 thermometer was positioned next to the sample and the nichrome heater was brought closer to the sample. The nitrogen was allowed to evaporate and nitrogen/cold air having a temperature of about 90.0 K existed inside the vessel. The sample was maintained in the cold air/nitrogen vapour and the Lake shore 336 temperature controller was used to regulate the temperature to an 'annealing' temperature above 90.0 K not exceeding 240 K, for not more than 5.0 minutes (details of 'annealing' temperatures and time are given in Chapter 7).

The aim of the 'annealing' experiment was to allow the hydrogen atoms to diffuse to grain boundaries in the samples' lattice with the aim that they might diffuse to places that may relieve stresses in the material's lattice at grain boundaries. The 'annealing' experiment was done under cryogenic temperature above the critical temperature to allow the hydrogen to diffuse slowly in a controlled manner into the material's lattice. Gas such as hydrogen has a high diffusivity and is in motion at any temperature (apart at absolute zero) [70]. The hydrogen experiment was done with the philosophy that the H_2 molecules would be collected at grains boundaries and to relieve the stresses at the dislocations. The 'annealing' experiment was done to identify the correct temperature that would be enough to move mobile H_2 molecules around but once the H_2 molecules are "stuck" at the dislocations, there would be not enough energy to "unstick" them.

6.4.2.3 Experimental procedures

The magnetic field was varied by changing the voltage from the variable AC supply. The magnetic field and the relative AC susceptibility were logged by a computer through DASYLab interfacing. The relative imaginary AC susceptibility were determined from which the grain connections in a sample could be characterised after successive hydrogen doping. The magnetic field was manually increased up to a magnetic field of about 20 mT. This magnetic field was generated by a current of about 0.7 A. Joule heating was minimized since the primary coil was operated under cryogenic conditions. A magnetic field of 20.0 mT was enough to characterize the intergranular coupling of bulk YBCO specimens.

The following summarises the experiment procedure:

1. The AC susceptibility response of the alumium probe without the superconducting specimen (in the nitrogen bath) was logged versus magnetic field by the IO Tech Daqbook 2000 module (an 'empty run').

2. The sample, attached to the aluminium probe placed inside the susceptometer, was submerged into liquid nitrogen as shown in Figure 6.15.

3. The magnetic field at the primary coil was manually varied from the variac making sure to record at least 50 different values of magnetic field well scattered between 0 to 20 mT .

4. The values of AC susceptibility and magnetic field were measured and logged by IO Tech Daqbook 2000 module, interfaced via DASYLab software.

5. 'Annealing' experiment was done under zero field.

6. Steps 2 to 5 were repeated on the same sample but each time the 'annealing' temperature and time were randomly varied.

7. The sample was then removed from the vessel after four 'annealing' runs and allowed to dry before undergoing hydrogenation. The hydrogenated sample was then subjected to steps 2 to 5 again before undergoing the next hydrogenation. Steps 2 to 5 were repeated until the sample stop superconducting.

Chapter 7 Results and Discussions

A dedicated AC susceptometer was designed and built to study high temperature superconducting specimens. The AC susceptometer proves to be a valuable asset to the material science laboratory. At the time that this research was started, the lab had limited experimental facilities. Regarding the characterisation of high temperature superconductors, the lab was fully equipped only for resistance measurements of high-T_c superconductors. Four-wire resistivity tests are time consuming and limited concerning the information that can be obtained about superconducting properties. The possibility of doing AC susceptibility measurements of superconducting samples now exists. The measurements of AC susceptibility have the potential to provide important information about energy losses and the superconducting properties of granular high-T_c materials due to sweeping magnetic field penetrating the intergranular weak link. In particular, the imaginary part of the AC susceptibility can be used to determine the nature of the grains' coupling. Based on AC susceptibility data and a suitable critical state model (like a simple modified version of Bean model), the critical current density can be calculated. Moreover, AC susceptibility was used to determine the onset temperature T_c at which normal to superconducting transition takes place. One experiment for which the AC susceptibility system was used for was a hydrogen doping experiment. YBCO specimens were doped with H_2 in an attempt of improving the grain connections through stress alleviation. Control (virgin sample) and hydrogen-doped specimens were studied by conducting AC susceptibility measurements.

7.1 Grain Morphology

Optical and scanning electron microscopy were used to investigate the morphology of the YBCO specimens. Scanning electron microscopy (SEM) was very helpful in characterising the bulk samples and the images obtained are of superior quality compared with those from optical microscopy. The resolution with SEM is much better and provides the possibility of producing high quality image. However, polarised optical microscopy helps to identify grains and orientation.

7.1.1 SEM Images of Bulk Samples

SEM was performed on an undoped bulk sample of YBCO specimen at different magnification, as shown in Figure 7.1.
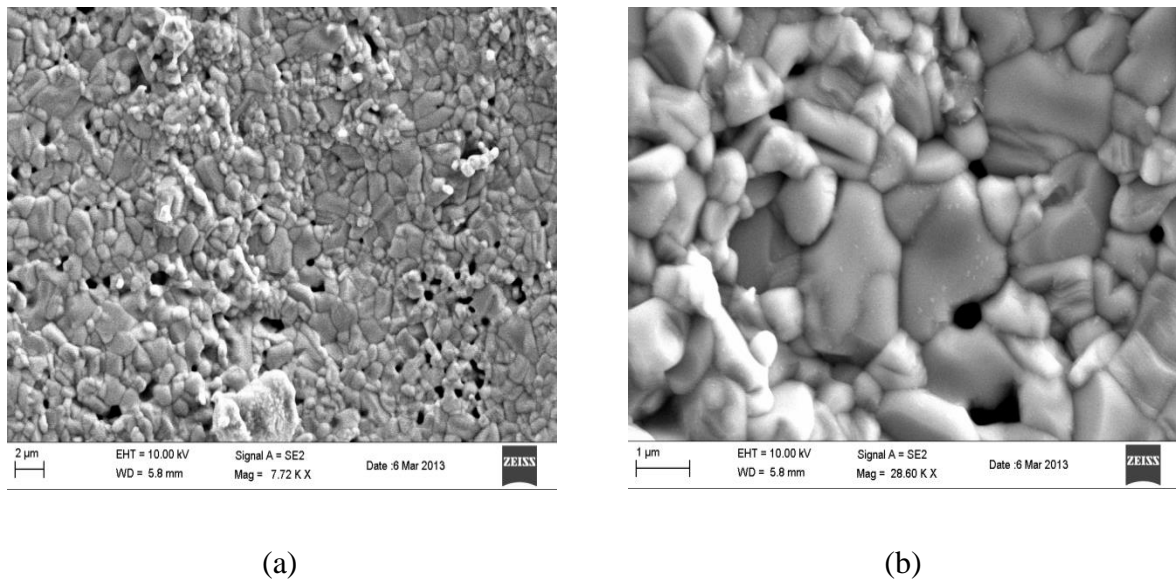
(a)   (b)

Figure 7. 1 SEM characterisation of an undoped bulk YBCO sample. (a) SEM performed at magnification factor of (a) x 7.72 K (b) x 28.6 K.

The granular nature of the YBCO specimen could be observed. The grains and grain boundaries could be distinguished clearly in Figure 7.1 (b). Voids in the material's lattice could be seen as well.

7.2 AC Susceptibility Results

7.2.1 T_c Measurement

First and foremost, AC susceptibility measurements outlined in Section 6.4 were done on a control bulk sample for T_c characterisation. T_c was characterised by drawing a graph of real susceptibility against temperature, where $T_c \approx 91.8\ K$.

Figure 7.2 and Figure 7.3 shows the real and imaginary AC susceptibility response respectively with temperature. The susceptometer used was not calibrated for the scope of this research as we were mainly interested in trend changes. The arbitrary unit was used for AC susceptibility measurements. Figure 7.2 shows a sharp decrease in the real susceptibility, χ'. This indicates that the bulk sample is of good quality where there is one phase of YBCO with a constant oxygen doping. Figure 7.3 shows the response of the imaginary component of the AC susceptibility with temperature. The values of χ'' increased from zero. Then, it reached a maximum value and then decreased again. Positive values of χ'', indicates that the magnetic energy is being converted into heat due to magnetic flux penetrating the intergranular weak links oscillating in and out of the sample. According to Bean's Critical Model [22], a peak in χ'' (T) indicates that the supercurrents have fully penetrated the sample [3][61].

$$H_a = J_{ci\ (T_{peak})}R \tag{7.1}$$

Where H_a is the applied magnetic field, R is the radius of the path of the induced shielding current and $J_{ci\ (T_{peak})}$ is the critical current density (intergranular) at the temperature where the χ'' peak occurred.
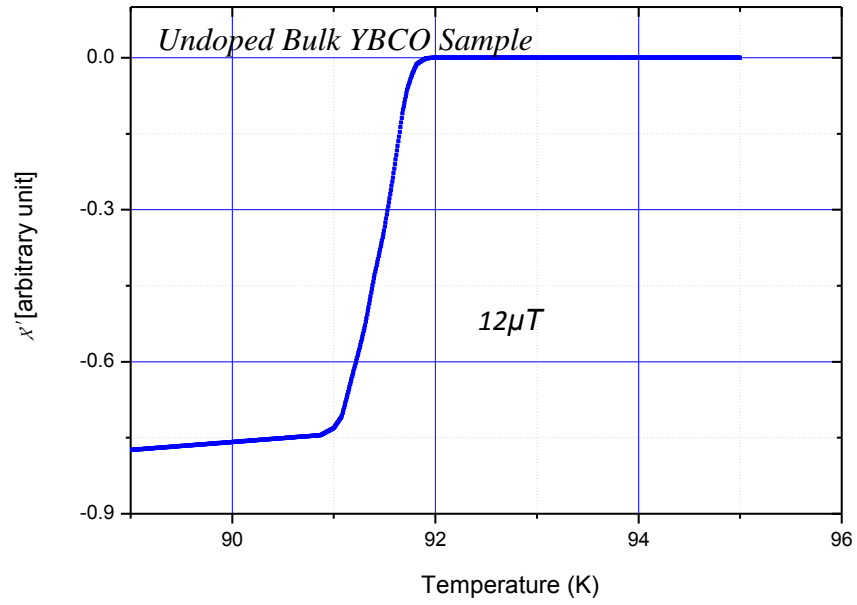
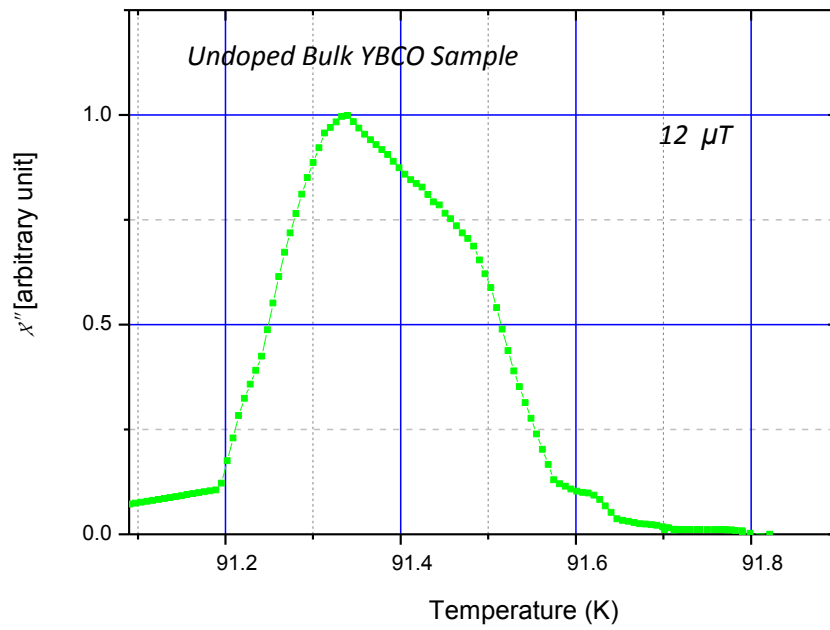Figure 7. 2 Graph of χ' against temperature for bulk YBCO sample.

Figure 7. 3 Graph of χ'' against temperature for bulk YBCO sample.

111

7.2.2 AC susceptibility as a Function of Magnetic Field

Complex AC susceptibility measurements were done with respect to a variable oscillating magnetic field at 50 Hz (sinusoidal in nature) at a constant temperature (77.0 K). Much emphasis was laid on χ''. Using the simplest critical state model of Bean (a modified version), where J_c is independent of the magnetic field [22]. The critical current, J_c is related to B_p, which is the penetration magnetic flux density, by Equation 7.2 [61]. x is the distance perpendicular to the field.

$$B_p = \mu_o J_c \, x. \tag{7.2}$$

Similarly, this relation (Equation 7.2) can be adapted to describe the intergranular critical current circulating through the intergranular matrix of the superconductor:

$$B_{pi}^* = \mu_o J_{ci} \, \frac{D}{2}. \tag{7.3}$$

B_{pi}^* is the value of the magnetic field at which the peak in χ'' occurs, J_{ci} is the intergranular critical current density, D is the width of the sample.

The peak in χ'' appears at full penetration field , B_{pi}^* [61], at which the supercurrent just reaches the centre.

Equation 7.3 could be used to estimate the intergranular current density through the matrix of the ceramic YBCO sample. Hence, the nature of the strength of the grain boundaries can be deduced from the value of the intergranular critical current density.

Complex AC susceptibility measurements of the original YBCO sample and hydrogen doped samples (at different H_2 concentration) against magnetic field were done at a constant temperature of 77.0 K (sample immersed into liquid nitrogen). The relevant values of χ'' were plotted against magnetic field.

The normalized plots of the measured values of the imaginary part of the AC susceptibility (χ'') against the applied magnetic field (B) for the control sample (original undoped sample) and the hydrogen-doped specimens are shown in Figures 7.4 and 7.6 to 7.13. In each case, the applied magnetic field is normalised to the value of B_{max}, the field at which maximum

112

value in χ'' occurs before "annealing" was carried out for the control sample (original sample). Similarly, the value of χ'' is normalised to the maximum value of the imaginary AC susceptibility (χ''_{max}).

The signal at the pickup coil was a summation of the Ac susceptibility response of the superconducting specimen and the response of the aluminium sample holder. To eliminate the magnetic response of aluminium (mainly due to eddy current), an 'empty run' was performed, an experiment with no superconducting specimen present at the secondary coils, to record a reference curve.
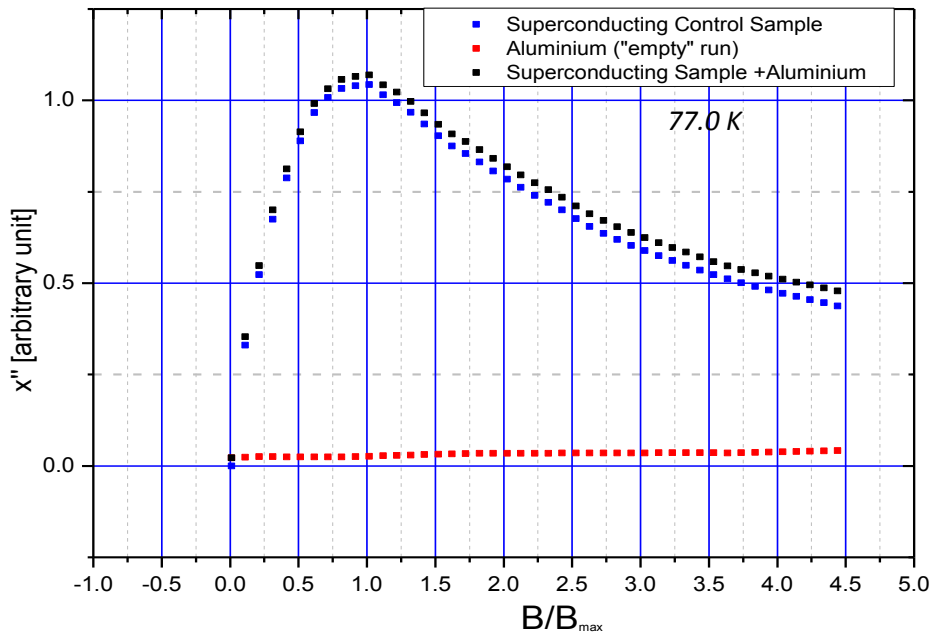

Figure 7. 4 χ'' component of AC susceptibility reference curve of aluminium (in red), χ'' component of AC susceptibility curve of aluminium and superconducting specimen (in black) and χ'' component of AC susceptibility curve of superconducting specimen only (in blue).

The χ'' curve for the superconducting specimen is obtained after substraction of the reference curve from the χ'' curve due to the magnetic response of aluminium and superconducting specimen. The other χ'' curves (Figure 7.6 to Figure 7.12) were obtained after subtracting the magnetic response of aluminium (obtained from the "empty run" experiment). Figure 7.6 shows the real susceptibility response of the control sample with magnetic field. As the magnitude of the magnetic field increases the real susceptibility χ' increases (becomes less

negative), showing a decrease in the strength of the superconducting connections between the grains.
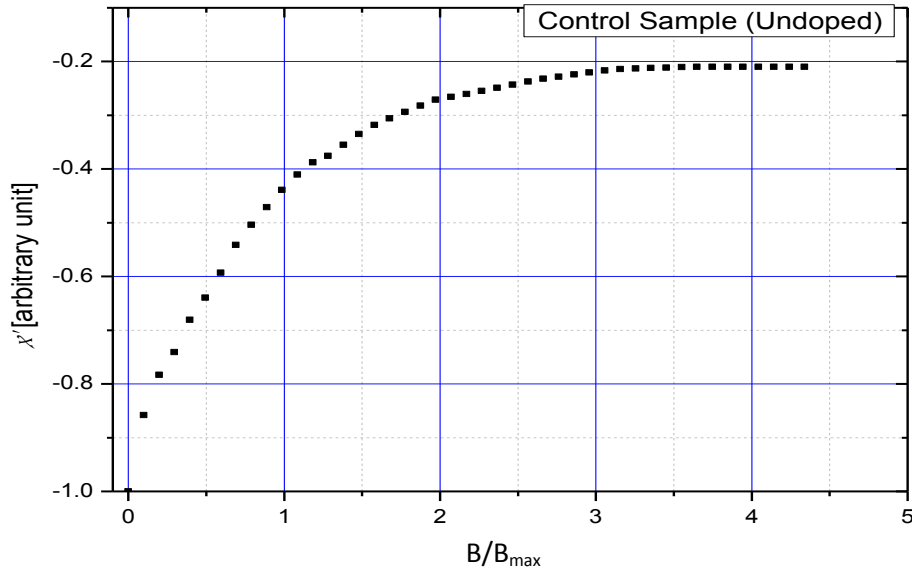

Figure 7. 5 χ' component of AC susceptibility for the Control sample (undoped YBCO specimen) after subtracting the magnetic response of aluminium.

The method of subtraction of the reference curve is not perfect and it was expected that there were undesired effects in the AC susceptibility curves plotted. So far, the results obtained prove to be satisfactory as the curves show good repeatability and distinct peaks can be identified from each graph plotted as shown in Figure 7.6 to Figure 7.13. The main focus was to detect any shift in the χ'' peaks which provides us with valuable information about the grain couplings.

The graphs shown in Figures 7.6 to 7.12 were plotted to determine if the 'annealing' experiments resulted in an effect causing a right or left shift in the position of the peaks and/ or a change in the magnitude of the peaks with respect to the magnetic characteristics before annealing. Here 'annealing' was a term used to indicate a shifting and collecting of mobile hydrogen in the YBCO specimen. It was thought that the hydrogen would migrate to dislocation sites and remain trapped and relieve stress fields associated with the dislocations. Each experiment comprised an 'annealing' temperature, duration and then a quenching to 77.0K.

Figure 7.6 χ''/χ''_{max} against B/B$_{max}$ plots. Annealing_1 was done at 120 K for 3.0 minutes; Annealing_2 was done at 150 K for 3.0 minutes; Annealing_3 was done at 240 K for 3.0 minutes.

Figure 7.7 χ''/χ'_{max} against B/B$_{max}$ Plots. Annealing_1 was done at 120 K for 3.0 minutes; Annealing_2 was done at 155 K for 3.0 minutes; Annealing_3 was done at 240 K for 3.5 minutes.

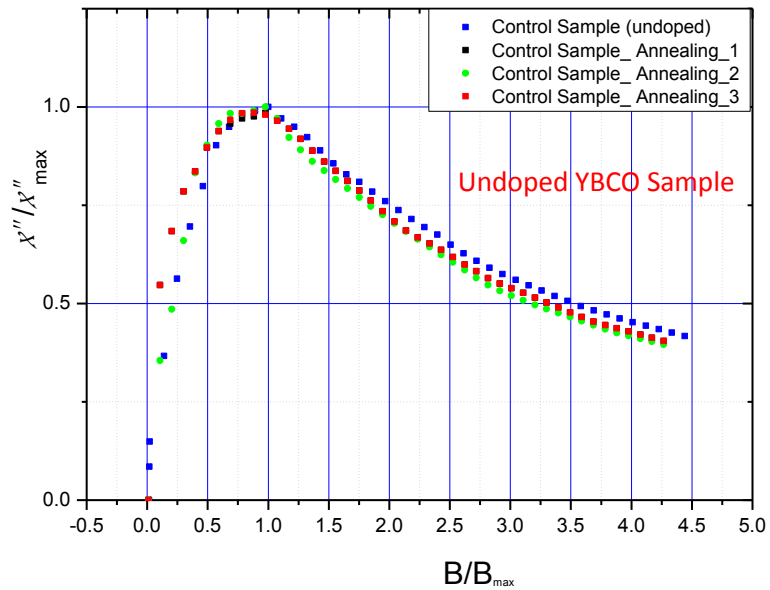Figure 7.8 χ''/χ''_{max} against B/B$_{max}$ plots. Annealing_1 was done at 120 K for 4.0 minutes; Annealing_2 was done at 155 K for 3.0 minutes; Annealing_3 was done at 200 K for 2.5 minutes.

Figure 7.9 χ''/χ''_{max} against B/B$_{max}$ plots. Annealing_1 was done at 120 K for 3.0 minutes; Annealing_2 was done at 155 K for 2.5 minutes.

Figure 7.10 χ''/χ''_{max} against B/B_{max} plots. Annealing_1 was done at 120 K for 5.0 minutes; Annealing_2 was done at 155 K for 3 minutes; Annealing_3 was done at 200K for 2 minutes.
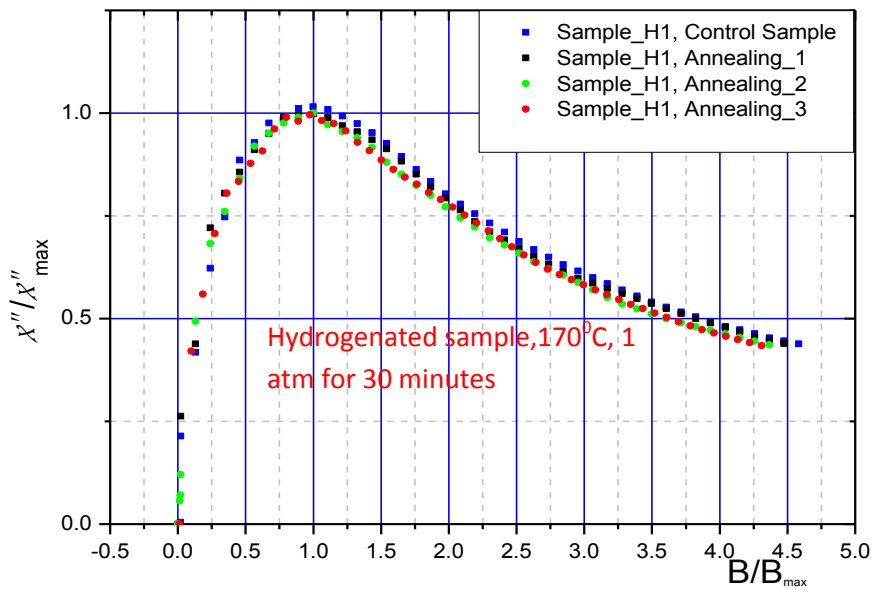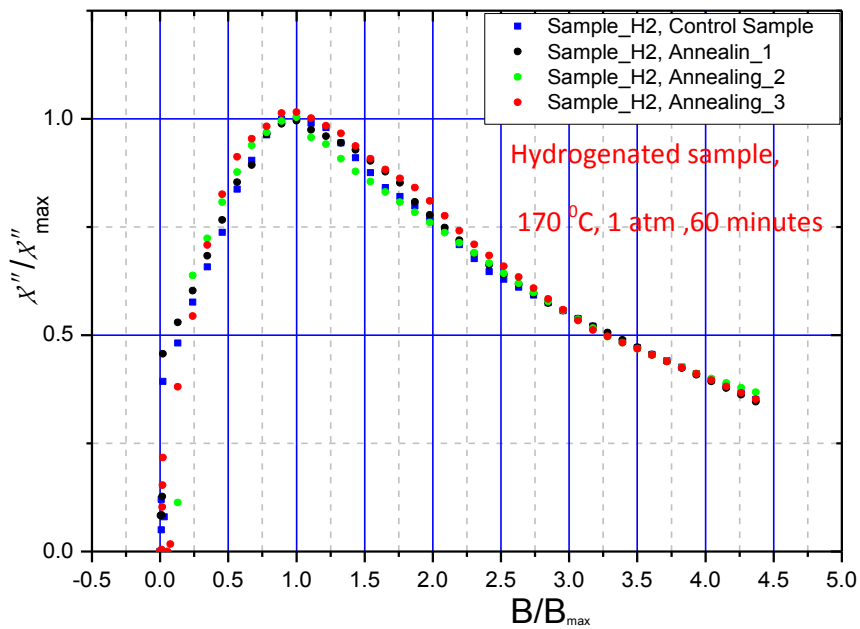

Figure 7.11 χ''/χ''_{max} against B/B_{max}. Annealing_1 was done at 120 K for 4.0 minutes; Annealing_2 was done at 155 K for 3.5 minutes; Annealing_3 was done at 200 K for 4.5 minutes.
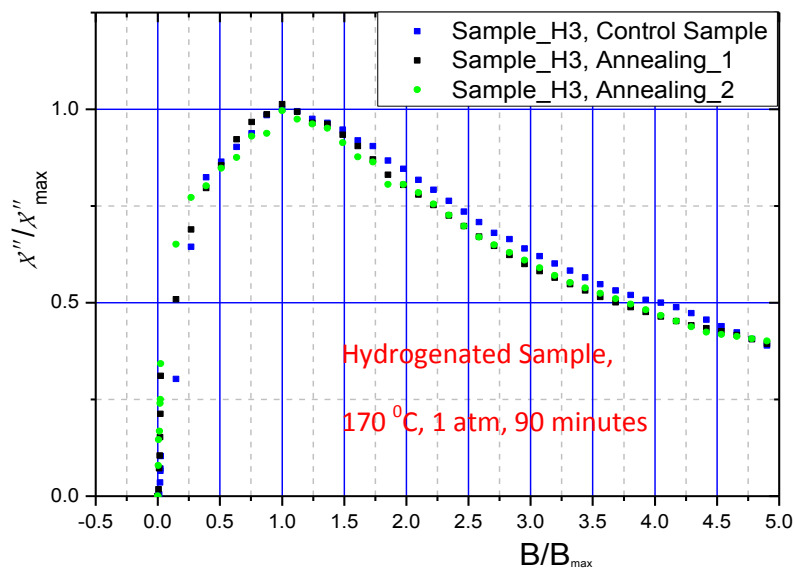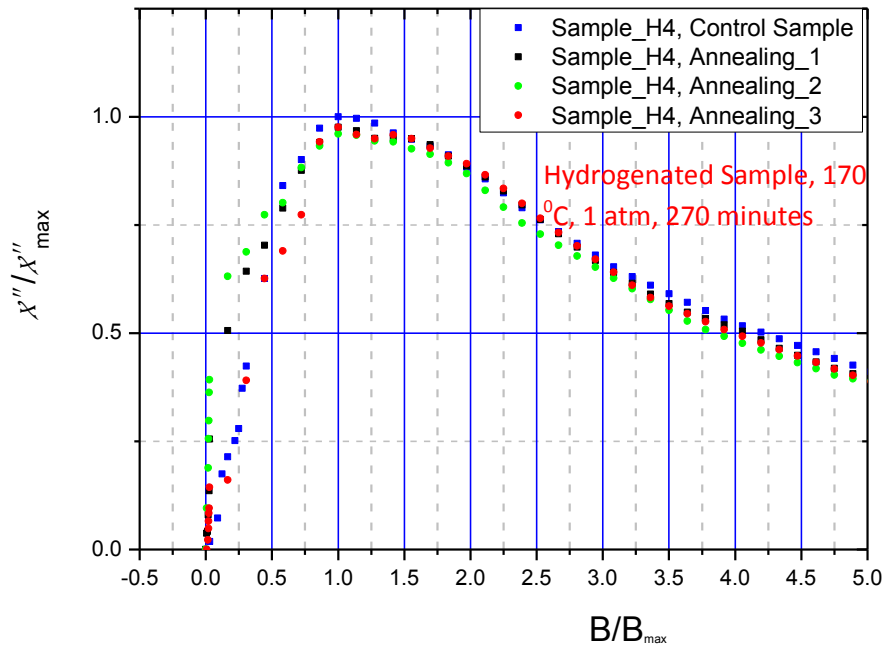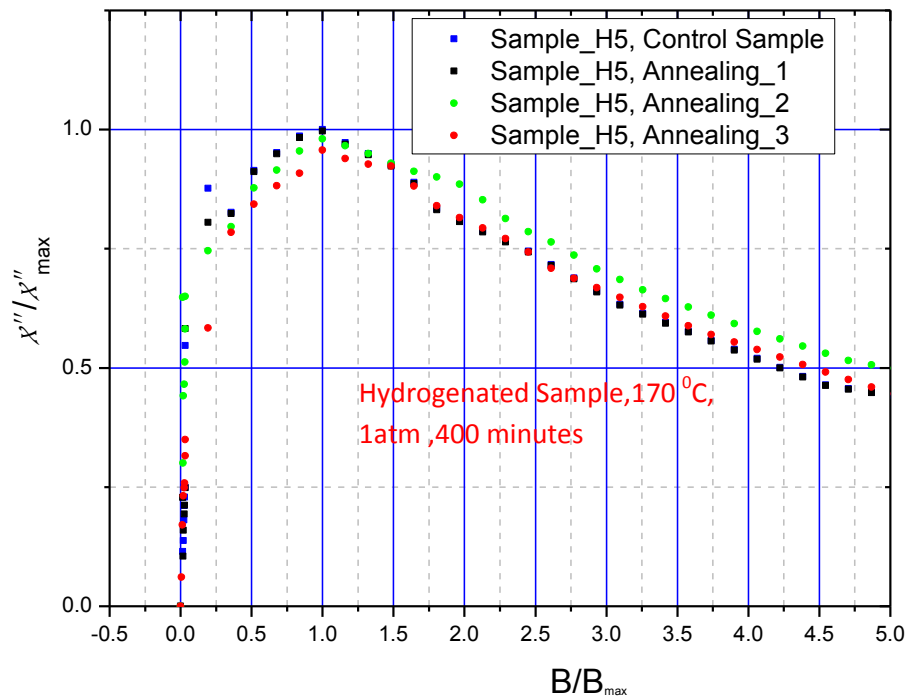
The magnetic field was varied manually using a variac. One of the limitation of the variac is the magnetic field cannot be varied with good precision between 0 to 0.5 (relative magnetic field values). This explains why the variation of values χ'' is not smooth on the graph. After a relative field of 0.5, fairly good precision and resolution could be obtained using the variac.

It can be deduced that the 'annealing' experiments did not cause any shift in the peaks. Different annealing scenarios were opted (by varying the temperature and the time) but the results remained merely the same. In conclusion, no measurable effects were noticed .i.e., no support for the hypothesis of stress relief due to the collection of hydrogen at the grain boundaries in the matrix of the ceramic YBCO superconducting specimen occurred. The curves for each specimen are similar except some minor differences in some situations. This might be attributed to higher harmonics signals generated in the pick-up signal due the noisy signal output (sinusoidal with higher harmonics) from the variac. Though a main's filter was used to remove higher order harmonics and the lock-in amplifier filtered the signal before separating the real from the imaginary components, significant variation in noise voltages from the mains might explain the fluctuation in the curves plotted for a particular specimen.

The data collected for the undoped and hydrogenated specimen (before and after "annealing" , shown in Figure 7.6 to Figure 7.12) were processed to produce average curves (shown in Figure 7.12). The curves were normalised. The applied magnetic field is normalised to the value of B_{max}, the field at which maximum value in χ'' occurs for the control sample (undoped original sample). The value of χ'' is normalised to the maximum value of χ'' for the control sample. The method of subtracting the magnetic response of aluminium and producing average curves is not perfect and this might have resulted in some undesired outcomes. However, the peaks formed can clearly be distinguished for all the graphs plotted. The peak is reached when the intergrain currents come to a value allowing the alternating magnetic field to penetrate fully through the intergranular space reaching the sample's centre. At B_{pi}^*, at which the peak χ'' occurs, the AC field occupies the whole intergranular space in the sample.

The average curves were plotted on the same graph such that any shift in the peaks associated with hydrogen doping could be identified.
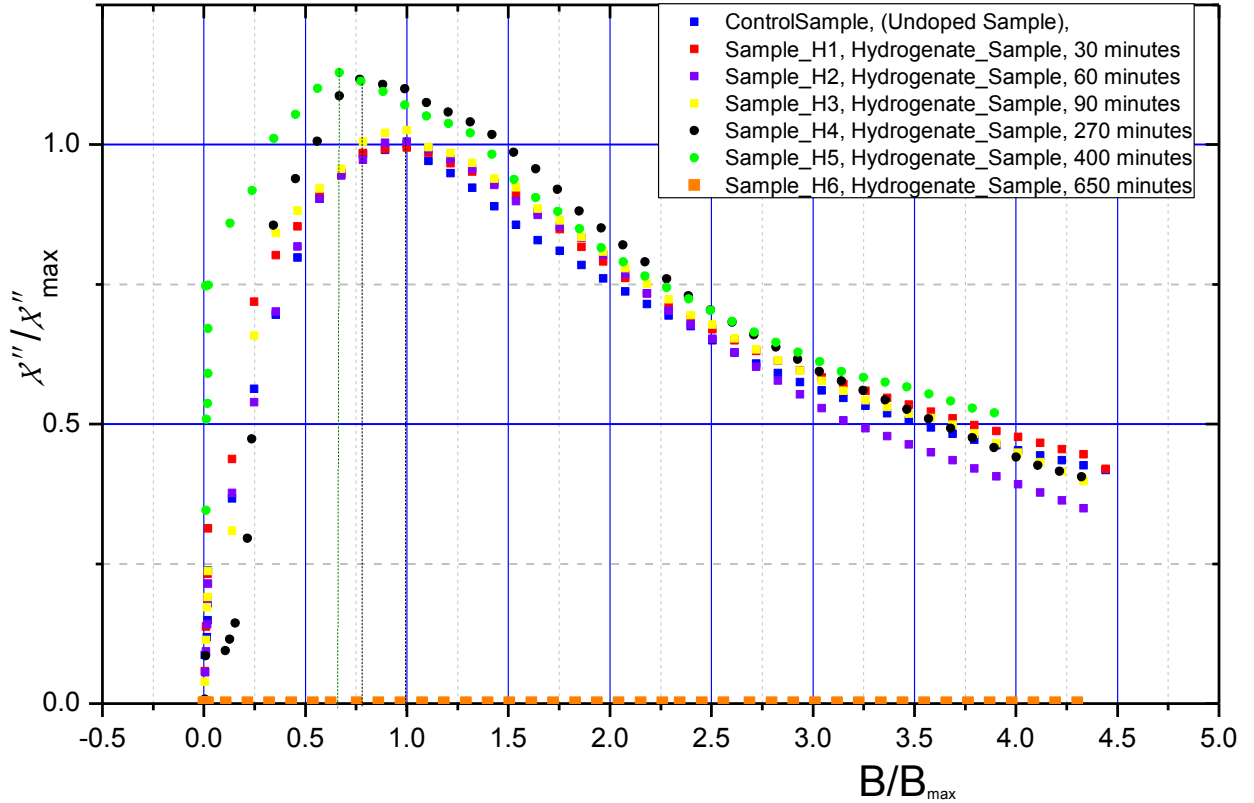

Figure 7. 12 χ''/ χ''_{max} as a function of B/B_{max} for trends comparison with the original undoped sample as the control sample.

The curve for the undoped sample and the curves after the 30 minutes doping, 60 minutes doping and 90 minutes doping cycles are almost similar except insignificant variation in the maximum value of χ'' reached. However, the peak values of χ'' occured at the same magnetic field. According to the simple modified version of Bean critical model (Equation 7.3), the intergranular critical current remained unchanged as there is no right or left shift in the peaks of the curves. This was attributed to the fact that the hydrogen concentration in the sample's lattice was too small to influence the material's properties.

After 270 minutes of H_2 doping cycle, the curve shifted towards the left and there was an increase in the peak value of χ'' (with respect to the original sample). An increase in the peak of χ'' indicates that more energy is being dissipated in the form of heat as the oscillating magnetic

field penetrated the intergranular weak links [2] [34] [61]. From Equation 7.3, it can be deduced that the intergranular critical current decreases as the curves shift towards the left. So, both a decrease in the value of the full penetration magnetic field and an increase in the peak value of χ'' indicate that the weak-link superconducting networks between the grains are being disconnected/ weakened.

After 400 minutes of reaction with hydrogen, the curve shifted further to the left and an increase in the relative magnitude of χ'' was noted. This indicates a further weakening of the intergranular Josephson coupling as more hydrogen was absorbed. After 650 minutes of H_2 doping cycle, no diamagnetic response was detected and hence no superconductivity state. This was attributed to the fact that the high concentration of H_2 molecules in the YBCO's lattice causes a change in the stoichiometry of the material. Hence, the hydrogenated sample lost its superconducting characteristics.

Figure 7. 13 J_{ci} against Hydrogenation
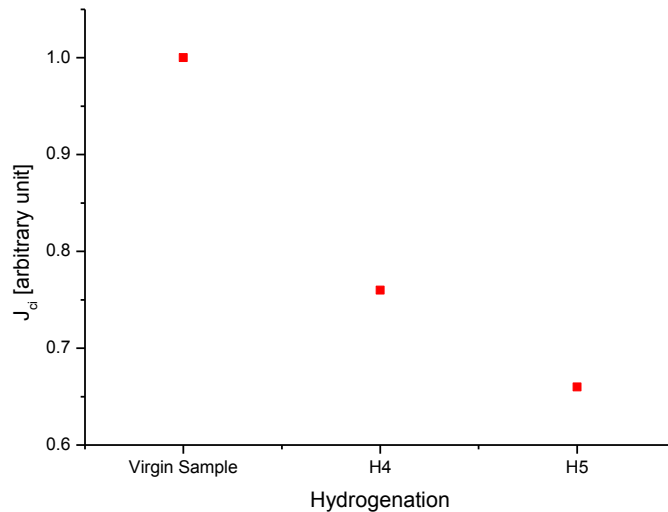
From Equation 7.3, the relative intergranular critical current density J_{ci} was estimated (with respect to the virgin sample).   H4 is the sample being hydrogenated for 270 minutes, H5 is the sample after 400 minutes of hydrogenation. As the amount of time for which the sample is being hydrogenated increases, the critical current density decreases as shown in Figure 7.13.

Chapter 8 Conclusion and Further Work

8.1 Summary

The research goal was to design and implement an AC susceptibility measurement system to characterize granular YBCO specimens, with a particular focus on the study of the grains coupling of the specimens and 'qualitative' trend changes.

An DSP-enhanced AC susceptometer was successfully designed and implemented to characterise polycrystalline YBCO sample. The susceptometer built has a calibration coefficient α' of $14.8\,A\,m^2V^{-1}s^{-1}$ and the present apparatus' sensitivity is $11.6\,\mu V$ (at $\chi' = 0.1$). The magnetic experimental signals from the bulk samples were large enough to be detected by the IOTech 2000 data-acquisition system. A differential amplifier successfully removed the offset voltage at the secondary coils and amplified the experimental signal in case the signal is less than the DaqBook's resolution. The IOTech 2000 Daqbook module has its limitations. It has a low sampling frequency of 25 KHz and a mediocre resolution of $2.38\,\mu V$. If the signal's frequency was of the order of KHz, the resolution of the samples would have been low causing a shift in the value of T_c. To counteract this drawback, the magnetisation signal was limited to a frequency of 100 Hz. Despite the limitations of the IOTech 2000 Daqbook module, the DSP-enhanced lock-in amplifier constructed in DASYLab environment, satisfactorily measured the fundamental amplitudes of the in-phase and the out-of-phase components of the magnetic signal, from which relative values of χ' and χ'' could be estimated, due to the diamagnetic response of the sample placed in the susceptometer. Clear transition in χ' was observed from the results of AC susceptibility tests at low field in determining T_c of an undoped polycrystalline specimen. The values of χ'' varied with temperature to reach a maximum value

during the phase transition of the YBCO sample, indicating power loss during the transition due to magnetic field penetrating the intergranular weak link space. Next to AC susceptibility, resistive testing was successfully done on control bulk YBCO specimen. To perform resistive experiment in the establishment of the critical temperature, good contacts were achieved with silver paste and silver wire. AC susceptibility and resistive tests were not performed on hydrogen doped specimens for critical temperature determination due to equipment limitation, unavailability of cryostat (which broke down).

The AC susceptometer was constructed with an explicit focus to investigate about the grains' coupling in YBCO specimens. The magnetic response of polycrystalline YBCO samples was effectively measured with respect to magnetic field at 77.0 K (AC susceptometer submerged in liquid nitrogen). The relative intergranular critical currents for control and hydrogen-doped YBCO were successfully estimated from the magnetic measurements using simple critical state model, Bean model. Hydrogenation was found to substantially suppress intergranular critical current density. This is due to the weakening of the Josephson couplings between the grains, complying with the literature reviews. Hydrogen molecules failed to relieve the stresses at the grain boundaries according to our prediction with no evidence of Cottrell atmosphere formation.

Overall, the AC susceptometer effectively characterised the bulk YBCO samples: measuring T_c and relative intergranular critical current J_{ci}.

8.2 Further Work

The susceptometer built has some limitations. There is scope for development. It suits the purpose to establish T_c of bulk specimen and to study the grain boundaries in polycrystalline superconducting systems by the determination of intergranular critical current density J_{ci}. However, it needs to be calibrated, to correct for the demagnetization fields, for exact determination of χ' and χ''. Substitution of the actual data-acquisition system by one with a sampling frequency higher than 25 KHz and if the resolution is nanovolts, then improvement in the performance of the AC susceptibility measurement system is expected. The variac which outputs a noisy signal needs to be replaced by a high power AC supply capable of producing pure sinusoidal voltage signal that varies over a range of frequency (from 0 to 10 KHz for instance). With this type of power supply, a better signal to noise ratio is expected at the pick-up coil, from which more accurate magnetization readings will be extracted by the lock-in amplifier. Instead of doping with hydrogen to relieve stresses at grain boundaries, the effect of other dopants, such as calcium, etc., could be explored, knowing that Ca improves grain coupling [35][36].

References:

1. J. Archer, "Investigation Into The Synthesis and Carbon Doping of MgB2 for Possible Bulk Superconducting Fault Current Limiter", M.S Dissertation., Elec Eng., UKZN., Durban., South Africa, 2012.

2. M.I. Youssif, A. A. Bahgat and I. A. Ali, " AC Magnetic Susceptibility Technique for the Characterisation of High Temperature Superconductors" , *Egypt J. Sol*, vol. 23 no. 2, pp. 232-250 , 2000.

3. Laurent, J F Fagnard and B Vanderheyden, ''An AC Susceptometer for the Characterisation of Large, Bulk Superconducting Samples'' *Measurement Science and Technology*, *IOP Publishing*, vol. 19, pp. 1-10, July 2008.

4. Fedor Gomory, "Characterisation of high-temperature superconductors by AC susceptibility measurements", *Supercond. Sci. Technol*. vol. 10, pp. 523-542, May 1997.

5. ALL. Jarvis, "An Investigation of the Influence of Silver Doping on the Intergranular 'weak-link' Properties of the Superconducting System $Y_1Ba_2Cu_3O_{7-x}$", PH.D. dissertation, Elec Eng., UKZN., Durban., South Africa, 2012.

6. M.Nicolas et al., "Effect of Hydrogen on High T_c Granular Superconductors, Observation of percolating Behaviour ", *Solid State Communication* , vol. 66, No 11, pp 1157-1160, 1988.

7. Hitoshi Sakai, Yoshimi Ohzawa, "Effect of Internal Stress in BSCCO/ silver plate on critical current density", *Advances in Superconductivity*, no.4, pp.591-594, 1992.

8. D. Agassi, C. S. Pande, and R. A. Masumura, "Superconductor superlattice model for small angle grain boundaries in Y-Ba-Cu-O", *Physical Review B*, vol.52, p.16237, December 1995.

9. H.Kamerlingh Onnes, "Further experiments with liquid helium: the resistance of pure mercury at helium temperature*", Commun Phys*. Letter no. 120 b, April 1911.

10. Gian Franco Vidali, *Superconductivity The Next Revolution*: University of Cambridge Press, 1993.

11. F. London and H. London, "The Electromagnetic Equations of the Supraconductor". *Proceeding of the royal society of London-* Series A*, Mathematical and Physical sciences*, vol. 149, no.866, pp. 71-88, March 1935.

12. J. Bardeen, L.N Cooper and J.R Schrieffer, "Microscopic theory of superconductivity". *Physical review*, vol.106, no1, pp. 162-164, April 1957.

13. Stephen Blundell, *Superconductivity, a very short introduction:* Oxford press, 2009.

14. Alexei A Abrikosov, "On the Magnetic Properties of Superconductors of the Second Type," *Soviet Physics JETP*, vol. 5, no. 6, pp. 1174-1182, December 1957

15. B. D. Josephson, "Possible new effects in superconductive tunnelling," *Physics Letters*, vol. 1, no. 7, pp. 251-253, July 1962.

16. J. G. Bednorz and K. A. Müller, "Possible high T_c superconductivity in the Ba−La−Cu−O system," *Zeitschrift für Physik B Condensed Matter*, vol. 64, no. 2, pp. 189-193, June 1986.

17. J. W. Gibbs, "A method of geometrical representation of the thermodynamic properties of substances by means of surfaces," *Transactions of the Connecticut Academy of Arts and Sciences*, vol. 2, pp. 382-404, December 1873.

18. L. Landau, "Theory of phase transformations. I," *Sov. Phys. JETP*, vol. 7, p. 19, 1937.

19. L. Landau, "Theory of phase transformations. II," *Sov. Phys. JETP*, vol. 7, p. 627, 1937.

20. V. L. Ginzburg and L. Landau, "On the theory of superconductivity," *Zh. Eksp. Teor. Fiz.*, vol. 20, p. 1064, 1950.

21. Charles P.Bean, "Magnetisation of Hard Superconductors", *Physical Review Letters*, vol. 8, pp 250-253, 1962.

22. Charles P. Bean, "Magnetisation of High Field Superconductors", *in Review of Modern Physics*, vol. 36, pp 31-39, 1964.

23. Y. B. Kim, C. F. Hempstead, and A. R. Strnad, "Magnetization and Critical Supercurrents," *Physical Review*, vol. 129, no. 2, pp. 528-535, January 1963.

24. R.M. Hazen et al, "Crystallographic description of phases in the Y-Ba-Cu-O superconductor", *Phys. Rev. B,* vol. 35, p. 7238 ,1987.

25. M. K. Wu et al., "Superconductivity at 93 K in a new mixed-phase Y-Ba-Cu-O compound system at ambient pressure," *Physical Review Letters*, vol. 58, pp. 908-910, March 1987.

26. Ajay Kumar, Saxena "Crystal Structure of High Temperature Superconductors" in *High Temperature Superconductors*, Berlin, Germany: Springer, 2009, Ch.2, p. 43.

27. Ajay Kumar, Saxena "Crystal Structure of High Temperature Superconductors" in *High Temperature Superconductors*, Berlin, Germany: Springer, 2009, Ch. 2, p. 45.

28. F.B Silbee, "A note on electrical conduction in metals at low temperatures" *Journal of Washington Academy of science,* no. 6, pp. 597-602, 1916.

29. D.C Van der Laan, T.J Haugan and P.N. Barnes "Effect of a Compressive Uniaxial Strain on the Critical Current Density of Grain Boundaries in Superconducting $YBa_2Cu_3O_{7-\delta}$ Films" .*Phys.Rev. Lett,* no.103, p.27005, July 2009.

30. D. Dimos et al.,"Orientation Dependence of Grain-Boundary Critical Current in $Y_1Ba_2Cu_3O_{7-\delta}$ Bi-Crystals" *Phys. Rev. Letters* 61, p. 219 , July 1988.

31. S.J Pennycook et al., " The Relationship Between Grain Boundary Structure and Current Transport in High-Tc Superconductors" *in Studies of High Temperatures superconductors-II* , Newyork: Nova science,1999, Ch. 6 , pp. 145-172.

32. S.A Kukushkin, I.A. Ovid'ko and A.V. Osipov, "Critical Current in High Temperature Superconductors with Disordered Tilt Grain Boundaries*", Technical Phyiscs Letters*, vol. 26 , no.7 , pp 609-611. February 2000.

33. A. Gurevich and E.A. Pashitskii, " Current Transport through low-angle grain boundaries in high-temperature superconductors", *Physical review B*, vol.57, no. 21, June 1998.

34. W.Ye, T. Takabatake a, T.Ekino and H. Fujii, *"Effect of Hydrogenation on $YBa_2Cu_3O_{6.9}$ and $Sr_2CaCu_2O_{8.2}$ Superconductors" ,Physica B*, vol.194-196, pp.1941-1942, 1994

35. A. Berenov and al. "Ca Doping of YBCO Grain Boundaries" *Physica C*, vol. 372-376, pp.1059-1062, August 2002.

36. X.Song et al., "Electromagnetic , Atomic Structure and Chemistry Changes Induced by Ca Doping of $YBa_2Cu_3O_7$ Low Angle Grain Boundaries", *Nature Materials*, vol. 4, pp.470-475, 2005.

37. D. Dew-Hughes, "The Critical Current of the Superconductors: an Historical Review", *Low Temperature Physics*, vol. 27, no.9-10, pp. 713-722 ,October 2001.

38. R. F. Klie et al., "Enhanced current transport at grain boundaries in high-T_c superconductors", *Nature*, vol. 435, pp. 475-478, May 2005.

39. M. F. Chisholm and S. J. Pennycook, "Structural Origin of Reduced Critical Currents at $YBa_2Cu_3O_{7-d}$ Grain Boundaries", *Nature*, vol. 351, pp. 47-49, May 1991.

40. J.Mannhart and C.C Tsuei, "Limits of critical current density of polycrystalline high-temperature superconductors based on the current transport properties of single grain boundaries", *Condensed Matter*, vol. 77, pp. 53-59, April 1989.

41. Jibin Shi, " Predictive Microstructural Modeling of Grain-boundary Interactions and their Effect on Overall Crystal Behaviour", Ph.D. dissertation, North Carolina University, Chapel Hill, USA, February 2009.

42. A.H Cottrell and B.A Bilby,"Dislocation Theory and Strain Ageing of Iron*", Proceeding and the Physical Society*, London , vol. 62, Issue 1, pp.49-62 , 1948

43. Douthwaite RM, Evans JT, "Interaction between a tetragonal distortion and a 〈111〉 screw dislocation in an anisotropic cubic crystal", *Scripta Metall*, vol. 7, p.1019, October 1973.

44. E.Clouet "Dislocation Interaction with C in Alpha-Fe: a comparison between atomic simulation and elastic theory", *Condensed Matter Science* , pp 1-18, July 2006

45. R.Bullough and R.C. Newman, "The Kinetic of Migration of point Defects towards Dislocations*, Rep. Prog. Phys*, vol. 33, pp. 101-148, 1970.

46. Martin Nikolo, *"Superconductivity: A guide to alternating current susceptibility measurements and alternating current susceptometer design", Am. J. Phys*, vol. 63 (1), pp. 57- 65,June 1994.

47. S.Ramakrishan et al., "An AC susceptometer from 1.5 K to 300 K", *Journal of Physics E: Sci inst*, vol.18, no.8, pp. 650, 1985.

48. Coach M and Khoder A.F *"AC susceptibility responses of Superconductors: cryogenic aspects, investigation of inhomogeneous systems and the equilibrium mixed state"* in *Magnetic Susceptibility of Superconductors and other Spin System*, RA. Hein Ed, Newyork: Plenum Press, pp. 25-48, 1991.

49. B.W. Kuipers et al., "Complex Magnetic Susceptibility Setup for Spectroscopy in Extremely low-frequency range" *AIP Review of Scientific Instruments,* vol. 79, p. 1391, January 2008.

50. .P.H Kes *et al*., "Thermally assisted flux flow at small driving force" *Supercond. Sci Techno*, vol. 1, p. 242, February1989.

51. Clem J R, "Granular and superconducting-glass properties of the high-temperature superconductors*", Physica C*, vol. 153-155, pp. 50-55, June 1988.

52. A. Bajpai and A. Benerjee, "An automated susceptometer for the measurement of linear and nonlinear magnetic ac susceptibility*", Rev.Sci. Instrum,* vol. 68, p. 4075, June 1997.

53. C.P Bidinosti and W.N Hardy, "High precision ac susceptometer for measuring the temperature and magnetic field dependence of the penetration depth in superconductor single crystals*", Rev. Sci. Instrum*, vol.71, p. 3816, July 2000.

54. T. Dumelow *et al.* , "A simple AC susceptometer Mounted on a Cryostat Cold finger"*, Journal of Magnets and Magnetic Materials*, vol .226, pp. 2063-2064, May 2001.

55. Osborn J.A, "Demagnetizing Factors of the General Ellipsoid", *Phys. Review,* vol. 67, p. 351, March1945.

56. Gomory.F*,* "Low frequency magnetic measurements on high-T_c superconducting materials", *Thermochim Acta,* vol. 174, p.299 *,* January 1991.

57. Mohammed Shahabuddin and Nasser SalehAlzayed, "Design of ac susceptometer using closed cycle helium cryostat", *Phys.Stat Sol*, no. 9, pp.3002-3006, July 2006.

58. D.X Chen *et al*, "AC Susceptibility of half-half jointed melt-textured YBCO rings" *Physica C*, vol. 460-462,Part2, pp. 770-771, September 2007

59. E.Seiler and L.Frolek "AC Loss of $YBa_2Cu_3O_7$ coated conductor in high Magnetic Fields", *at 8th European Conference on Applied superconductivity,* 2007,

60. D.X chen *et al*, "ac susceptibility and critical current densities in sintered $YBa_2Cu_3O_{7-\delta}$ superconductors*", Applied Physics Letters*, vol. 89, p. 72501,August 2006.

61. M.Ciszet *et al*., "Influence of hydrogenation on inter- and intragranular critical currents in $YBa_2Cu_3O_{7-\delta}$", *J.Appl. Phys*. vol 76, pp. 2357-2360, August 1994

62. Goldfarb R.B and Minervini J.V, "Calibration of AC Susceptometer for Cylindrical Specimens" *Rev. Sci. Instrumentation*, vol.55, pp. 761-764, May 1984

63. Jack W. Ekin , "Heat Transfer at Cryogenic Temperatures" *in Experimental Techniques for Low Temperature Measurements,* New York: Oxford Press, 2006, p.51.

64. Si, Thermal Properties [online] 2014, http://www.ioffe.ru/SVA/NSM/Semicond/Si/Figs/151.gif (Accessed June 2014).

65. K. J. Song *et al*., "The effect of solvent treatments and aging on the superconducting properties of MgB2 materials*", Physica C*, vol. 467, no. 1-2, pp. 106-111, Dec. 2007.

66. J.J. Reilly *et al*., "Superconductivity in HxYBa2Cu3O7", *Physical Review B*, vol.36, no.10, pp. 5694-5697, October 1987.

67. D.Di Gioacchino *et al*.,"Further enhancement of critical temperature up to 105 K of hydrogen loaded YBCO melted samples by μs pulsed electrolysis", *Physics Letters A,* vol. 225, pp. 326-330, February 1997.

68. J. Volkl and G. Adefeld, "Diffusion of Hydrogen in Metals"*,* in *Hydrogen in Metals I,* Berlin Heidelberg, Germany, Springer, 1978, ch.8, pp. 197-226.

69. H. Ehrenreich and F. Spaepen, "Solid solutions of hydrogen in complex materials", *Solid State Physics*, vol.69, pp. 203-305,2004

70. D.R. Sadoway, "Diffusion", class notes for 3.091, Dept. of Material Science and Engineering, Massachusset Institute of Technology, 2004.

Appendix A Lock-in Amplifier Software in DASYLab

A software lock-in amplifier was implemented in DASYLab software environment. The signals were fed to the computer via the IOTech Daqbook 2000 Ethernet-base data acquisition hardware. The schematic of the software used for T_c characterization is shown in Figure A1. The reference signal and the magnetic experimental signals were fed to channel 1 and 2 respectively. For intergranular critical current density J_{ci} characterisation, the schematic of the software is shown in Figure A2. The reference signal is fed to channel 1, the magnetic signal due to diamagnetic response of the superconducting specimen is fed to channel 2 and channel 3 was used to read the signal from amplifier X (which forms part of the differential amplifier used for balancing and amplification; shown in Appendix C) which represents the magnetic flux density at the centre of the primary coil.

The signals from channel 2 were filtered by a narrow band-pass filter, implemented by the combination of low and high-pass filters. The signals are then multiplied with the reference and the imaginary reference signals and then low-pass filtered to extract the DC components of the in-phase and the out-of-phase components of the magnetization signals. The outputs from the low-pass filter LPF1 are the signals V' (Equation 5.14) and V'' (Equation 5.18) respectively.

Data were sampled by the IO Tech DaqBook 2000 module at a sampling frequency of 25 KHz. A timing system was implemented together with the lock-in amplifier in DASYLab environment to write the data to the hard disk every two second.
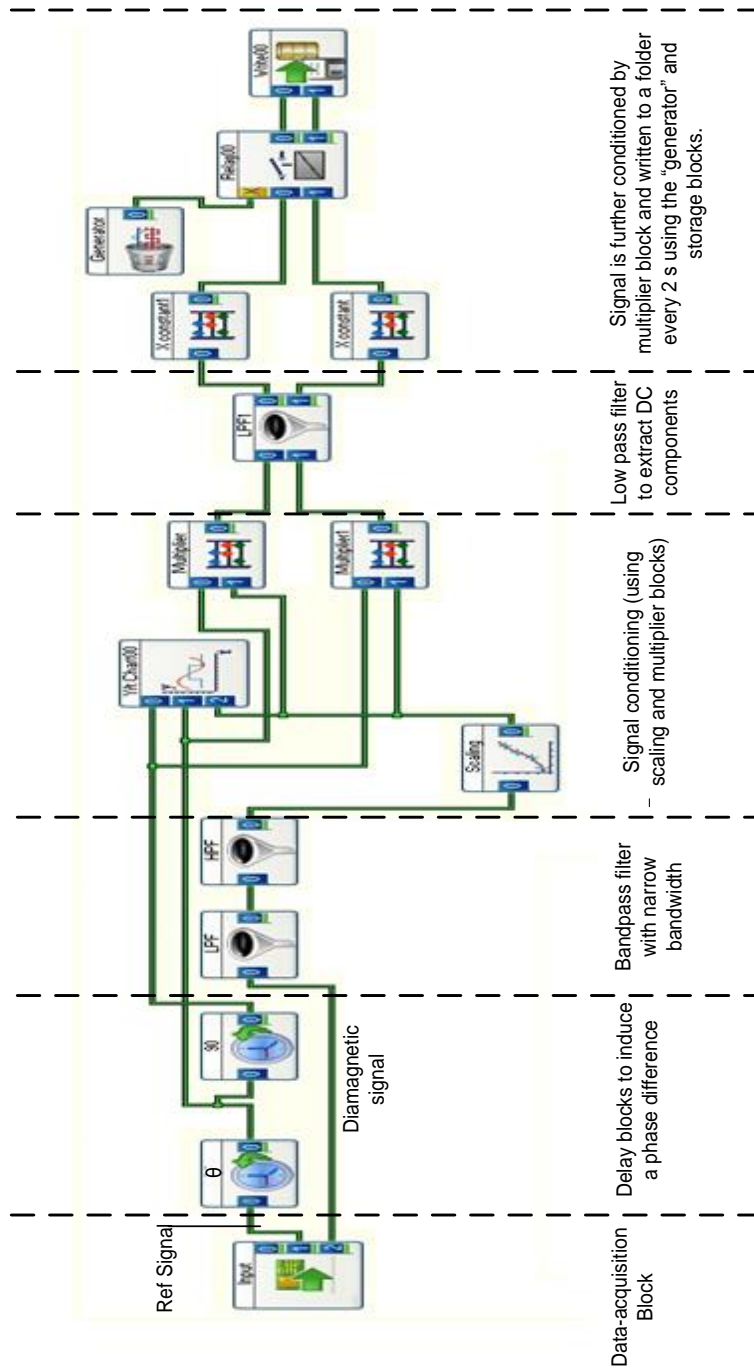
Figure A1 Lock-in amplifier software, implemented in DASYLab environment used for AC susceptibility measurements for T_c characterization.
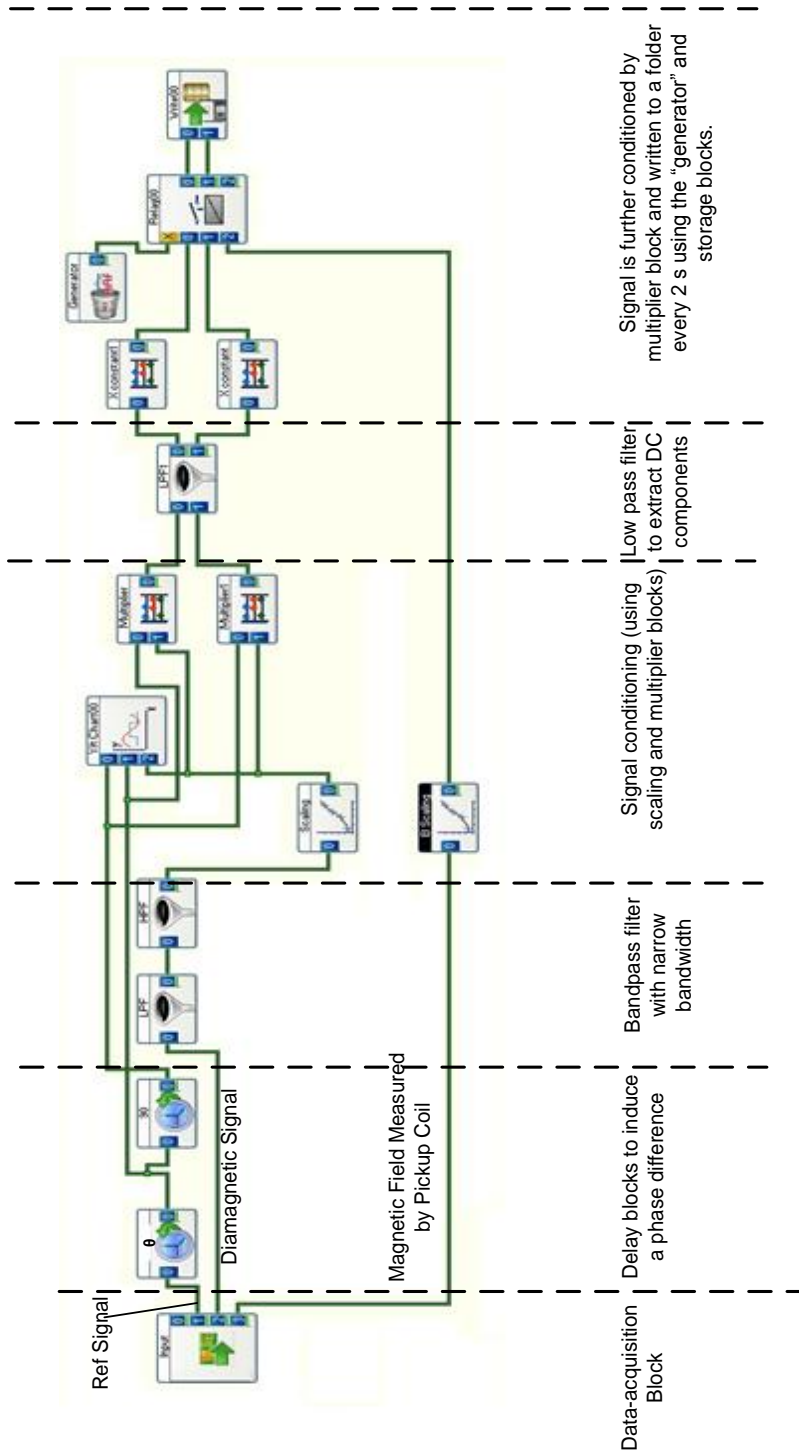
Figure A2 Lock-in amplifier software, implemented in DASYLab environment used for AC susceptibility measurements for intergranular critical current J_{ci} characterization.

Appendix B Software for Temperature Logging

The temperature logger software used to log temperature data was written by Brett Swann and Jonathan Archer [unpublished]. Brett Swan was one of the past students from the material science Lab and Jonathan Archer is a registered student doing his PHD. The logger software provides remote logging of temperature data by interfacing the Lakeshore Model 336 temperature controller over the Ethernet. The logging interval can be adjusted and the software also displays the history of the temperature and derivatives.
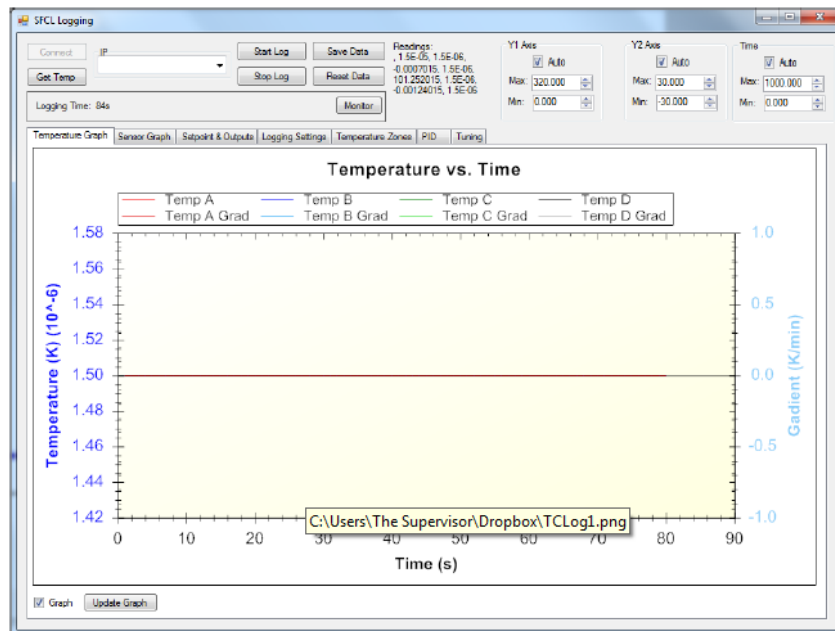

Figure B1 Main page of temperature logger software.

Appendix C Differential Amplifier

The differential amplifier was used for balancing and amplification purposes. The amplifier circuit is made up of a combination of INA128 instrumentation amplifiers. Since the two secondary coils are not perfectly identical, a mismatch exists in their output voltages. So, the amplifier circuit was used to remove the voltage mismatch when the secondary coils were empty. The signal produced due to the diamagnetic response of a superconducting specimen (from coil_2) was amplified. R_{G1} and R_{G2} are variable resistors (0- 50 KΩ) used to control the gain of the amplifiers X and Y respectively.

The output voltage V_{output} of the INA 128 amplifier is calculated using the following equation:

$$G = 1 + \frac{50\ K\Omega}{R_G} \qquad (C.1)$$

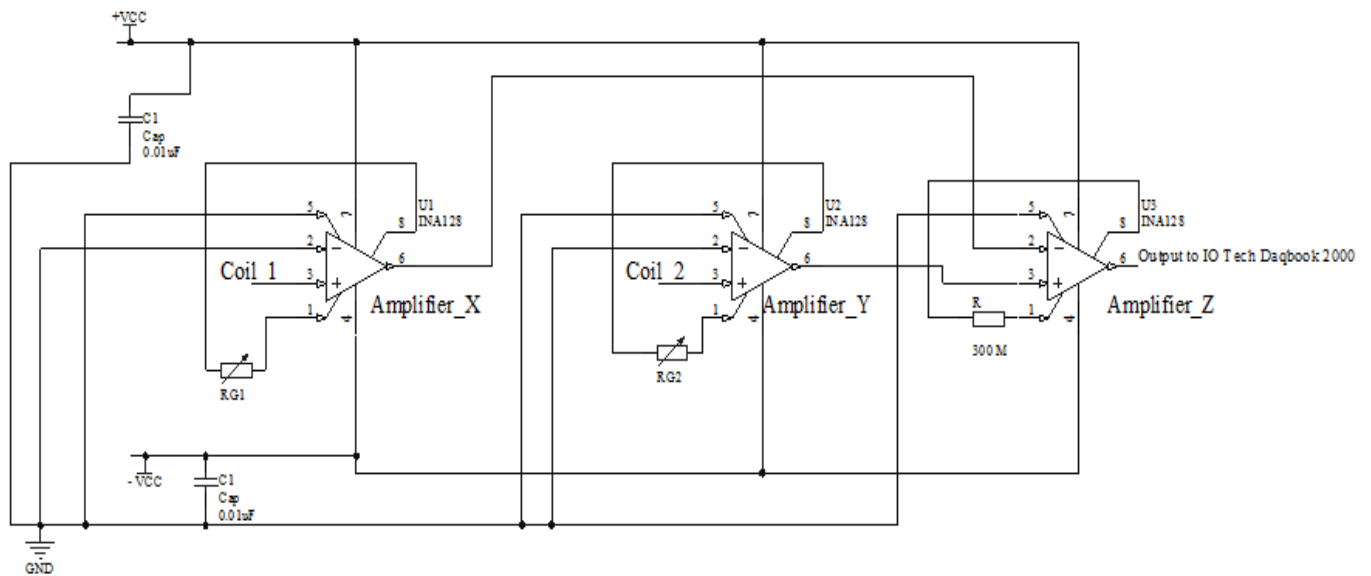$$V_{output} = G(V_{in}^+ - V_{in}^-) \qquad (C.2)$$

Figure C1 Amplifier Circuit used for amplification and balancing.

The amplifier was initially used to remove the offset voltage (mismatch voltage) by adjusting the values of R_{G1} and R_{G2} (0 to 1000 Ω). Once the offset voltage was removed, the amplifier gain

134

(of Amplifier_Y) was determined using a test sinusoidal signal produced by a function generator (10.0 mV pk-pk). The circuit and coils were very stable as once the offset was removed and the overall amplifier gain (gain ≈ 51 for T_c experiments and for susceptibility v/s magnetic field experiments) was set at the beginning before the first experiment. So, there was no need of varying the values of R_{G1} and R_{G2} for balancing and amplification purposes before each magnetization experiment.

Appendix D Calibration of Sensing Coil

The empty secondary coil of the AC susceptometer was used to sense the magnetic flux density inside the primary coil, which is fairly uniform. The voltage across the sensing coil was fed to amplifier X which forms part of the differential amplifier (Appendix C). The output of amplifier X was fed to the IO Tech Daqbook 2000 data acquisition module. This voltage was amplified in DASYLab and the resulting voltage V_X was recorded with respect to current. The magnetisation experiment for intergranular J_{ci} determination was done at liquid nitrogen temperature, 77.0 K. So, the calibration experiment was also done by submerging the AC susceptibility apparatus into liquid nitrogen (at 77.0 K), to conform to the magnetisation experimental conditions.

The current I flowing through the primary coil, from which B was calculated, was varied by varying the voltage across the primary coil and the corresponding values of V_X were recorded and tabulated. A graph of V_X against I was plotted and the gradient K was determined.

$$K = \frac{\Delta V_X}{\Delta I} \qquad\qquad (D.1)$$

$$B = \left(\frac{\mu_o N}{lK}\right) V_X \qquad\qquad (D.2)$$

So, the magnetic flux density inside the primary coil was estimated using the value of K ($K = 2.32\ V/A$) and the values of V_X using Equation D.2 (calculation and logging were done in DASYLab software environment).
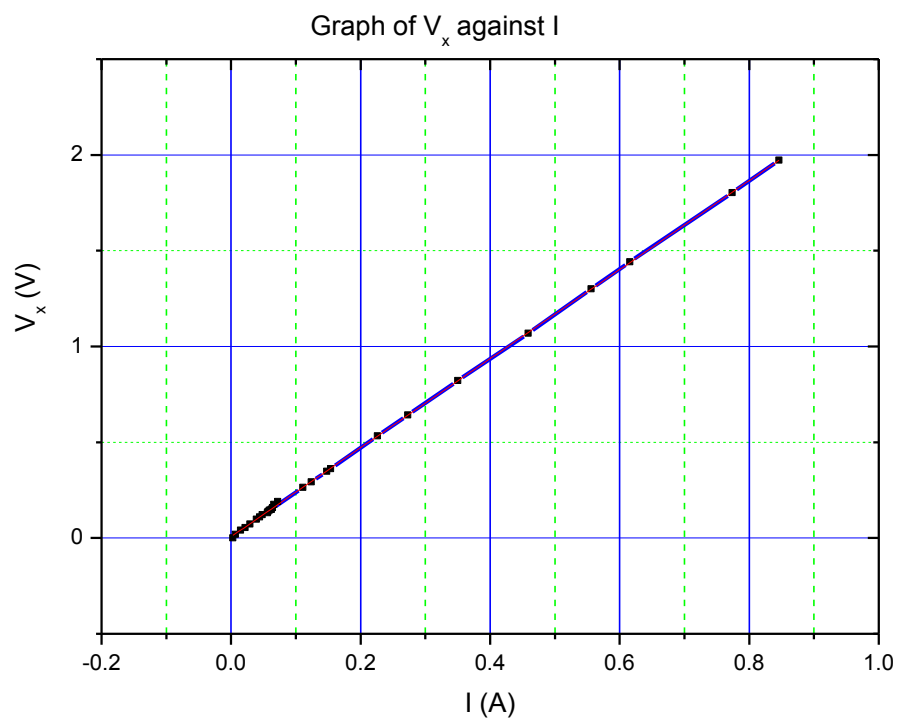
Figure D1 Calibration curve for sensing coil at 77 K, graph of V_X vs. I

Appendix E Resistivity Graph of Undoped Bulk YBCO Sample

The resistivity (arbitrary unit) of an undoped bulk YBCO sample was plotted against the temperature in Kelvin. T_c was found to have a value of approximately 92.0 K as expected.
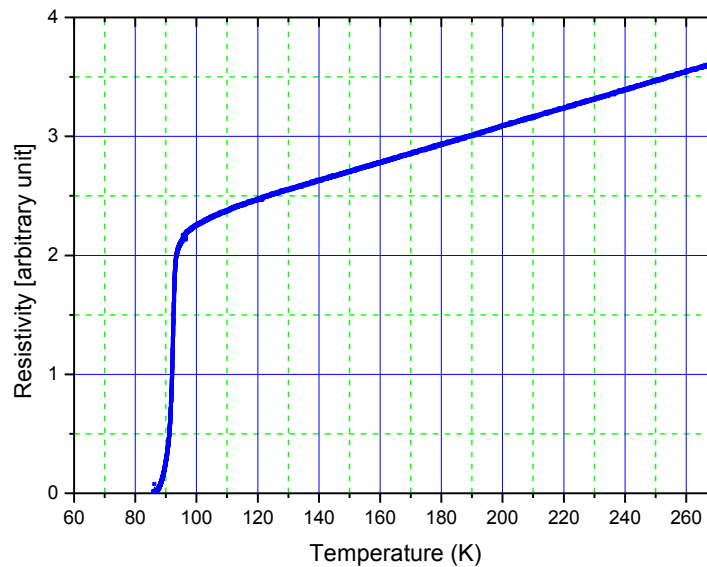
Figure E1 Resistivity vs. temperature of an undoped YBCO sample.